

Copyright Undertaking

This thesis is protected by copyright, with all rights reserved.

By reading and using the thesis, the reader understands and agrees to the following terms:

- 1. The reader will abide by the rules and legal ordinances governing copyright regarding the use of the thesis.
- 2. The reader will use the thesis for the purpose of research or private study only and not for distribution or further reproduction or any other purpose.
- 3. The reader agrees to indemnify and hold the University harmless from and against any loss, damage, cost, liability or expenses arising from copyright infringement or unauthorized usage.

IMPORTANT

If you have reasons to believe that any materials in this thesis are deemed not suitable to be distributed in this form, or a copyright owner having difficulty with the material being included in our database, please contact lbsys@polyu.edu.hk providing details. The Library will look into your claim and consider taking remedial action upon receipt of the written requests.

BUILDING STABLE ELECTRODE/ELECTROLYTE INTERFACES FOR ADVANCED POTASSIUM-ION BATTERIES

YU ZHENLU

PhD

The Hong Kong Polytechnic University

The Hong Kong Polytechnic University Department of Applied Physics

Building Stable Electrode/Electrolyte Interfaces for Advanced

Potassium-Ion Batteries

YU ZHENLU

A thesis submitted in partial fulfilment of the requirements for the degree of Doctor of Philosophy

CERTIFICATE OF ORIGINALITY

YU Zhenlu (Name of student)

I hereby declare that this thesis is my own work and that, to the best of my knowledge
and belief, it reproduces no material previously published or written, nor material that
has been accepted for the award of any other degree or diploma, except where due
acknowledgment has been made in the text.
(Signed)

Abstract

Potassium ion batteries (PIBs) are considered promising complements to prevailing Liion batteries for large-scale energy storage. Stable cycling of PIBs relies on not only the development of advanced electrode materials but also the building of robust electrode/electrolyte interfaces on both anode and cathode sides. This thesis first explores the K ion storage mechanism in carbon anodes and then investigates the effect of the anode/electrolyte interface on the charge/discharge kinetics. The carbon-based interfacial chemistry regulation strategy is further extended to high-capacity potassium metal anodes. Along with the anodes, this thesis is also committed to constructing cathode/electrolyte interfaces at a high voltage to realize a competitive energy density.

Hard carbon is among the most attractive anodes for PIBs, but the inexplicit charge storage mechanism at the low voltage region impedes the rational structural design. Systematic studies demonstrate the presence of quasi-potassium nanoclusters after deep discharging, evidencing that the K ion pore-filling, in addition to intercalation, contributes to the low-voltage capacity. To improve the rate performance of hard carbons, cyclic ether tetrahydrofuran (THF) as a weak solvent is applied to regulate the interfacial chemistry and boost the de-solvation process. An inorganic-rich solid electrolyte interphase (SEI) resulting from enhanced anion decomposition benefits the charge transfer for superior rate capability and cyclic performance even at 0 °C.

Besides severing as anodes, carbon-based materials have been widely utilized as the host for potassium metal anodes. Carbon nanofibers are adopted as a model system to explore the surface functionality of carbon in determining interfacial behavior. Because of the lower Fermi level than commercial Al, the CNFs modified Al prevents excessive electrolyte consumption and promotes the formation of thin inorganic-rich SEI. The performance is further improved by incorporating nickel species to provide abundant active sites for K-embryo nucleation and induce planar growth of K metal. Consequently, the decorated Al current collector enables a 4.4 V anode-free full cell with 89% capacity retained after 50 cycles.

To achieve a high-voltage potassium metal battery, we extend the terminal alkyl chain of ether solvent to alleviate the electrolyte decomposition at high voltages. The high viscosity accompanied by the long alkyl groups could be effectively mitigated by introducing an S-containing additive, which further enhances the oxidative stability to 4.6 V. Additionally, the additive aids in forming S-rich organic species at the interphases, which prevents the cathode's metal dissolution and facilitate uniform K deposition by enhancing the kinetics. Thanks to the stable interphases and minimized side reactions, the dilute non-fluorinated ether-based electrolyte allows the full cell to cycle stably for more than 200 cycles, achieving a high Coulombic efficiency of over 99.4% with a negative/positive capacity ratio of 4.

List of Publications

- *Equal contribution; *Corresponding author
- 1. **Zhenlu Yu**[#], Changsheng Chen[#], Qun Liu, Jie Liu, Mingxue Tang, Ye Zhu, Biao Zhang*, Discovering the Pore-Filling of Potassium Ions in Hard Carbon Anodes: Revisit the Low-Voltage Region, Energy Storage Materials, 2023, 60, 102805.
- 2. **Zhenlu Yu**, Qun Liu, Changsheng Chen, Ye Zhu, Biao Zhang*, Regulating the Interfacial Chemistry Enables Fast-Kinetics Hard Carbon Anodes for Potassium Ion Batteries, Journal of Power Sources, 2023, 557, 232592.
- 3. **Zhenlu Yu**[#], Ke Fan[#], Qun Liu, Danni Wang, Changsheng Chen, Ye Zhu, Haitao Huang, Biao Zhang*, Designing Electrolytes with Steric Hindrance and Film-Forming Booster for High-Voltage Potassium Metal Batteries, Advanced Functional Materials, 2024, 34, 2315446.
- 4. **Zhenlu Yu**, Qun Liu, Danni Wang, Jie Shi, Biao Zhang*, Unraveling Electrode Surface Chemistry in Determining Interphase Stability and Deposition Homogeneity for Anode-free Potassium Metal Batteries. Angewandte Chemie, 2025. Accepted.
- 5. Qun Liu, **Zhenlu Yu**, Qiuna Zhuang, Jang-Kyo Kim, Feiyu Kang, Biao Zhang*, Anti-Fatigue Hydrogel Electrolyte for All-Flexible Zn-Ion Batteries, Advanced Materials, 2023, 35, 2300498.
- 6. Qun Liu, Zhenlu Yu, Rui Zhou, and Biao Zhang*, A Semi-Liquid Electrode toward

Stable Zn Powder Anode, Advanced Functional Materials, 2023, 33, 2210290.

- 7. Qun Liu, **Zhenlu Yu**, and Biao Zhang*, Tackling the Challenges of Aqueous Zn-Ion Batteries via Polymer Derived Strategies, Small Methods, 2023, 8, 2300255.
- 8. Qun Liu, **Zhenlu Yu**, Ke Fan, Haitao Huang, Biao Zhang*, Asymmetric Hydrogel Electrolyte Featuring Customized Anode and Cathode Interfacial Chemistry for Advanced Zn-I₂ Batteries, ACS Nano, 2024, 18, 22484-22494.
- 9. Mingcong Tang, Qun Liu, **Zhenlu Yu**, Xiaohong Zou, Xiaoyu Huo, Biao Zhang*, Liang An*, Bi-Funcional Electrolyte Additive Leading to a Highly Reversible and Stable Zinc Anode, Small, 2024, 20, 2403457.
- 10. Mingcong Tang, Qun Liu, Xiaohong Zou, **Zhenlu Yu**, Kouer Zhang, Biao Zhang*, Liang An*, Engineering In Situ Heterometallic Layer for Robust Zn Electrochemistry in Extreme Zn(BF₄)₂ Electrolyte Environment, Energy Storage Materials, 2024, 74, 103896.

Acknowledgments

Upon finishing this thesis, I would like to appreciate the great support and help from everyone throughout my PhD study.

First I am incredibly grateful to my supervisor Prof. Biao Zhang for giving me excellent guidance and helpful expertise in my research from experiment design to shaping the paper. His great ability in critical thinking taught me a global but specific perspective on research. I also would like to thank my co-supervisor Prof. Haitao Huang for his kind help and support during my study. Besides, I am truly thankful to Prof. Ye Zhu, Dr. Changsheng Chen, and Dr. Ke Fan for their contribution to conducting cryotransmission electron microscopy and theoretical simulation. My heartful gratitude is also conveyed to colleagues and friends, Dr. Qun Liu, Dr. Yao Gao, Dr. Xiaoqiong Du, Dr. Zhen Hou, Dr. Rui Zhou, Ms. Danni Wang, Ms. Jie Shi, Mr. Yao Liu, Mr. Mengzi Geng, Mr. Fanbin Zeng, and Mr. Mingcong Tang, for their support and insightful advice. Additionally, I really thank my parents for their unconditional love, understanding, and support, which are the bedrock of my academic pursuit.

Lastly, I extend my deepest appreciation to the examiners. Thank you for your valuable time and patience in the review. Your comments boosted the quality of this thesis.

Table of Contents

Abstract	I
List of Publications	III
Acknowledgments	V
Table of Contents	VI
List of Figures	X
List of Tables	X
Chapter 1. Introduction	1
1.1 Development of Potassium Ion Batteries	1
1.2 Cathode	2
1.2.1 Oxides	3
1.2.2 Prussian Blue Analogs	4
1.2.3 Polyanion Compounds	7
1.3 Anode	8
1.3.1 Carbonaceous Materials	8
1.3.2 Conversion and Alloying Types	12
1.3.3 Potassium Metal	14
1.4 Electrolyte	16
1.4.1 Solvents and Salts	17
1.4.2 Molecules Design of Solvents	23
1.4.3 (Localized) High Concentration of Salts	24
1.5 Objective and Outline	25
Chapter 2. Experimental Section	27

2.1 Materials Synthesis	.27
2.1.1 Pistachio-derived Hard Carbons	.27
2.1.2 Carbon Nanofibers (CNFs)	.27
2.1.3 Lignin-based Hard Carbon Powder	.28
2.1.4 CNFs Grown with Nickel Species (CNFNis)	.28
2.1.5 CNF@Al and CNFNi@Al Current Collectors	.29
2.1.6 Fe-based Prussian Blue FeHCF	.29
2.1.7 Mn-based Prussian Blue Analog MnHCF	.30
2.2 Electrodes and Electrolytes Preparation	.30
2.2.1 Electrodes	.30
2.2.2 Electrolytes	.31
2.3 Materials and Electrolytes Characterization	.32
2.3.1 Structure and Composition Analysis	.32
2.3.2 Pores Structural Information of Hard Carbon	.33
2.3.3 Morphology Scanning	.33
2.3.4 Thermostability Measurements	.34
2.3.5 Mechanical Properties of Solid Electrolyte Interphase	.34
2.4 Electrochemical Measurements	.36
2.4.1 Cycling with Rate Performance	.36
2.4.2 Kinetics Behavior Probing	.37
2.5 Computational Calculation	.38
Chapter 3. Discovering the K-ion Pore-filling Behavior and Regulating	the
Interfacial Chemistry for Fast-kinetics Hard Carbon Anode	.39
3.1 Introduction	.39

3.2 Probing Potassium Storage Behavior41
3.2.1 Synthesis and Physical Properties of Hard Carbon
3.2.2 Electrochemical Performance and Kinetics
3.2.3 K-ion Storage Behaviors
3.2.4 Discussion
3.3 Interfacial Chemistry Regulation
3.3.1 Solvation Structures of Different Electrolytes
3.3.2 Different Kinetics Behaviors
3.3.3 Charge Storage Mechanisms and Interfacial Chemistry71
3.4 Summary
Chapter 4. Tailoring Solid Electrolyte Interphase by Carbonaceous Materials for
Advanced Potassium Metal Anodes79
4.1 Introduction
4.1 Introduction794.2 Results and Discussion81
4.2 Results and Discussion
4.2 Results and Discussion
4.2 Results and Discussion 81 4.2.1 Properties of CNFNi@Al 81 4.2.2 Potassium Nucleation Behavior 87
4.2 Results and Discussion814.2.1 Properties of CNFNi@Al814.2.2 Potassium Nucleation Behavior874.2.3 SEI on Deposited K93
4.2 Results and Discussion814.2.1 Properties of CNFNi@Al814.2.2 Potassium Nucleation Behavior874.2.3 SEI on Deposited K934.2.4 Electrochemical Performance1014.3 Summary107
4.2 Results and Discussion814.2.1 Properties of CNFNi@Al814.2.2 Potassium Nucleation Behavior874.2.3 SEI on Deposited K934.2.4 Electrochemical Performance101
4.2 Results and Discussion
4.2 Results and Discussion

Ref	ferences	137
	6.2 Future Plan	135
	6.1 Conclusion	133
Ch	apter 6. Conclusion and Future Plan	133
	5.3 Summary	131
	5.2.4 Performance of MnHCF K Cells Under a Harsh Condition	130
	5.2.3 Enhanced Stability of Modified Electrolyte against K Anode	124
	5.2.2 Compatibility of Modified Electrolyte with MnHCF Cathode	118

List of Figures

Figure 1.1. Voltage profiles for alkali-metal layered oxides. The shadow parts indicate the similar profiles of different oxides. Reproduced with permission ¹⁰ . Copyright 2020. American Chemical Society
Figure 1.2. (a) Charging-discharging profile for K _{1.89} Mn[Fe(CN) ₆] _{0.92} ·0.75H ₂ O. Reproduced with perssion ¹² . Copyright 2017. American Chemical Society. (b) Initial discharging profile of K ₂ Ni _{0.05} Fe _{0.95} Fe(CN) ₆ (NiFePB-5) and K ₂ FeFe(CN) ₆ (NiFePB-0). Reproduced with permission ¹⁵ . Copyright 2019. American Chemical Society6
Figure 1.3. Comparison of volumetric energy and gravimetric energy of layered oxides (A=Li, Na, K; TM=Co, Mn, Ni, etc.). Reproduced with permission ¹⁰ . Copyright 2021. American Chemical Society
Figure 1.4. Typical carbon-based materials with characteristic structures. Reproduced with permission ¹⁸ . Copyright 2018. Wiley-VCH
Figure 1.5. The potassium storage mechanism of alloying-type materials, taking the Bi as an example. Reproduced with permission ²⁵ . Copyright 2018. Wiley-VCH
Figure 1.6. Typical phosphate solvents derived from TMP
Figure 3.1. (a) Synthesis procedure of hard carbon (b) XRD Patterns of HC samples with or without HCl treatment. (c) Overall XPS result of HC-130042
Figure 3.2. (a) Raman curves, (b) XRD patterns, (c) initial charging-discharging profiles, (d) cycling performance, and (e) rate performance of HC-1100, HC-1300, and HC-1400 with corresponding (f) 26th voltage profile of HC-1400 in e
Figure 3.3. (a) HRTEM with marked defects (the left square), graphitic domain (rectangle in the middle). (b) SAXS patterns presenting pores and graphitic layers. (c) Fitted SAXS profiles of HC-1300. Volume distribution of (d) micropores and (e) mesopores calculated through fitted SXAS results
Figure 3.4. BET isotherms with porosity distribution derived from (a) N ₂ and (b) CO ₂ adsorption/desorption
Figure 3.5. Initial two charging-discharging profiles with insets of dQ/dV profiles for

(a) HC-1300/K cell and (b) HC-1300/Na cell. (c) Diffusion coefficient calculated from
GITT results of HC-1300/K cell and HC-1300/Na cell. (d) EIS plots of HC-1300
obtained from three-electrode cells at different discharging states. The inset illustrate
the three-electrode Swagelok cell. Cycling performances of (e) HC-1300/K cell and (f
HC-1300/Na cell
Figure 3.6. (a) Ex situ Raman curves of HC-1300/K collected at different charge
discharge states with (b) the corresponding charging-discharging profile
Figure 3.7. (a) Initial discharging profiles of HC-1300 in CC-CVDi mode followed by
2 h plating at 25 mA g ⁻¹ . (b) Ex situ XRD patterns for the sample after CVDi and the
plated K sample
Figure 3.8. (a) Ex situ K 2p-C 1s spectra of samples at different charge-discharge state
after Ar-beam etching (40 nm depth with rate of 0.25 nm s ⁻¹) with plated K as the
reference. (b) Ex situ K 2p peaks of samples at different states. Here DC and C represen
the discharge and charge, respectively. All the spectra are normalized through C-C peal
at 284.8 eV
Figure 3.9. (a) Annular dark-field STEM image and the simultaneous EDS elementa
maps for C, K, and O of CVDi-5 mV sample. Ex situ HR-TEM images of discharged
HC-1300 at 5 mV (b) DC 5 mV sample, with the corresponding FFT pattern (inset)
and (c-e) CVDi 5 mV (K deeper insertion) sample, with the corresponding SAEI
pattern presented in the inset. (f-g) Intensity plots derived from SAED image. All the
TEM observation was taken at a cryogenic temperature of ~98 K to preserve the pristing
state of the samples54
Figure 3.10. EELS of (a) the DC 5 mV sample and (b) the CVDi 5 mV sample50
Figure 3.10. EELS of (a) the DC 5 mV sample and (b) the CVDi 5 mV sample50 Figure 3.11. (a) EPR spectra of samples at different stages of cycling. (b) Schematic
Figure 3.11. (a) EPR spectra of samples at different stages of cycling. (b) Schematic
Figure 3.11. (a) EPR spectra of samples at different stages of cycling. (b) Schematic illustration of proposed K ion storage behavior along with discharging
Figure 3.11. (a) EPR spectra of samples at different stages of cycling. (b) Schematic illustration of proposed K ion storage behavior along with discharging
Figure 3.11. (a) EPR spectra of samples at different stages of cycling. (b) Schematic illustration of proposed K ion storage behavior along with discharging

Figure 3.14. (a) The initial first two charging-discharging profiles of HC-KOH compared with HC-1300 2nd profile. (b) The rate performance of HC-1300 and HC-KOH (under the galvanostatic potentiostat discharging-galvanostatic charging mode)
Figure 3.15. (a) Raman spectra of electrolytes, pure solvents, and KFSI salt. (b) Enlarged FSI ⁻ peaks of 1M KFSI in THF and 1M KFSI in DME. (c) Schematic illustration of the solvating structure of 1M KFSI in DME and 1M KFSI in THF64
Figure 3.16. (a) Fabrication scheme of CNFs for PIBs. (b) SEM and (c) HRTEM images of CNFs. (d) XRD pattern of CNF
Figure 3.17. (a) XPS results and (b) Raman pattern of as-prepared CNFs66
Figure 3.18. Charge-discharge profiles of CNFs in different electrolytes with inset of dQ/dV curve (a) 1M KFSI in DME electrolyte. (b) 1M KFSI in THF electrolyte67
Figure 3.19. (a) Initial charge/discharge profiles of CNFs. (b) Rate behaviors of CNFs at 25 °C in 1M KFSI in EC/DMC, 1M KFSI in THF, and 1M KFSI in EC/EMC electrolytes. (c) Rate performances of Lignin powder in different electrolytes. (d) Cyclic performance of CNFs in 1M KFSI in THF at 100 mA g ⁻¹ at 25 °C
Figure 3.20. (a) Cyclic performances of CNFs at 0 °C. K ion apparent diffusion coefficient calculated from GITT results of CNF upon (b) discharging and (c) charging (d) EIS plots of 3rd-cycled CNF electrode in different electrolytes at 100 mA g ⁻¹ 71
Figure 3.21. In-situ Raman plots of CNF electrode using the electrolyte of (a) 1M KFSI in THF and (b) 1M KFSI in EC/DMC.
Figure 3.22. TEM images of third-cycled CNFs in (a) 1M KFSI/THF and (b) 1M KFSI ECDMC with corresponding FFT patterns in the marked area at 50 mA g ⁻¹ 73
Figure 3.23. The surficial composition analyzed by XPS. (a) K 2p-C 1s, (b) O 1s, and (c) F 1s spectra of CNFs after 3 cycles at 50 mA g ⁻¹ using electrolyte of 1M KFSI in THF or 1M KFSI in EC/DMC; (d) The atomic fractions of pristine CNFs cycled in 1M KFSI in THF or 1M KFSI in EC/DMC.
Figure 4.1. (a) Illustration of spray-painting and (b) photograph of CNFNi@Al82

Figure 4.2. (a) Morphology and (b) lattice fringes of components of CNFNi captured
via high-resolution TEM. SAED patterns for (c) CNFNi and (d) CNF82
Figure 4.3. (a) Raman patterns of CNF and CNFNi samples. (b) Ni 2p spectrum and
(c) TGA curve of CNFNi powder under synthetic air atmosphere (80% $N_2+20\%$ O_2)
(d) XRD profiles of CNF and CNFNi83
Figure 4.4. Wetting angles of (a) the DEE electrolyte and (b) molten K on Al o
CNFNi@Al84
Figure 4.5. UPS profiles of Al, CNF@Al, and CNFNi@Al at different states 83
Figure 4.6. Calculated Fermi-level positions based on work function
Figure 4.7. Overall element composition of SEIs generated after 3 formation cycles at 5 mV-1 V.
Figure 4.8. (a) O 1s of SEIs generated after 3 formation cycles at 5 mV-1 V. (h) Specie
composition analyzed based on N 1s and S 2p spectra. (b) Species composition in O 1
spectra. (c) N 1s, (d) F 1s, (e) S 2p spectra of SEIs. (f) Species composition based on N
1s and S 2p spectra, respectively8
Figure 4.9. (a) The potential-capacity plots of K current collector cells at 0.5 mA cm
² -1 mAh cm ⁻² . (b) Comparison of μ_{tip} and $\mu_{mass-transfer}$ of asymmetric cells based on
different current collectors. (c) Tafel plots of symmetric cells based on different current
collectors.
Figure 4.10. (I/I _m) ² -(t/t _m) profiles of different asymmetric cells with different curren
collectors with the overpotential of -50, -100, and -150 mV.
Figure 4.11. Illustration of two nucleation models.
Figure 4.12. (a) Photographs of the GF/D separator in disassembled coin cells. (b-c
SEM images with EDS mappings and (d) XRD patterns of 10th-plated K on different
current collectors
Figure 4.13. (a-c) Planer images of 10th-plated K on Al, CNF@Al, and CNFNi@Al
(d) Three-dimensional AFM topography of 10th-plated K on A and CNFNi@Al. (e
Height variation curves on marked lines in d

Figure 4.14. (a) C 1s-K 2p and (b) O 1s spectra of 10th-plated K on Al and CNFNi@Al
current collectors, respectively94
Figure 4.15. (a) S 2p, (b) F 1s, and (c) N 1s spectra of 10th-plated K on Al and CNFNi@Al current collectors, respectively
Figure 4.16. (a) TOF-SIMS 3D rendering images of S, F, K, HCO ₂ K, C-O-K, and KF signals. (b) Depth profiles for S, F, CH ₃ OSO ₂ , KS, and KNO ₃
Figure 4.17. (a) TOF-SIMS depth profiles for K signal. (b) The approximate SEI thickness (t) obtained from AFM-based nanoindentation measurements on 10th-plated K on different substrates.
Figure 4.18. Proposed typical decomposition scheme of DEE solvent with the interaction of K ion
Figure 4.19. (a) TOF-SIMS 3D redering images of KCO ₃ , KS, KSO ₃ , CH ₃ OSO ₂ , KNO ₃ and K ₂ N signals. (b) EIS results with (c) simulated resistance values of asymmetric cells after 10th plating based on different current collectors
Figure 4.20. Nyquist plots of (a) CNFNi@Al and (b) Al-based asymmetric cells at different temperatures with the inset of equivalent circuit. (c) Derived activation energy values for charge transfer.
Figure 4.21. HRTEM images of SEI formed on (a-e) CNFNi@Al and (f-h) Al99
Figure 4.22. Distribution curves of testing values of (a) Young's modulus E , (b) elastic strain limit ε_Y , and (c) U values of SEI on different substrates
Figure 4.23. (a) Aurbach cycling profiles of asymmetric cells based on different current collectors. The long-term cycling performance of asymmetric cells at (b) 0.5 mA cm ⁻² -1 mAh cm ⁻² and (c) 2 mA cm ⁻² -1 mAh cm ⁻² , respectively
Figure 4.24. (a) Rate performance of the symmetric cells with the pre-plating capacity of 2 mAh on different current collectors. Cycling performance of asymmetric cells under (b) 25% DoD and (c) 50% DoD at 0.5 mA cm ⁻² -0.5 mAh cm ⁻²
Figure 4.25. (a) The cycling performance of CNFNi@Al-K FeHCF with an N/P ratio of 5 with (b) the cycling profile at the 50th cycle. The cycling performance of

CNFNi@Al-K MnHCF with (c) an N/P ratio of 1 and (d) an N/P ratio of 0 (Anodefree)
Figure 5.1. Rational design of ethers with high anodic stability and kinetics and the synergic effects of customized electrolyte in K metal batteries
Figure 5.2. (a) LSV curves of different electrolytes with the scanning rate of 1 mV s ⁻¹ (b) SEM images of the Al-C electrode after being held at 3.7 V for 10 h in 1M KFSI/G2 electrolyte. (c) Curves obtained from the Chronoamperometry measurement to hold K Al-C cell in 1M KFSI/DiDBE electrolyte at 4.3 V for 10 h with (d) corresponding SEM images of the tested Al-C electrode.
Figure 5.3. (a) The viscosity of DiDBE electrolyte and DiDBE-D electrolyte. (b) EIS plots of two stainless steels with GF/D filled with DiDBE and DiDBE-D electrolytes for ionic conductivity measurement with corresponding data
Figure 5.4. (a) ³⁹ K NMR spectra of different electrolytes. Raman spectra of C-O-C vibration of (b) G2 electrolyte and (c) DiDBE electrolyte with or without salt 114
Figure 5.5. (a) Raman spectra of S-N-S vibration of different electrolytes with the relative contents of SSIP, CIP, and AGG. (b) Raman spectra of S=O vibration of different species. (c) Illustrations of the most probable solvation structure of different electrolytes extracted from MD simulations
Figure 5.6. (a) Snapshots of the MD simulation cell and corresponding radial distribution function (RDF) plots for (a, b) 1M KFSI/G2, (c, d) 1M KFSI/DiDBE, (e, f) 1M KFSI/G4, (g, h) 1M KFSI/DiDBE-D
Figure 5.7. (a) XRD pattern; (b) TEM image and (c) SAED pattern of KMF119
Figure 5.8. Voltage profiles of KMF in G2 and G4 electrolytes
Figure 5.9. (a) Initial voltage curves of MnHCF in different electrolytes under 25 mA g ⁻¹ . (b) Comparison of ICE and salt concentration in state-of-art electrolytes for MnHCF (c) Chronoamperometry measurements to hold K Al-C cells at 4.3 V for 10 h and (d) corresponding SEM images of tested Al-C electrodes. (e) Rate performances
Figure 5.10. (a) Cycling performances of MnHCF in the DiDBE-D electrolyte with corresponding profiles in specific cycles. (b) Cycling performance of the MnHCF

electrode in EC/DEC electrolyte. (c) The mean voltage evolution upon cycling in different electrolytes
Figure 5.11. (a) Comparison of the remaining weight of different electrolytes at 150 °C based on TGA measurement. (b) DSC curves of cycled MnHCF
Figure 5.12. HRTEM images of MnHCF cycled in (a) DiDBE-D and (b) EC/DEC electrolyte with corresponding FFT in the selected square area. XPS spectra of (c) C 1s. (d) O 1s, (e) S 2p, and (f) F 1s.
Figure 5.13. (a) Long-term CE tests of K Al-C cells. Cycling performances of K K cells at 0.5 mA cm ⁻² and 0.5 mAh cm ⁻² in (b) DiDBE-D and EC/DEC, (c) DiDBE, and (d) EC/DEC-D electrolytes.
Figure 5.14. (a-c) Three-dimensional 10th-plated K topographic images in different electrolytes from AFM. (d-f) Corresponding sectional height curves of plated K on Al-C electrode.
Figure 5.15. Typical force-displacement curves at different regions for (a) the elastic region obtained with a small force of less than 30 nN and curves for (b) the plastic region obtained with a larger load, about 900 nN. Box charts with the distribution curve for (c) Young's modulus E , (d) elastic strain limit ε_Y , and (e) U values of elastic deformation of more than 70 testing positions
Figure 5.16. C 1s XPS spectra of plated K anode cycled in (a) DiDBE-D and (b) EC/DEC electrolytes. (c) C atomic percentage of different samples
Figure 5.18. (a-b) O 1s spectra and (c-d) S 2p spectra of 10 th -plated K on Al-C current collectors in DiDBE-D and EC/DEC electrolytes
Figure 5.19. Proposed reduction mechanism of DTD. Reproduced with permission ²⁰¹ . Copyright 2021. Wiley-VCH
Figure 5.20. (a) The cycling performance of K MnHCF cell with an N/P ratio of 4 in different electrolytes with (b) corresponding voltage profiles at the first cycle and 165th cycle

List of Tables

Table 1.1. Comparison between LIB and potential substitutes. 1
Table 1.2. Comparison of three typical cathode materials including K _{0.4} CrO ₂ , K ₂ MnFe(CN) ₆ , and KVPO ₄ F for PIBs.
Table 1.3. Comparison of three typical anode materials for PIBs. 16
Table 1.4. Comparison between different potassium salts for electrolytes. 22
Table 3.1. Pore size information of HC-1300. 45
Table 3.2. Comparison of the electrochemical performance of biomass-derived HC precursors. 48
Table 3.3. Physical and chemical properties of different solvents. 62
Table 3.4. Comparison of the electrochemical performance of PIB hard carbon anodes.
Table 4.1. Calculated nucleation density at different overpotentials91
Table 4.2. Summary of the fitted interface resistance values from Nyquist plots98
Table 4.3. Comparison of electrochemical performance of asymmetric cells between state-of-the-art modified anode and this work. 102
Table 4.4. Calculated standard deviation of CE at 0.5 mA cm ⁻² -1 mAh cm ⁻² 103
Table 4.5. Calculated standard deviation of CE at 2 mA cm ⁻² -1 mAh cm ⁻² 104
Table 4.6. Comparison of electrochemical performance of anode-less or anode-free full cells between state-of-the-art modified anode and this work. 107
Table 5.1. Viscosity of G2 and DiDBE electrolytes at different temperatures
Table 5.2. Calculated solvation energy and coordination numbers of O in FSI anion and solvent in different electrolytes by MD simulation. 117
Table 5.3. ICP-MS result of Mn residue proportion at the separator in MnHCF K cells with DiDBE-D and EC/DEC electrolytes after 150 cycles

Chapter 1. Introduction

1.1 Development of Potassium Ion Batteries

The soaring demand for energy storage cannot be fully satisfied by lithium-ion batteries (LIBs) alone, taking into account the limited Li resources. Therefore, other rechargeable batteries featuring sufficient reserves and high energy are intensively pursued. Considering the similarity in chemical properties of alkali ions, sodium-ion batteries (SIBs) and potassium-ion batteries (PIBs) regained the interest of the community for sustainable development. Their resource abundance (300 times over Li) and similar working principles¹ make them promising candidates (**Table 1.1**).

Table 1.1. Comparison between LIB and potential substitutes.

	Li	Na	K
Standard electrode potential in aqueous solution (V, vs. SHE)	-3.04	-2.71	-2.93
Electrode potential in carbonate electrolytes (V, vs. Li ⁺ /Li) ²	0	0.3	-0.1
Resource abundance (wt.%)	0.0065	2.27	2.1
Cost of industrial-grade metal (US dollar ton ⁻¹)*	100770	2580	13000
Substrate	Cu	Cu or Al (Cheap)	Cu or Al (Cheap)

^{*}Data was obtained from the latest report from Shanghai Metals Market in Aug 2024.

Among the Li, Na, and K, K possesses the lowest redox potential in the organic

carbonate electrolytes², suggesting a promising future for high-voltage PIBs for realized competitive energy densities. Compared to LIBs, another advantage of PIBs lies in the applicability of the cost-effective and lightweight Al foil collector on both the cathode and anode side because of the absence of K-Al alloying. The research in PIBs can be classified into three parts, cathodes, anodes, and electrolytes.

1.2 Cathode

Several types of cathodes, including layered oxides, polyanion compounds, and Prussian blue analogs (PBAs), have been reported with decent electrochemical performance, whose characteristics are summarized in **Table 1.2**. Layered oxides like $K_xCoO_2^3$ and $K_xMnO_2^4$ exhibit a relatively low working potential and inferior capacity, ascribed to the sluggish transfer of a large radius of K ions. Polyanion compounds Kion cathodes like KVPO₄F⁵ and K₃V₂(PO₄)₂F₃⁶ can deliver a decent capacity with a higher working potential than that of layered oxides. Specifically, stoichiometric KVPO₄F exhibits over 100 mAh g⁻¹ at 2.0-5.0 V with an average discharge potential of 4.2 V, the highest working potential so far for PIB cathodes. Nevertheless, the development of such polyanion compounds is hindered by the lack of the proper electrolyte and the structural degradation. In contrast, a couple of specific PBAs including potassium iron hexacyanoferrate (FeHCF) and manganese potassium hexacyanoferrate (MnHCF) deliver a longer lifetime. The development of different cathodes is summarized in the following sections.

Table 1.2. Comparison of three typical cathode materials including $K_{0.4}CrO_2$, $K_2MnFe(CN)_6$, and $KVPO_4F$ for PIBs.

	Layered Oxide (K _{0.4} CrO ₂ ⁷)	Prussian Blue Analog (K ₂ MnFe(CN) ₆ ⁸)	Polyanionic Compound (KVPO ₄ F ⁹)
Structure			
Working potential (V vs. K+/K)	~2.5	~3.8	~4.2
Capacity (mAh g ⁻¹)	~85	>120	~80
Lifespan	~100	~300	~200
Density	Heavy	Light	Light

1.2.1 Oxides

The layered transition-metal oxides K_xTMO_2 (TM=transition metal) mainly conclude three types: P2, P3, and O3. P and O represent the structure of prismatic and octahedral ons, respectively. "2" and "3" present the oxide-layer number in a unit crystalline cell. For instance, the O3 crystal conveys an "ABCABC" stacking pattern with the space group of R-3m. These phases, such as O3' (0.75<x<1), P2 (x<0.6), and P3 (x<0.5), can be synthesized through the solid-state method. Up to now, apart from the stoichiometric

O3-KCrO₂, the *x* in other potassium-based oxides is less than 0.5 with the substoichiometric K. That is ascribed to the strong K-K interaction, leaving the limited K contents in the as-prepared oxides. Moreover, the voltage profiles of these cathodes have steep slopes (**Figure 1.1**), as a result of the larger interlayer distance¹⁰ with poor electrostatic repulsion between K ions.

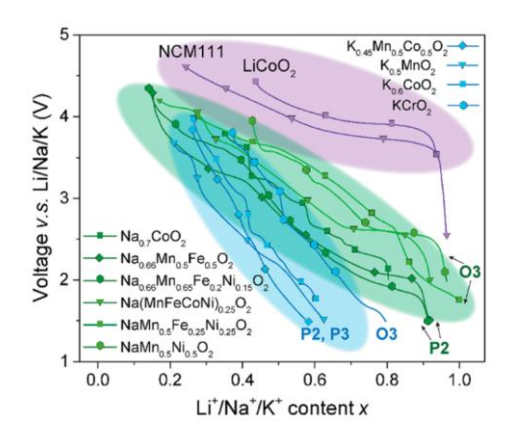


Figure 1.1. Voltage profiles for alkali-metal layered oxides. The shadow parts indicate the similar profiles of different oxides. Reproduced with permission¹⁰. Copyright 2020. American Chemical Society.

1.2.2 Prussian Blue Analogs

Potassium-type PBAs can be generally determined by the following formula, $K_xM_1^{III}[M_2^{II}(CN)_6]_{1-y}\circ_y\cdot zH_2O$ ($0 \le x \le 2$, $0 \le y \le 1$) [M_1 and M_2 stand for transition metal ions, \circ represents the $M_2^{II}(CN)_6$ vacancy formed during the synthesis, and H_2O exists as the coordination water in PBAs]. When M_1^{III} is fully reduced to a di-valent state with the intercalation of K ions, the product with K-content maximum ($K_2M_1^{II}[M_2]$

 $^{II}(CN)_6]\cdot xH_2O)$ is Prussian white. The material with limited K or even K-free $(M_1^{III}[M_2^{III}(CN)_6]\cdot xH_2O)$ is described as Berlin green¹¹.

Previously-reported typical K-poor phases conclude FeFe(CN)₆ and K_{0.22}Fe[Fe (CN)₆]_{0.805}·4.01H₂O. An excellent rate performance of 89 mAh g⁻¹ at 20 C is achieved when used as the PIBs cathode. The volume variation in such a structure is calculated as 1.18% through XRD tests, which approaches the value of the zero-strain material Li₄Ti₅O₁₂ in LIB. K-rich PBAs (Prussian white) have attracted intensive interest in recent years. The first K-rich PBA for PIBs (K_{1.89}Mn[Fe (CN)₆]_{0.92}·0.75H₂O, as shown in **Figure 1.2a**) was reported by the Goodenough's group¹² utilizing saturated KCl or NaCl solution as the precipitation environment in 2017. The coexistence of low-spin Fe³⁺/Fe²⁺ and high-spin Mn³⁺/Mn²⁺ benefits the achievement of a high working potential of 3.8 V and a remarkable specific capacity of 142 mAh g⁻¹ at 0.2 C in the 2.5-4.6 V voltage window. However, the low-concentrated electrolyte (saturated KClO₄ in PC, about 0.01M) results in an obvious polarization, leading to a relatively low discharging potential. Moreover, the existence of interstitial water and Fe(CN)₆ vacancies deteriorates the cyclic and structural stability. Furthermore, the intrinsic electronic conductivity restricts the rate capability. Therefore, the primary objective to optimize PBAs is the crystallinity and electronic conductivity enhancement.

Synthesis conditions significantly affect the crystallinity and particle sizes of

PBAs. Various chelating agents like potassium citrate, ethylenediaminetetraacetic acid dipotassium salt dihydrate (EDTA-2K)⁸, and trans-1,2-cyclohexanediaminetetraacetic acid (Cydta)¹³ can form the complexation with transition metal ions and then control the speed of co-precipitation. The addition of EDTA-2K is confirmed to help suppress the ultrafast nucleation and growth, then promoting the larger crystalline sizes with higher crystallinity. Tailoring the morphology is considered a useful strategy to decrease the vacancies and enhance the kinetics. Mai et al.¹⁴ prepared flower-like $K_{1.4}$ Fe[Fe(CN)₆]₃ by a dissolution-recrystallization method utilizing HCl and DMF as the surfactants and an appropriate aging time. Such material conveys a capacity of 71 mAh g⁻¹ at 50 mA g⁻¹ and retains over 75% capacity after 100 cycles.

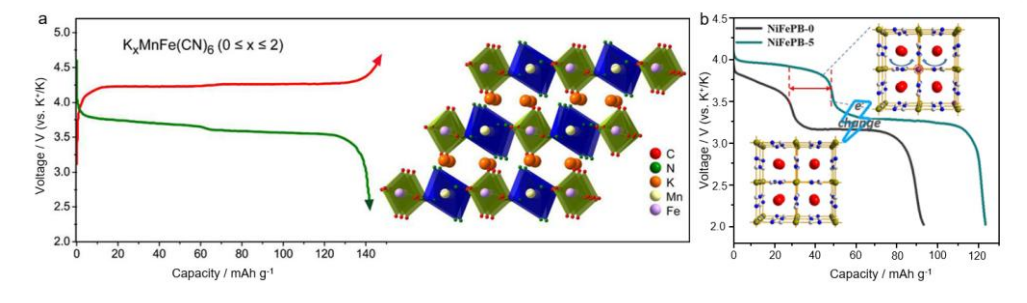


Figure 1.2. (a) Charging-discharging profile for K_{1.89}Mn[Fe(CN)₆]_{0.92}·0.75H₂O. Reproduced with perssion¹². Copyright 2017. American Chemical Society. (b) Initial discharging profile of K₂Ni_{0.05}Fe_{0.95}Fe(CN)₆ (NiFePB-5) and K₂FeFe(CN)₆ (NiFePB-0). Reproduced with permission¹⁵. Copyright 2019. American Chemical Society.

Considering that NiFe-PBA serves almost as a "zero-strain" material, Ni substitution for Fe has been applied to achieve the high-performance FeFe-PBA. Huang

et al.¹⁵ found that changing N-coordinated Fe to Ni with higher electronegativity will cause an electron cloud shift from Fe-C bonds to N-Ni bonds. Such shift corresponds to the valence rise of Fe, together with the improving Fe²⁺C₆/Fe³⁺C₆ redox (low-spin state) activity. As depicted in **Figure 1.2b**, KNi_{0.05}Fe_{0.95}Fe₀

1.2.3 Polyanion Compounds

Similar to PBAs, polyanionic compounds possess a three-dimensional open framework structure that would promise fast ionic diffusion. Vanadium and iron-based fluorophosphate and phosphates like KVPO₄F, KVOPO₄, and KFeSO₄F have been reported with limited volume changes. As depicted in **Figure 1.3**, compared to the layered oxides, polyanionic compounds perform higher volumetric and gravimetric energy. Commonly, the polyanionic compounds display a relatively high redox potential, such as 4.3 V for V⁴⁺/V³⁺, which poses a threat to the anodic stability of electrolytes. Moreover, the stability of these polyanionic cathodes in the electrolyte is a potential issue due to the dissolution of vanadium species¹⁶ and the possibility of fast self-discharge¹⁷.

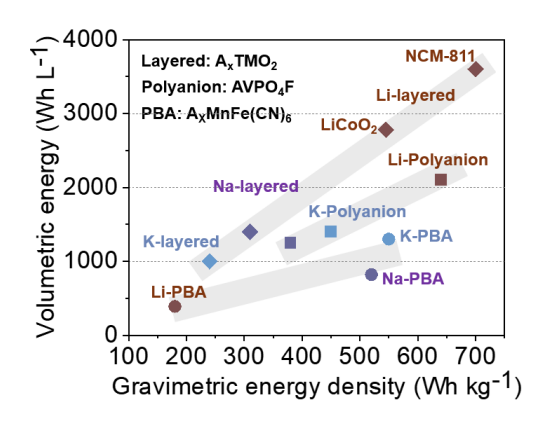


Figure 1.3. Comparison of volumetric energy and gravimetric energy of layered oxides (A=Li, Na, K; TM=Co, Mn, Ni, etc.). Reproduced with permission¹⁰. Copyright 2021. American Chemical Society.

1.3 Anode

Ideal anodes for PIBs should exhibit characteristics like low working potential, low cost, high specific capacity, superior cyclic durability, and environmentally benign. A low redox potential of the anode is the premise of realizing the high energy density of the full cell when combined with a cathode. Typical anodes can be classified into five categories according to the K ion storage mechanism: (i) Intercalation. (ii) Alloying. (iii) Conversion. (iv) Conversion-alloying and (iv) K metal anodes through plating/stripping. A detailed introduction will be provided in the following sections.

1.3.1 Carbonaceous Materials

Carbonaceous materials have been regarded as the most promising candidates as anodes in PIBs owing to their low cost, excellent electronic conductivity, and facile large-scale

production capability. C atoms in carbonaceous materials generally contain three hybrid orbitals sp, sp^{2,} and sp³. Carbonaceous materials with single sp and sp³ are usually difficult to accommodate K ions because of their irregular structures and are rarely utilized as anodes. Other carbonaceous materials with sp² hybrid or sp²/sp³ complex hybrid orbital exhibit excellent properties. Typical carbonaceous materials include graphite, soft carbon, and hard carbon, with properties illustrated in **Figure 1.4**.

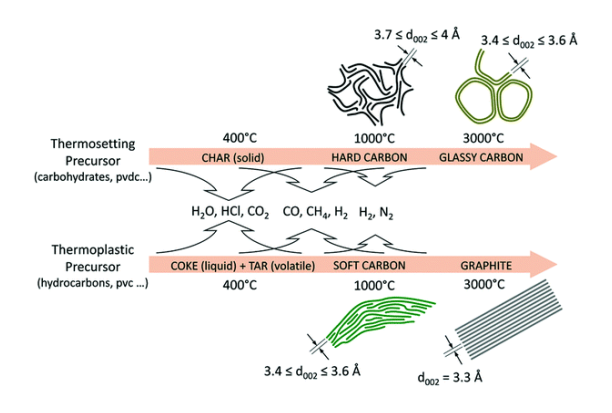


Figure 1.4. Typical carbon-based materials with characteristic structures. Reproduced with permission¹⁸. Copyright 2018. Wiley-VCH.

Graphite possesses well-ordered graphitic domains, enabling the intercalation behavior of potassium ions with a low working potential. Soft carbon has a high graphitization degree and exhibits a relatively long-range ordered graphitic domain, which usually requires a high synthesis carbonization temperature to acquire high crystallization. Hard carbon, a kind of carbon material showing a poor graphitization degree even at high temperatures, possesses defects, pores, and short-range graphitic domains as different active sites to accommodate alkali ions. The detailed mechanism

of these carbon-based anodes is discussed in the following.

Graphite

Soft Carbon (SC)

Mizutani et al. 19 discovered the K ion intercalation behavior in graphite and the formed binary K-graphite intercalation compounds (GICs) in 2-methyl tetrahydrofuran and 2.5dimethylte tetrahydrofuran electrolyte. In 2015, Ji's group²⁰ displayed the structural evolution of graphite upon cycling using ex-situ X-ray diffraction (XRD) and proposed the charge storage mechanism in the initial cycle. During discharging, GIC with a high stage number (KC₃₆ stage III) was first observed when the voltage came to around 0.25 V, followed by the KC₂₄ stage II appearing at 0.15 V. Finally, the stage I pure KC₈ with an orange color was discovered near 0.01 V. Upon charging, the conversion from KC8 to KC₃₆ is not completed until above 0.3 V without the observation of KC₂₄. Eventually, the (002) peak with a tiny shoulder re-emerged in the final charging state, indicating the reversible reaction process. Since graphite anode was found to exhibit a remarkable capacity, PIBs have aroused worldwide attention as a promising substitute. Nevertheless, the volume expansion caused by KC₈ is about 60% (compared to ~11% in the formation of LiC₆), which poses a challenge to cycling stability.

Typical soft carbon, characterized by a prevalence of hexagonal carbon rings and a limited presence of pentagonal rings near boundaries and defect areas, exhibits a

turbostratic arrangement of carbon layers. Thermoplastic precursors like hydrocarbon and polyvinyl chloride (PVC) are the main precursors for soft carbons²¹. Soft carbons exhibit a higher rate performance than hard carbons and conventional graphite anodes. This is ascribed to their partly ordered carbon structures with slightly larger interlayer distances, which facilitate faster ion transport. Additionally, they normally have a higher tap density than hard carbons because of a more compact structure and a lower porosity. The cyclic stability varies in the reports, caused by different fabrication techniques and precursors, both of which have significant effects on the microstructures and their subsequent charge storage performances. Owing to the abundant short-range ordered graphitic domains in soft carbons, the K ion storage behavior in soft carbon is mainly intercalation.

Hard Carbon (HC)

Hard carbon with a low graphization degree, is commonly synthesized through carbonizing the thermosetting polymers like lignin, cellulose, starch, sucrose, and glucose under an ambient atmosphere. Hard carbon typically contains defects on its edges, as well as nanopores, and short-range graphitic domains depending on carbonization temperature¹⁸. Meanwhile, rich nanopores are present in the hard carbon resulting from the irregular growth of the carbon layers during synthesis. The short-range graphitic layers usually possess a broader layer distance, which is more adaptable

for the volume expansion during K ion insertion. The adsorption behavior of K ion on the defects of hard carbon surfaces in the early stage of discharging with high potential can be realized with fast kinetics. It implies a superior rate performance of hard carbon compared to that of graphite at the expense of the working potential. In addition to excellent rate performance with high cyclic stability, high capacity at the low-voltage region is the pursuit for hard carbon to realize more favorable overall energy density when coupled with cathodes. However, till now, there has been no agreement regarding the K ion storage mechanism in hard carbon at the low-voltage region. Whether the pore-filling or intercalation behavior of potassium ions accounts for the capacity at the region is still under debate.

1.3.2 Conversion and Alloying Types

Conversion-type anodes usually are transition metal compounds TM_aX_b (TM=transition metal, X=O, S, Se, Te, P, and F). These materials store K ion by the phase conversion between compounds and transition metal single substances: TM_aX_b + (bn) K^+ + (bn) $e^- \leftrightarrow a TM + b K_nX$, where n represents the oxidation state of X anion. These conversion reactions occur with multiple-electron transfer, indicating the high theoretical capacity for conversion-type materials. Nonetheless, the phase conversion commonly takes place together with the typical structural pulverization, which leads to the loss of cohesion from the current collector and a decline in capacity.

Group IV and V A elements, like Ge, Sn, Pb, P, Sb, and Bi are typical alloying-type anodes for PIBs. These materials accommodate the potassium via a reversible (de)alloying process: $xA+yK^++ye^-\leftrightarrow A_xK_y$. The IVA elements (Ge²², Sn²³) can only react with one K ion to form stable alloys, leaving relatively low capacities. In contrast, the stable K₃Sb²⁴ and K₃Bi²⁵ phases (**Figure 1.5**) endow the Sb and Bi anodes with the theoretical capacities of 660 and 385 mAh g⁻¹, respectively. P-K alloys like K₃P, K₄P₃, or KP possess even higher theoretical capacities of 2597, 1154, or 865.6 mAh g⁻¹ but suffer from unstable P substance that may restrict the practical application.

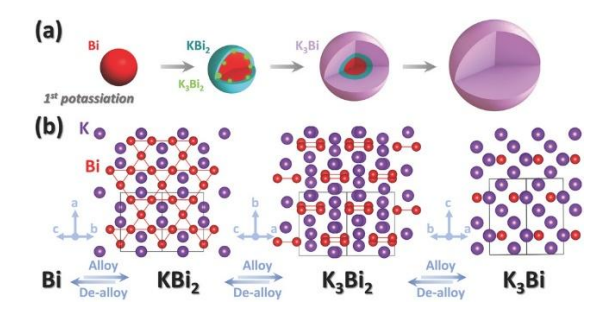


Figure 1.5. The potassium storage mechanism of alloying-type materials, taking the Bi as an example. Reproduced with permission²⁵. Copyright 2018. Wiley-VCH.

Compared to intercalation-type anodes, these alloying anodes suffer from more severe volume change and even pulverization especially during multi-electron-transfer reactions (407% for K₃Sb and 406% of K₃Bi *vs.* 60% for KC₈). To alleviate this issue, nano-sized engineering is employed to effectively shorten potassium-ion transfer distance. It usually combines a conductive carbon matrix to accommodate the volume expansion and enhance electric conductivity. Binary, ternary, and high-entropy solid

solutions formed by alloying several metals Sn, Sb, or Bi could also achieve superior electrochemical performance compared to the single-phase counterparts.

Apart from pure conversion and alloying materials, conversion-alloying hybrid types also serve as the anodes. These anodes commonly consist of oxides, sulfides, selenides, tellurides, and phosphides for IV A and VA elements including Ge, Sn, Pb, Sb, and Bi. Their K ion storage mechanism does not only involve the cation conversion but also the following alloying process of metal substances, which can be concluded as $TM_aX_b + (bn+m) K^+ + (bn) e^- \leftrightarrow K_mTM_a + b K_nX$ (TM= Ge, Sn, Pb, Sb, Bi. X=O, S, Se, Te, P). In the first step, metal anions react with K ion and convert into the transition metal single substance and K_nX . Subsequently, the TM substance alloys with K ion to form K_mTM_a . The K_nX plays a role as a solid electrolyte to transfer the K ion and offer a buffer space for the accommodation of volume expansion during the alloying process²⁶.

1.3.3 Potassium Metal

Potassium metal stood out as an anode for PIBs in 2016 owing to its unique merit of low redox potential (-2.93 V vs. SHE), large abundance (~2.1 wt.%), and high theoretical capacity (685 mAh g⁻¹)² compared to the above-mentioned anode materials (as illustrated in **Table 1.3**). Plating and stripping behaviors of K ion on the K anode will occur along with the extraction and insertion of K ion in cathode materials.

However, there are still a series of challenges to be handled before application. First is the uncontrollable formation of K dendrite, which can result from uneven charge distribution and K ion flux caused by the "tip effect" resulting from intrinsic defects on K metal. Consequently, cell failure caused by short circuits and thermal runaway will happen²⁷. Second, the unstable SEIs will cause the progressive consumption and even exhaustion of electrolytes²⁸. Accordingly, the inferior Coulombic efficiency and poor cycling performance cannot guarantee durable K anode stability. The low melting temperature (~64 °C) of K metal is another concern for its practical utilization due to the uncontrollable penetration of liquid K at high temperatures. Several strategies, including host design^{29, 30}, artificial interface including potassiophic species³¹⁻³⁴ or polymer coating³⁵, electrolyte design³⁶⁻³⁸, and designing the cycling protocol in the first several cycles³⁹ have been put forward to cope with these issues.

Among these modification strategies, the carbon-based host is widely utilized to buffer the volume variation and promote both electron and ion transfer^{40, 41}. These hosts possess characteristics including lightweight, high electronic conductivity, compatibility with electrolytes, and affinity with the K metal anode. For instance, porous N-doped carbon nanofibers⁴⁰ with dispersed Zn exhibit extreme potassiophilicity leading to the ultralow nucleation overpotential of 15 mV at 0.5 mA cm⁻² for K metal anode. It is reported that double element doping, including N-O, B-O,

and P-O, would form a stronger local dipole with adjacent carbon atoms, which enables tightly absorbing behavior towards K ion driven by the robust ion-dipole force⁴². Under this guidance, P-binding porous multichannel carbon nanofibers (P-CNF, with P-O and P-N bonds inside) are designed for potassium metal batteries and endow the PTCDA||K@P-CNF with high capacity retention (85%) after 1000 cycles²⁹. However, the relatively low average discharge potential of below 2.5 V for the PTCDA cathode is still unsatisfactory to achieve high energy density.

Table 1.3. Comparison of three typical anode materials for PIBs.

	Carbonaceous Materials	Conversion and alloying types	Potassium metal	
Charge storage mechanism		K ⁺ • - ₩ - ₩ K ⁺	K [†] K [†] Plating-stripping	
Working	~0.2 (Graphite& SC)			
potential (V vs. K+/K)	≥0.5 (HC)	0.6	0	
Capacity (mAh g ⁻¹)	<350	>400	685	
Drawbacks	Limited capacity	Huge volume expansion >300%	Dendrite growth; Unstable interphase	

1.4 Electrolyte

Apart from the cathode and anode, the electrolyte is a critical part of the battery systems as well. To shield electric channels and guarantee the ionic transport between cathodes

and anodes, the electrolyte acts as the important transfer medium in the cell. The intrinsic properties of electrolytes and generated interphases significantly impact the overall performance of the batteries.

The most used electrolytes are liquid electrolytes, which can be classified into carbonates, phosphates, and ethers according to the different functional groups, which will be discussed in the following parts. With the growing requirement for safe and high-powered energy-storage systems, researchers are actively investigating various aspects of electrolytes to alleviate the challenges in PIBs. One key direction is expanding the electrochemical windows, which can enable batteries to operate at higher voltages without degradation or hazardous side reactions. Another important focus is improving the thermal stability of electrolytes. As heat generation occurs inside the battery during the operation, it can lead to thermal runaway and potential safety hazards by releasing flammable gases if the electrolyte is not thermally stable. Furthermore, enhancing the ionic conductivity of electrolytes is also a crucial focus for improving the rating capability. In the following sections, the detailed classification of solvents and salts together with tailoring electrolyte engineering will be discussed separately.

1.4.1 Solvents and Salts

Carbonates

Carbonate electrolytes containing one or multiple kinds of carbonyl-radical (O-C=O)

carbonates include cyclic carbonates (ethylene carbonate, EC, and propylene carbonate, PC) and linear carbonates (dimethyl carbonate, DMC, ethyl methyl carbonate, EMC, and diethyl carbonate, DEC).

Cyclic carbonates with a ring-like structure have a high dielectric constant thus facilitating the dissociation of potassium ions for an enhanced ionic transport⁴³. Moreover, cyclic carbonates are known to readily decompose on the anode during the initial charge-discharge cycle to form a SEI layer. This layer is crucial for the stability of the battery to prevent electrolytes from further decomposition and maintain the integrity of the anode. However, the SEI layer formed by cyclic carbonates is relatively thick and unstable, which increases the interfacial resistance and decreases the battery's capacity⁴⁴.

On the other hand, linear carbonates have a straight-chain structure. They have lower viscosity and higher ionic conductivity than cyclic carbonates, which guarantees the kinetics and rate behaviors of the battery. However, linear carbonates are less likely to form a stable SEI layer on the anode⁴⁵, which can lead to continuous electrolyte decomposition and poor cycling stability. Moreover, they possess a lower dielectric constant than cyclic carbonate and pose a challenge to the solvation of potassium ions and their transport. Therefore, in practice, mixed linear and cyclic carbonate-based

electrolytes are often used for potassium-ion batteries to achieve a balanced performance⁴⁶. The cyclic carbonate provides a high dielectric constant for good cation solvation and forms an initial SEI layer, while the linear carbonate ensures the kinetics behavior.

Phosphate Solvents

Phosphate electrolytes are typically composed of organophosphate solvents (**Figure 1.6**), including trimethyl phosphate (TMP), triethyl phosphate (TEP), and tris(2,2,2-trifluoroethyl) phosphate (TFEP)³⁷ with ionic-conductive potassium salt dissolved. These solvents have a high dielectric constant and good solvation ability for potassium ions, which can facilitate ion transport and improve the power density.

Figure 1.6. Typical phosphate solvents derived from TMP.

One of the key advantages of phosphate electrolytes is their thermal stability. Unlike carbonate electrolytes, which can decompose and produce $H\cdot(RH\to R\cdot +H\cdot)$, $OH\cdot(H\cdot +O_2\to OH\cdot +O\cdot)$ free radicals, and finally release flammable gases at high

temperatures, phosphate electrolytes are stable and safe even under extreme conditions benefitting from the H· catcher [P]· or [PO]· radicals ([P]·+H· \rightarrow [P]H)^{47, 48}. This makes them typically applicable for scalable energy storage systems, where safety is a major concern. Nevertheless, most phosphates exhibit poor compatibility with anodes including graphite, K metal, and alloy-like Sb.

Ether Solvents

Compared to the carbonates and phosphates, ethers with R-O-R (R represents CH₂ groups) functional groups possess high compatibility with potassium metal anode and graphite anode. They can also be divided into two types, i.e., linear ethers and cyclic ones. Linear ethers, such as dimethoxyethane (DME) and diglyme (G2), have a straight chain structure. Cyclic ethers, like 1, 4-dioxane (1,4-DX)⁴⁹, and THF have a ring-like structure and exhibit a weaker solvating ability than the linear structural ones with the same O atoms number. These solvents can induce more C-O bonds corresponding to the PEO-like [CH₂CH₂O]_n organic components in the SEI and cathode electrolyte interphase (CEI) layers, resulting in higher flexibility. Furthermore, the layers generated in the ethers are even and thinner than those in carbonates, decreasing the interphase resistance. Most recently, Lu et al. 49 introduced 1,4-DX as the nonfluorinated diluent into the TMP-based electrolyte. The weak K ion-1,4-DX interaction prevents the co-intercalation of K ions in the graphite anode and enhances the stability of PIBs.

Nevertheless, the oxidative stability of ether electrolytes is inferior compared to that of esters. Further research, like the molecules design via modifying the terminal functional groups, is required to optimize these solvents and develop new ones that can enhance the performance of PIBs, as will be discussed in section 1.4.2.

Potassium Salts

The common potassium salts are potassium hexafluorophosphate (KPF₆) and potassium bis(fluorosulfonyl)amide (KFSI). There are also other salts like potassium tetrafluoroborate (KBF₄), and potassium perchlorate (KClO₄). The solubility of salts in common a carbonate electrolyte were compared in the previous work¹. KFSI and KPF₆ salts exhibit higher solubility and enable a high ionic conductivity of 8.1 and 6.2 mS cm⁻¹, respectively. However, KBF₄ and KClO₄ are hardly dissolved in the carbonate electrolytes (Table 1.3) and result in a low ionic conductivity, which largely restricts their application as potassium salt in electrolytes. For instance, MnHCF||K cell could be reversibly cycled in the saturated KClO₄ in PC (about 0.01M) but exhibits a significant polarization with unclear redox reaction-related plateau, which significantly impedes interior ionic transport and affects the electrochemical performance¹². KFSI exhibits the highest solubility in most solvents and has been widely used. Nevertheless, the normal concentration of KFSI in either ester or ether cannot afford the high-voltage MnHCF cathode due to the Al corrosion from soluble product Al(FSI)_x. Increasing the concentration of salt^{50, 51} can alleviate the Al corrosion and enhance the electrolyte stability at high voltages but with a cost penalty.

Table 1.4. Comparison between different potassium salts for electrolytes.

	KFSI	KTFSI	KPF ₆	KBF ₄	KClO ₄
Structure	0 K 0 F-S-N-S-F 0 0	N-3-F F-0 F	Ertre	F B K	O=CI-O K ⁺
Solubility in PC (mol L ⁻¹)	>1	>1	1	<0.01	~0.01
Cost (US dollar g ⁻¹)*	15	21	3	0.6	0.8
Advantage	High ionic conductivity; Stable anode surface	High ionic conductivity; Stable anode surface	High oxidative stability	High oxidative stability	High oxidative stability
Disadvantage	Al corrosion	Al corrosion	Limited solubility; Unstable anode surface	Poor solubility	Poor solubility

^{*} Data was obtained from TCI chemical company.

Generally, carbonates, phosphates, and ethers are widely utilized as the solvent in PIBs. Carbonates possess wider electrochemical windows while inferior compatibility against the anode. Phosphates have high stability at elevated temperatures and induce a stable CEI, but their ionic conductivity is limited. Ethers are likely to boost the kinetics through their weak solvating ability, however, their anodic stability is inferior.

Therefore, tailoring solvents or salts with some effective strategies is needed to concurrently resolve the interface issues at both the cathode and anode sides.

1.4.2 Molecules Design of Solvents

Fluorinating emerges as one of the most promising strategies for enhancing oxidative stability. Owing to the great electron-withdrawing power of fluorine-substituted groups, both the highest occupied molecular orbital (HOMO) and the lowest unoccupied molecular orbital (LUMO) energy levels can be lowered, thereby increasing the oxidation stability of the electrolyte. Additionally, the electron-withdrawing effect of F would attract electrons of O atoms, thereby weakening the solvating ability. The resulting anion-rich solvation structure gives rise to anion-derived CEI/SEI with enhanced inorganic components including KF ⁵². Lu et al.³⁷ introduced a fluorinated phosphate FTEP-based electrolyte (1M KFSI in FTEP) to enable durable and safe PIBs via forming anion-derived SEI on graphite anode and enhancing oxidative stability. It endows K_{0.2}MnO₂||graphite full cell for 100 cycles with an average Coulombic efficiency (ACE) of over 99.7%.

Considering the uncertain environmental issues arising from F atoms, other molecule designs have been put forward, including reducing the number of O atom ratios in ethers to enhance anodic stability⁵³ and chlorinating the ending group⁵⁴. Accompanied by the reducing coordinated sites (O atoms) for K, the K ion-solvent

interaction can be weakened, indicating a lower desolvation energy barrier and a smoother desolvation process^{55, 56}. It is promising to achieve superior rate performance and low-temperature compatibility in PIBs coupled with weakly solvated electrolytes. As for the chloro-substituting modification, Lu's group⁵⁴ recently proposed that chlorine can withdraw the electron density around O atoms in the solvent due to the relatively high electronegativity and serve as another site for weak K-Cl interaction. A halides-based SEI protects electrodes and enables the full cell with superior stability at the high voltage.

1.4.3 (Localized) High Concentration of Salts

Electrolytes with high concentrations have emerged as an effective design in past years benefitting from their inflammability and compatibility with high-voltage cathodes. The high concentration of salt would surround the solvent molecules to reduce the free solvent in the electrolyte. In these salt-concentrated electrolytes, ion pairings of FSI anion and K ion increase, which can extract the solvent out of the first solvation shell of K ion and finally induce an anion-derived interphases^{50, 51}. It also prevents the free solvent from corroding the aluminum current collectors⁵⁷. Nevertheless, the highly concentrated salt will also lead to high viscosity and poor wettability, which decreases the ionic mobility and seriously impacts the performance at a low temperature. Moreover, considering the high cost of the highly concentrated salt, such kind of

electrolyte is inapplicable for scalable production.

To retain the benefits of highly concentrated electrolytes while maintaining low viscosity, diluent solvents are incorporated to create regions of localized high concentration within the electrolyte. Several diluents including 1,1,2,2-tetrafluoroethyl-2,2,2-trifluoroethyl ether (HFE) have been effectively introduced into ether-based and phosphate-based electrolytes to promote the cyclic stability of PIBs. For instance, the diluent HFE serving as an antisolvent possesses the lowest electrostatic potential (ESP) difference between the minimum and maximum values than the common solvating solvent⁵⁸. When corporate into the KFSI/diglyme electrolyte, the synergic decomposition of the F-containing HFE and FSI-derived KF-rich SEI enhances the oxidative stability and promotes the Coulombic efficiency⁵⁹.

1.5 Objective and Outline

The above discussion suggests that the development of PIBs is still at an early stage, leaving many issues unresolved. Interfacial stability is among the most challenging issues afflicting the stability of PIBs. Therefore, the major objective of this thesis is to build stable interfaces at both the anode and cathode side through electrode/current collector modification and electrolyte engineering.

Accordingly, Chapter 2 presents the detailed experimental procedures including the preparation of materials, characterization, and theoretical simulation. In Chapter 3,

we studied the charge storage behavior of K ion in hard carbon to understand the capacity contribution at the low voltage region. A weakly solvating electrolyte was developed to promote the rate performance and low-temperature compatibility of carbon anodes by tuning the desolvation process and SEI microstructure. In Chapter 4, considering the lightweight and the inferior capacity of carbon materials, we unveiled the function of carbon nanofiber as the decoration of the current collector to regulate inorganic-organic ingredients of SEI by suppressing the electrolyte decomposition. Meanwhile, the nucleation behavior is regulated by incorporating Ni species to enable long lifespan K metal anodes. Chapter 5 extends the interface regulation from the anode side to the high-voltage cathode. We designed a dilute electrolyte for stable highvoltage PIBs with K metal anodes by combining the steric hindrance with the filmforming booster to generate stable SEI/CEI with high ionic conductivity and elasticity. Finally, Chapter 6 summarizes the major findings and presents the plan for future work.

Chapter 2. Experimental Section

2.1 Materials Synthesis

2.1.1 Pistachio-derived Hard Carbons

Pistachio shells (4 g), the hard carbon's biomass precursors, were the first ball milled (HEBM, spex8000) for 10 mins to crush them into fine powder. Subsequently, it was calcined at different temperatures ranging from 1100-1300 °C for 1 h in Ar at a ramping rate of 5 °C min⁻¹. The obtained product was washed with diluted HCl to remove the impurities. Specifically, the as-annealed black powder was soaked in a 30 ml 1M HCl solution and stirred for 6 h at room temperature. After drying at 60 °C under a vacuum oven, the final hard carbon anode materials were collected, showing an 18wt.% yield refers to the weight of the pistachio shells. For KOH-treated samples, an extra hydrothermal process by soaking the pistachio shells in 30 mL 1.5M KOH solution at 165 °C for 6 h, rinsing with deionized water, and drying at 80 °C overnight was applied before the ball-milling. The other procedures are identical to the one without KOH treatment.

2.1.2 Carbon Nanofibers (CNFs)

To prepare the lignin-based CNFs, 1 g of lignin (kraft, Alfa Aesar) and 0.5 g polyacrylonitrile (PAN, Mw 150,000, Sigma Aldrich) were dissolved and stirred in 10 mL N-dimethylformamide at 60 °C overnight. Afterward, the lignin-PAN solution was

electrospun into the nanofiber film under the high voltage of 18 kV with the feed rate of 1 mL h⁻¹, which was collected on the Al foil and peeled off after the electrospinning. Then a stabilization process with a ramping rate of 0.5 °C min⁻¹ at 250 °C for 1 h in the muffle oven was applied to improve the thermal stability of PAN during subsequent carbonization. Finally, the CNFs with a yield of 42% were collected after annealing at 1350 °C for 2 h with the heating rate of 3 °C min⁻¹ in the tube furnace under Ar flow.

The preparation of PAN-based CNFs is similar to the previous one, except for the pure PAN precursors of 12% in DMF solution and the annealing temperature of 1400 °C for 2 h with a heating rate of 5 °C min⁻¹ under Ar flow.

2.1.3 Lignin-based Hard Carbon Powder

For the preparation of lignin-based powder (LigP), lignin powder was first pre-treated at 200 °C for 1 h in the oven in the air atmosphere and then carbonized at 1350 °C for 2 h under argon.

2.1.4 CNFs Grown with Nickel Species (CNFNis)

Before the synthesis of CNFNis, the initially prepared CNFs were rinsed in ethanol, and dried in a 60 °C oven (such rinse and drying process is referred to as RD for convenience). An RD was followed by immersing the CNFs into 20 mL 0.1M NiCl₂·6H₂O aqueous solution for overnight pre-electrostatic adsorption. After undergoing RD with deionized water, processed CNFs were immersed into 40 mL

ethanol solution of NaBH4 for 10 mins to preliminarily generate nuclei, followed by another RD. Subsequently, twice-processed CNFs were immersed in a Ni source solution labeled as A. A was prepared by dissolving 475 mg NiCl₂·6H₂O and 5.08 g potassium sodium tartrate tetrahydrate into 92 mL deionized water, then adding 0.14 g NaOH and stirring until pH reached 13. Under the premise of the uniform dispersion of CNFs, 1.8 mL 55% hydrazine hydrate was dropped into solution A. After refluxing under the magnetic field at 120 °C for 2 h, the as-prepared Ni-CNFs can be collected by RD.

2.1.5 CNF@Al and CNFNi@Al Current Collectors

CNF@Al and CNFNi@Al were prepared by air-assisted spraying using the 50 mL well-dispersed aqueous solution containing 20 mg CNF (or CNFNi) and 2 mg carboxymethylcellulose sodium (CMCNa) onto the 10 cm×10 cm-size Al foil on a heated plate at 180 °C. Before battery assembly, the coated Al foil was punched into Φ12 mm discs and vacuum dried at 80 °C for 10 h.

2.1.6 Fe-based Prussian Blue FeHCF

The synthesis of FeHCF can be referred to a previous work⁶⁰. Briefly, 1 mmol K₄Fe(CN)₆·3H₂O (Alfa Aesar) was added to 160 mL deionized water. A 40 mL aqueous solution containing 2 mmol FeCl₃ was prepared and dropped into K₄Fe(CN)₆·3H₂O

solution under vigorous stirring for 2 h and aged for 24 h. Then the precipitate was centrifuged with deionized water and ethanol 3 times. Finally, the blue powder was collected after vacuum drying at 80 °C overnight and grinding.

2.1.7 Mn-based Prussian Blue Analog MnHCF

MnHCF was synthesized by co-precipitation with the iminodiacetic acid (H2IDA, Aladdin) as a chelating agent. Typically, 1.5 mmol manganese acetate tetrahydrate (Sigma Aldrich) was dissolved in the 25 mL of 1.5 mmol H2IDA aqueous solution. The solution was added dropwise into 37.5 mL of 1.5 mmol potassium hexacyanoferrate trihydrate (Sigma Aldrich) aqueous solution containing 9 mmol potassium citrate tribasic monohydrate (Sigma Aldrich) under Ar bubbling and vigorous stirring for around ten minutes. After stirring for 2 h and aging for another 2 h, the milk-white powder was collected by rinsing with deionized water, centrifuging three times, and drying at 100 °C under vacuum overnight.

2.2 Electrodes and Electrolytes Preparation

2.2.1 Electrodes

Hard carbon electrodes were fabricated by casting a slurry containing 90wt.% HC, 5wt.% carbon super P (SP) conductive additives, and 5wt.% CMCNa binder onto Cu foil. These electrodes with an average mass loading of 1.3 mg cm⁻² were dried in an 80 °C vacuum oven. CNFs are directly utilized as the electrodes. To prepare the MnHCF

electrode, the active material powder, SP, and poly(vinylidene fluoride) (PVDF) were mixed and ground in deionized water with a weight ratio of 6:3:1. Subsequently, the uniform slurry was cast onto the C-coated Al foil followed by the vacuum-drying at 100 °C for 10 h and punched into Φ12 mm discs. Finally, these electrodes were transferred to the Ar-filled glove box (water and O₂ contents below 0.1 ppm) for assembling coin cells (CR2032). The K metal electrode was fabricated by rolling the K chunks (98%, Sigma Aldrich) and cutting them into Φ12 mm discs.

2.2.2 Electrolytes

EC, DEC, DMC, EMC, DME, G2, tetraglyme (G4), 1,3,2-dioxathiolane 2,2-dioxide (DTD), and KPF₆ were purchased from DoDo. Chem. Tetrahydrofuran (THF) and KFSI were obtained from TCI. Di-ethylene glycol di-butyl ether (DiDBE) (99%) was provided by Sigma Aldrich. Ethylene glycol diethyl ether (DEE) (98%) was purchased from Macklin. The sodium hexafluorophosphate (NaPF₆) was provided by Kishida Chemical Co. Ltd Japan. Solvents were dried with molecular sieves for at least 24 h before use. 1M KFSI/ECDEC (EC:DEC=1:1 in vol.%), 1M KFSI/ECDMC (EC:DMC=1:1 in vol.%), 1M KFSI/ECDMC (EC:DMC=1:1 in vol.%), 1M KFSI/ECDMC (EC:DMC=1:1 in vol.%), 1M KFSI/DEC=1:1 in vol.%), 1M KFSI/DEC=1:1 in vol.%), 1M KFSI/DIDBE, 1M KFSI/DIDBE, 1M KFSI/DIDBE, 1M KFSI/DIDBE, with 6wt.% DTD additive) were prepared.

2.3 Materials and Electrolytes Characterization

2.3.1 Structure and Composition Analysis

The crystalline structure was examined by X-ray diffraction (XRD) using Cu Ka radiation (Rigaku Smart Lab 9kW). The degree of graphitization with the structural evolution of hard carbons and the elemental bonding information in electrolytes were determined by Raman (Witec Confocal Raman, with a 532 nm laser) test. The solvation structure of electrolytes was evaluated through nuclear magnetic resonance (NMR) spectroscopy using Bruker Avance III HD. For ¹⁹F spectra, 0.1M chlorobenzene (-112.7 ppm) in CDCl₃ was utilized as the standard solution. UV photoelectron spectroscopy (UPS, Thermo Fisher Nexas) analysis was exploited to determine the work functions $(\Phi = h \nu - E_{\text{cut off}})$ of current collectors with a He I X-ray source $(h \nu = 21.22 \text{ eV})$ and a negative voltage bias of 10 V. X-ray photoelectron spectroscopy (XPS) test was performed by a Thermo Fisher Nexas using a vacuum transfer unit to examine the chemical content and states. Except for the other samples, the HC-1300 samples were etched by the Ar ion beam 160 s (with the spurring speed of 0.25 nm s⁻¹) to exclude the interference of the SEI layer. Energy dispersive X-ray spectroscopy (EDS) and electron energy loss spectroscopy (EELS) on JEOL JEM-2100F TEM at 200 kV were also utilized to detect the element components. Time-of-Flight Secondary Ion Mass Spectrometry (TOF-SIMS, IONTOF TOF-SIMS M6) measurements were performed on a region of 300 $\mu m \times 300~\mu m$ with a Cs-ion sputtering at 500 eV and 50 nA within 690 s and Bi³⁺ as the analyzing ion 100 $\mu m \times 100~\mu m$ area.

2.3.2 Pores Structural Information of Hard Carbon

The open and closed pore structural information was obtained via a series of characterizations, including N₂ and CO₂ adsorption/desorption through ASAP2020 apparatus, small-angle X-ray scattering (SAXS) from Xeuss 2.0 apparatus, and true density measurement using helium as the analysis gas (AccuPyc II 1340). The volume of closed pores is calculated by the following formula:

$$V_{closed\ pores} = 1/\rho_{true} - 1/2.26 \tag{2.1}$$

Here $2.26~g~cm^{-3}$ is the true density of graphite without pores⁶¹ The volume of closed pores is over five times that of open pores obtained in CO_2 adsorption/desorption.

2.3.3 Morphology Scanning

The morphology of materials was captured through scanning electron microscope (SEM) and transmission electron microscopy (TEM, JEOL JEM-2100F). For the preparation of ex-situ TEM observation on discharged hard carbon, active materials collected from the discharged electrodes were washed and dispersed in diethyl carbonate (DEC) electrolyte in the glove box with an Ar atmosphere. Then the clear upper dispersion was dropped onto the TEM grid, shrouded in DEC to reduce the air exposure, and immediately transferred into a JEOL JEM-2100F TEM using a liquid-N₂

cooling cryo holder (Gatan 636) sheathed in a plastic cap-wrapped by Parafilm tape. High-resolution TEM (HRTEM), and scanning TEM (STEM) were conducted at 200 kV (JEOL JEM-2100F TEM/STEM) with an Oxford INCA EDS detector and a Gatan Enfina electron spectrometer as a supplementary instrument. The morphologies of SEI were captured through atomic force microscopy (AFM, Bruker, Santa Barbara, CA) in three different regions with an area of $10~\mu m \times 10~\mu m$.

2.3.4 Thermostability Measurements

The thermostability of electrolytes was tested through TG measurement based on Netzsch STA 449 F3 with a ramping rate of 10 °C min⁻¹ under N₂ flow. The stability of the cycled MnHCF cathode (cycled at 50 mA g⁻¹ after three cycles) was determined by differential scanning calorimetry (DSC, Netzsch STA449 F3) in the range of 25-250 °C with a ramping rate of 5 °C min⁻¹ under Ar flow.

2.3.5 Mechanical Properties of Solid Electrolyte Interphase

The mechanical properties of SEI were analyzed through AFM-based nanoindentation tests under an Ar-filled glovebox using a probe with a spring contrast of 21.2 N m⁻¹ and a tip radius is 25.2 nm. For each sample, more than 70 unparallel testing positions were examined to guarantee the reliability of results. There are three main factors including Young's modulus E, elastic strain limit ε_Y , and the maximum energy of elastic deformation U ($U \propto E \cdot \varepsilon_Y^5$) were compared. The detailed relationship among these

factors is shown as following⁶²:

$$E = \frac{(1-v^2)(1-e^{-\frac{\alpha t}{a}})}{\frac{1}{E_T} - \frac{1-v_{tip}^2}{E_{tip}} + \frac{1-v_S^2}{E_S}(e^{-\frac{\alpha t}{a}})}$$
(2.2),

where E_r is the reduced modulus, which could be calculated from the fitting of the retract section in the force-displacement curve from the first step of the AFM nanoindentation test (the maximum loading force is set as 30 nN), with the fitting model as the Hertz contact model⁶³ in the NanoScope Analysis software; v_{tip} , v_s and v are the Poisson's ratio of the AFM probe, the substrate K metal and the SEIs, as 0.22, 0.35 and set as 0.3, respectively; E_{tip} and E_s are Young's modulus of the AFM probe and the substrate K metal, as 160 GPa and 3.53 GPa. α is a scaling factor about the substrate effect, which can be calculated through the following equation:

$$\alpha = 0.18 + 0.67 \left(\frac{a}{t}\right) - 0.5 \left(\frac{a}{t}\right)^2 + 0.11 \left(\frac{a}{t}\right)^3 \tag{2.3},$$

where $a = \sqrt{\pi R d}$, R is the tip radius of the AFM probe adopted, which is 33.3 nm in Chapter 4 and 25.2 nm in Chapter 5, respectively. d is the indentation deposition obtained from the force curves collected in the first step of tests. t is the thickness of SEIs, obtained from the force curves of the second step.

The elastic strain limit ε_Y is calculated via the equation 2.4:

$$\varepsilon_Y = \frac{\left(\frac{6F_Y E_r^{*2}}{R^2}\right)^{\frac{1}{3}}}{1.6\pi} \tag{2.4},$$

where F_Y is the force value when the elastic deformation meets its limitation, and

$$E_r^* = \left(\frac{1 - \nu_{tip}^2}{E_{tip}} + \frac{1 - \nu^2}{E}\right)^{-1}$$
 (2.5),

Based on the values of E and ε_Y , the maximum elastic deformation energy, U, could be calculated from the equation 2.6 below:

$$U = \int_0^{d_c} Fd(d) = \frac{8}{15} \left(\frac{4}{5}\pi\right)^5 \cdot r^3 \cdot \frac{E^5}{(E_r^0)^4} \cdot (\varepsilon_Y)^5$$
 (2.6),

where r is the radius of the indenter, set as 1 μ m for all tested samples; $E_r^0 = \frac{E}{1-\nu^2}$ is for a rigid indenter.

2.4 Electrochemical Measurements

2.4.1 Cycling with Rate Performance

The half cells contain the working electrode with active materials, K or Na metal as the counter and reference electrode. One piece of GF/D separator is applied with the electrolyte of 80 μ L. For the cyclic tests between 0.005-2 V, to fully demonstrate the charge storage capability of hard carbon, a constant-voltage discharge (CVDi) at 5 mV is applied until the current is less than 2.79 mA g⁻¹ (1/100 C). LSV tests were conducted using K||Al cells with a sweep rate of 1 mV s⁻¹ using a Biologic VMP-3. K||Al cell contains 100 μ L electrolytes, one piece of GF/D towards K, and one piece of Celgard 2325 towards the Al electrode. The charge cutoff voltage of the K||Al cell is 1 V (ν s. K⁺/K). K||K cells include two K electrodes, with one piece of Celgard 2325 facing each

K electrode sandwiching one piece of GF/D, and 120 μ L electrolyte. Before the assembly of anode-free cells, MnHCF cathodes were precycled for 10 cycles to alleviate the irreversible reactions on the cathode side. The cycling and rate performance of cells were evaluated on the basis of Neware and LAND software.

2.4.2 Kinetics Behavior Probing

Galvanostatic Intermittent Titration Technique (GITT) tests were performed on the Neware tester to compare the kinetics. Electrochemical Impedance Spectroscopy (EIS) was collected through an electrochemical workstation (CHI760E) in the frequency range from 10⁵ to 10⁻² Hz with a potential amplitude of 5 mV. The values of ionic conductivity of electrolytes were determined through EIS measurements, which were conducted through two stainless steels sandwiching a GF/D filled with each electrolyte at room temperature. The ionic conductivity is calculated based on the equation: $\delta = L/(RS)$, where L is the thickness of the separator, S is the area of GF/D, and the bulk resistance R is the intercept of the x-axis. The exchange current density I_0 of the symmetric cell was obtained through Tafel curves on Biologic VMP-3. It was calculated by the intercept value of the y-axis based on the following simplified equation⁶⁴: $\eta = -\left(\frac{2.303RT}{\alpha F}\right)logI_0 + \left(\frac{2.303RT}{\alpha F}\right)logI$, where η is the overpotential, α is the electron transfer coefficient, F is the Faraday constant, R represents the ideal gas constant, and T is Kelvin temperature.

2.5 Computational Calculation

Classical molecular dynamics (MD) simulations were conducted utilizing the LAMMPS code⁶⁵ employing the generalized Amber force field (GAFF)⁶⁶. Force field parameters for FSI⁻ were obtained from the literature⁶⁷. For the LAMMPS simulations, Packmol⁶⁸ and Moltemplate⁶⁹ codes were employed to obtain the initial geometric structures and parameters. During the MD calculations, the energy minimization was performed with an energy tolerance of 10⁻⁴, and the time step of 1 fs was utilized. Subsequently, the equilibration of each system was carried out for 7 ns in the NPT ensemble, employing the Nosé-Hoover thermostat and barostat, with the pressure and temperature of 1 atm and 300 K, respectively^{70, 71}. Subsequently, another 5 ns simulations were carried out in the NVT ensemble (Berendsen thermostat, 300 K)⁷² were performed, and the final 4 ns trajectory was then utilized to gather the necessary data for analysis. Furthermore, the geometric structures were visualized using VESTA, Materials Studio, and VMD73, 74. The solvation energies of each electrolyte were calculated by DFT in the ORCA package based on the above-acquired most possible solvation structure⁷⁵. Calculations under the B3LYP-D3BJ/6-311G*⁷⁶⁻⁷⁸ and B2PLYP-D3BJ/def2-TZVP levels^{76, 77, 79} were used to perform the structural relaxation and single-point energy calculations, respectively. The implicit solvent model CPCM was considered during the calculations⁸⁰.

Chapter 3. Discovering the K-ion Pore-filling Behavior and Regulating the Interfacial Chemistry for Fast-kinetics Hard Carbon Anode

This chapter first probes the K storage behavior in hard carbon anodes in different voltage regions. The K ion pore-filling behavior at low potentials is found, besides the reported adsorption and intercalation mechanisms at relatively high ones. Changing cycling protocol and electrolyte regulation are proven useful to promote such behavior. Secondly, noting the inferior rate performance of hard carbon materials, we further explore the influence of interfacial chemistry using free-standing CNF as the electrode. A THF-based electrolyte has been constructed to boost the kinetics in hard carbons.

3.1 Introduction

The surface adsorption sites in hard carbon normally uptake K ions at a relatively high potential⁸¹, discouraging the construction of high-voltage PIBs when coupling with cathodes. This is reflected in low-cost biomass-derived hard carbon materials^{82, 83} whose large proportion of the capacity is gained generally at over 1 V. An in-depth understanding of the K ion uptake mechanism in the low-potential region and approaches to enhance the low-voltage capacity are therefore the keys to achieving high-performance hard carbon anodes for PIBs.

The situation significantly differs from the Na ion storage in hard carbon, which

shows an essential fraction of capacity associated with the pore-filling behavior of Na ions at a low voltage plateau of ~0.1 V vs. Na⁺/Na¹⁸ so is the attractive anode for SIBs. Most recently, Yang's group⁸⁴ reported the possible K ion pore-filling by comparing the Na and K ion storage using electron paramagnetic resonance (EPR). There is still a lack of any direct evidence, despite an open call for deep investigation^{85, 86}, to confirm whether a pore-filling mechanism occurs in PIBs, bringing difficulty to rational microstructure design.

Additionally, apart from the blurring storage mechanism, the unsatisfactory rate capability impedes the development of hard carbon anodes. In particular, a large discrepancy in the K ion transfer kinetics has been found. The distinct electrode preparation protocol including the binder type and amount of conductive additives is partly responsible. Except for it, the electrode/electrolyte interfaces also play critical roles⁸⁷. Furthermore, the extension of DME to hard carbon anode has not been very successful until now. One possible reason is the solvent co-intercalation, which decreases the capacity of hard carbon and may bring structural deterioration.

Herein, we synthesize porous and partially ordered HC from pistachio shucks biomass waste. It exhibits a charging capacity (K ion extraction) of around 220 mAh g⁻¹ under 1.0 V, outperforming most reported biomass waste-derived carbons. In addition to the K ion adsorption in the sloping region of the voltage profiles, an "intercalation-

pore filling" hybrid behavior of K ions in hard carbon is detected in the low-potential region. The universality of such behavior is confirmed in lignin-derived HC. We then shift from the linear ether to a cyclic counterpart, i.e., THF, to prevent solvent co-intercalation and boost the kinetics of hard carbon through interfacial chemistry regulation. To exclude the interference of the binder, we prepare a CNF film by electrospinning to serve as freestanding electrodes. Thanks to the rapid desolvation process and the stable SEI formation in THF-based electrolytes, the CNFs possess fast kinetics to retain great performance at high current rates and low temperatures.

3.2 Probing Potassium Storage Behavior

3.2.1 Synthesis and Physical Properties of Hard Carbon

As **Figure 3.1a** illustrates, the rinsed pistachio shucks were first ball-milled to fine powder and then sintered into uniform and dark ones. HCl treatment was applied after the calcination to remove impurities, as proved by X-ray diffraction (XRD) in **Figure 3.1b**. X-ray photoelectron spectroscopy (XPS) pattern (**Figure 3.1c**) further confirms the absence of impurity atoms other than oxygen, which is widely probed as surface functional groups and may contribute to K ion storage.

Raman results (**Figure 3.2a**) show a high intensity of D band at around 1341 cm⁻¹ because of the poor crystallinity and partially ordered domain under moderate carbonization temperatures of 1100-1400 °C, which agrees with the XRD broad peaks

at ~22° and 43° (**Figure 3.2b**) representing (002) and (100) diffraction. The sample treated at 1300 °C (denoted as HC-1300) delivers the highest capacity of 273 mAh g⁻¹ with retention of 96.7% (**Figure 3.2c-d**). Moreover, HC-1300 presents a superior rate performance compared to HC-1100 and HC-1400 (**Figure 3.2e-f**) and is selected for probing the charge storage mechanism. The defect from functional groups in HC-1100 and more graphitic layer in HC-1400 should be the reason for inferior peroformance.

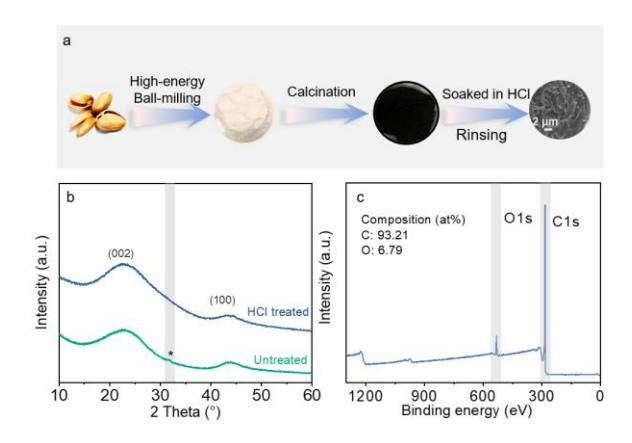


Figure 3.1. (a) Synthesis procedure of hard carbon (b) XRD Patterns of HC samples with or without HCl treatment. (c) Overall XPS result of HC-1300.

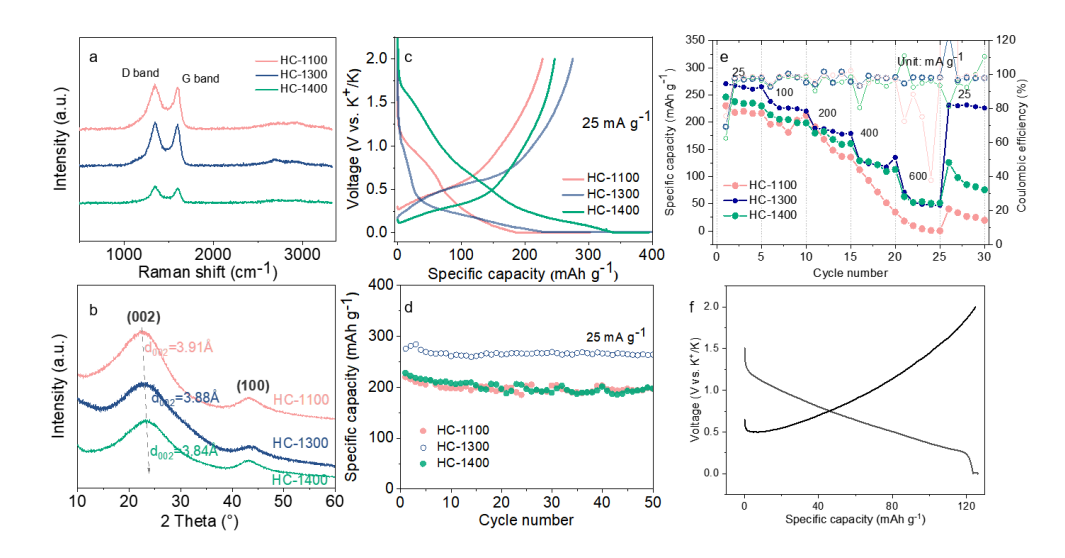


Figure 3.2. (a) Raman curves, (b) XRD patterns, (c) initial charging-discharging

profiles, (d) cycling performance, and (e) rate performance of HC-1100, HC-1300, and HC-1400 with corresponding (f) 26th voltage profile of HC-1400 in e.

The structural feature of HC-1300 is captured by cryo-electron transmission microscopy (cryo-TEM), which confirms the partially ordered structure exhibiting small graphitic domains and isolated graphene layers (**Figure 3.3a**). The small-angle X-ray scattering (SAXS) technique sensitive to both closed and open pores is employed for exploring the overall pore information. The data is fitted through the correlation between the characteristic length and the scattering power variation (**Figure 3.3b-c**)⁸⁸. The fitted results confirm the presence of micro- and mesopores in the sample (**Figure 3.3d-e**), leading to a large surface area S_{SAXS} of 229.0 m² g⁻¹.

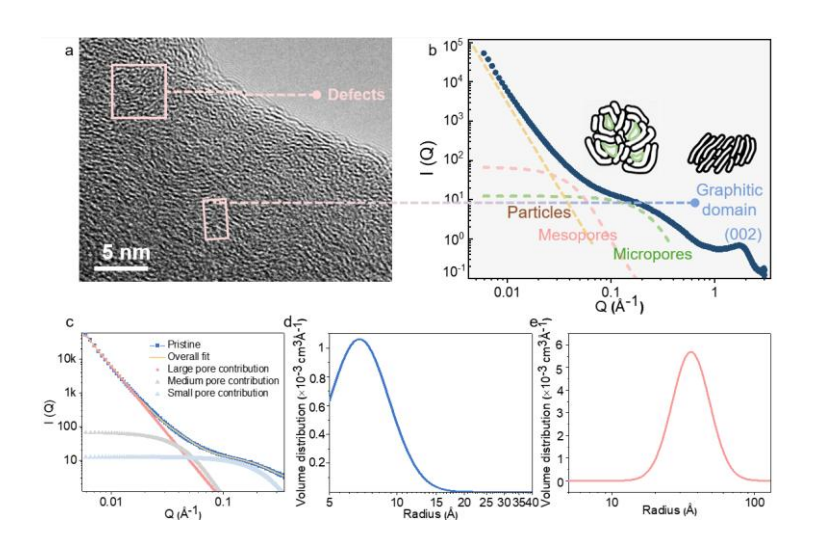


Figure 3.3. (a) HRTEM with marked defects (the left square), graphitic domain (rectangle in the middle). (b) SAXS patterns presenting pores and graphitic layers. (c) Fitted SAXS profiles of HC-1300. Volume distribution of (d) micropores and (e)

mesopores calculated through fitted SXAS results.

The pore distribution is further investigated by the N_2 adsorption/desorption (**Figure 3.4a**). It shows a Brunauer-Emmett-Teller (BET) surface area of 1.7 m² g⁻¹ and a pore volume of 0.004 cm³ g⁻¹. The pore size concentrates at 1.4 nm (micropores), 9.3 nm (mesopores), and over 50 nm (macropores), with an average pore size of 9.4 nm. Since N_2 adsorption has limitations in detecting the ultra-micropores, CO_2 adsorption is adopted as the supplementary. The CO_2 adsorption test result gives a much higher surface area of 70.9 m² g⁻¹ and a pore volume of 0.008 cm³ g⁻¹ (**Figure 3.4b**). It implies that apart from larger pores, a large content of micropores exists inside HC-1300, whose size is centered at 0.52-0.77 nm.

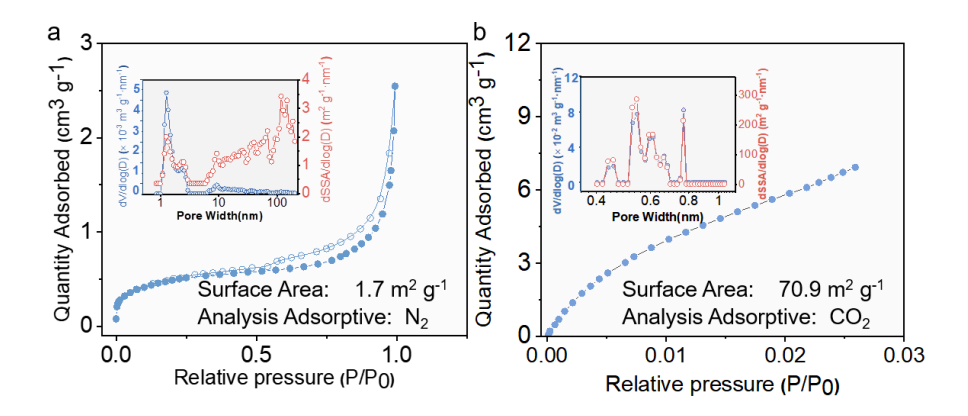


Figure 3.4. BET isotherms with porosity distribution derived from (a) N₂ and (b) CO₂ adsorption/desorption.

Note that the surface area obtained in N_2 and CO_2 adsorption/desorption is much smaller than that derived from SAXS. The reason lies in that the former two techniques mainly provide information on open pores⁸⁹. The results indicate that substantial

amounts of closed pores are presented in HC-1300. By subtracting S_{BET} from S_{SAXS} , the surface area contributed by the closed pore is as high as 158.1 m² g⁻¹. Furthermore, we examine the volume of closed pores through the true density measurement by the helium pycnometer since the He atom can reach nearly all pores in the samples. The true density of the sample ρ_{true} is 2.06 g cm⁻³. And the volume of closed pores is calculated to be 0.043 cm³ g⁻¹.

The rich porosity (as summarized in **Table 3.1**) provides a platform for exploring whether potassium nanocluster could be stored through the pore-filling mechanism.

Table 3.1. Pore size information of HC-1300.

Methods	S_{BET}	S_{SAXS}	S closed pores	V_{BET}	$V_{\text{closed pores}}$	True density
nous de la constant d	$(m^2 g^{-1})$	$(m^2 g^{-1})$	$(m^2 g^{-1})$	$(cm^3 g^{-1})$	$(cm^3 g^{-1})$	(g cm ⁻³)
N ₂ adsorption/desorption	1.7	_	_	0.004	_	_
CO ₂ adsorption/desorption	70.9	_	-	0.008	-	-
True density test	_	_	-	_	0.043	2.06
SAXS	_	229	158.1	_	_	_

3.2.2 Electrochemical Performance and Kinetics

We first compare the K ion storage with the Na counterpart, as the latter could be readily stored through pore-filling⁹⁰. The electrochemical performances are examined in classic carbonate electrolytes, and a constant-voltage discharge (CVDi) is applied after discharging to 5 mV to fully exhibit the capacity. The discharge curves of K (**Figure 3.5a**) and Na (**Figure 3.5b**) ion storage have a similar shape, both consisting of a

sloping region between 0.1-0.5 V followed by a plateau at a super low potential of below 0.1 V, as shown in the in dQ/dV profiles (insets in **Figure 3.5a-b**). It delivers a reversible capacity of 306 mAh g⁻¹ for Na ion storage with over 65% of it located in the plateau region. In comparison, the K counterpart shows a short low-voltage plateau, resulting in a lower reversible capacity of 273 mAh g⁻¹.

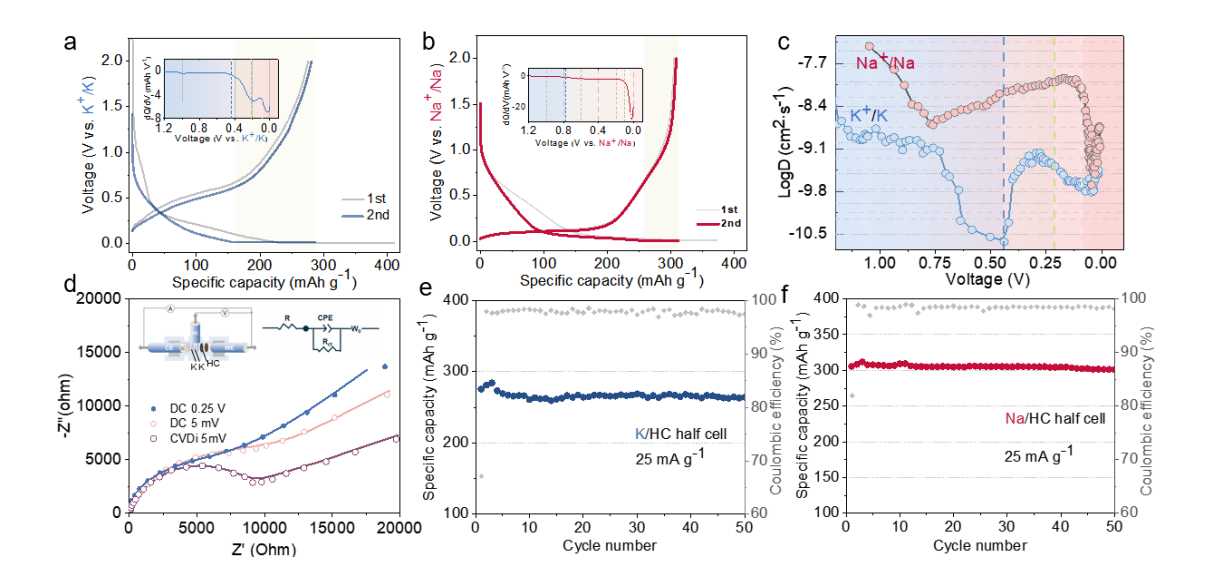


Figure 3.5. Initial two charging-discharging profiles with insets of dQ/dV profiles for (a) HC-1300/K cell and (b) HC-1300/Na cell. (c) Diffusion coefficient calculated from GITT results of HC-1300/K cell and HC-1300/Na cell. (d) EIS plots of HC-1300 obtained from three-electrode cells at different discharging states. The inset illustrates the three-electrode Swagelok cell. Cycling performances of (e) HC-1300/K cell and (f) HC-1300/Na cell.

Apart from the inferior capacity for K ions, a considerable proportion of capacity is gained during the CVDi process because of the poor kinetics. This is also reflected

by a large voltage hysteresis between the charge/discharge voltage profiles of K-ion cells. Therefore, we measure the apparent diffusion coefficient (D) by a Galvanostatic Intermittent Titration Technique (GITT) technique (Figure 3.5c). Both Na and K ion diffusivities show a similar trend but at a different pace. In specific, upon discharging, both the Na⁺ and K ion diffusivity decreases owing to the formation of SEI^{18,90}. Due to the distinct electrolyte decomposition pathway in the two systems, the Na⁺ diffusion pace goes through a progressive reduction above 0.8 V in contrast to 0.4 V for the K ion. Afterward, both diffusivity increases at the medium voltage region (0.8-0.1 for Na ion, and 0.45-0.1 V for K ion) because of the fast kinetics associated with Na ion or K ion adsorption⁹¹. The insertion-pore filling hybrid mechanism at the low voltage regime leads to a first decrease and then an increase in the diffusivity of both Na ion and K ion. Overall, the D value for K ion is in general one order of magnitude lower than that for Na, explaining the large voltage hysteresis. We therefore use electrochemical impedance spectroscopy (EIS) to compare the kinetics at the sloping and plateau regions. A three-electrode Swagelok cell, consisting of an HC-1300 working electrode, a K metal counter electrode, and a K metal reference electrode, is adopted to avoid the interference of the K metal counter electrode (illustrated in the inset of Figure 3.5d). The charge-transfer resistance (R_{ct}) of the sample ramps obviously from 6902 Ohm in the sloping region to over 10000 Ohm once discharging to 5 mV. Considering such sluggish kinetics in the low-voltage region, the CVDi process is required to fully access the K ion storage capability of HC-1300.

Table 3.2. Comparison of the electrochemical performance of biomass-derived HC precursors.

Ref.	Biomass	SSA ¹	Shape of	Potential	Operating	Initial	Capacity	Initial
	precursors	$(m^2 g^-)$	profile	window (V)	potential	capacity	below 1 V	Coulombic
92	Seafood waste	563	Slope	0-3.0	~1.5	250 at 25	82	65
	(chitin)					mA g ⁻¹		
82	Bacterial	778.75	Slope	0.01-2.8	~1.4	240 at 50	91	70
	cellulose					mA g ⁻¹		
93	Bamboo	336.4	Slope	0.01-3.0	1.275	339.3 at 50	85	55.72
	charcoal	330.4				$mA g^{-1}$		
94	Loofah	270	Slope	0.01-3.0	~1.5	150 at 100	95	43
		270				$mA g^{-1}$		
91	Cyanobacteria 437.	1373	Slope	0.01-3.0	~1.5	352 at 50	120	39.1
		437.3				$mA g^{-1}$		
95	Maple leaves	62.6	Slope +	0.01-3.0	~1.5	358.8 at 50	150	39
			Plateau			$mA g^{-1}$		
96	Skimmed cotton	n 612	Slope	0.01-2.0	~1.1	409.5 at	150	31.5
						100 mA g ⁻¹		
83	Oak	156	Slope +	0.01-2.3	~0.9	233.2 at 20	175	56.9
	Ouk	Ouk 150	Plateau	0.01 2.3	0.7	$mA g^{-1}$	175	30.7
97	Artemisia	1196	5 Slope	0.01-3.0	~1.5	116 at 70	100	24.7
	Hedinii	1170		0.01-3.0		$mA g^{-1}$		
98	Sugar cane 425	425.1	Slope +	0.01-2.5	~0.8	463 at 100	~200	64
		.25.1	Plateau			$mA g^{-1}$		0.
	This work	1.7	Slope +	0.005-2.0	~0.6	287 at 25	~220	67.1
	Pistachio shuck	1.,	Plateau	2.002 2.0	0.0	mA g ⁻¹		07.1

Despite the lower capacity and poor kinetics, the K ion storage possesses similar stability as the Na ion (**Figure 3.5e-f**), suggesting that the large K ion insertion does

_

 $[\]label{eq:collected} \begin{array}{c} 1 \\ \text{Collected through N_2 adsorption/desorption isotherm.} \end{array}$

not bring about significant structural damage to hard carbon upon cycling. The relatively low efficiencies may lie in the instability of electrolytes^{99, 100}, which require further optimization. It is worth mentioning that the K ion storage delivers a high charge capacity of 220 mAh g⁻¹ below 1.0 V with a relatively high initial Coulombic efficiency of 67.1%, which is one of the best among biomass-derived hard carbon anodes (**Table 3.2**).

3.2.3 K-ion Storage Behaviors

The alike electrochemical behavior between Na and K poses a question of whether they share analogous charge storage mechanisms. Thanks to the intensive studies on Na-ion batteries 101-104, the mechanisms associated with different voltage regimes in the voltage profiles have been clearly demonstrated. Depending on the microstructure of hard carbon, the sloping region may relate to Na ion storage through either adsorption on the isolated graphene layers or insertion between partially ordered graphitic domains 101, 105. The low voltage plateau capacity is widely accepted as the contribution of Na ions filling in the nanopores, i.e., the formation of quasi-Na metal clusters 106. Such a pore-filling behavior is one of the most stunning features of hard carbon, as it can not only uptake Na ion at a low voltage 107 but induce an exceptional capacity of up to 410 mAh g-1. It would be promising if the same mechanism could be applied to K ion storage, which will offer a potential approach to boost the capacity.

Raman tests were conducted on the samples at different states of potassiation/depotassiation (Figure 3.6a-b). Both the intensity D (I_D) and G (I_G) band of carbon decrease once discharged to 0.5 V because of the electrolyte decomposition to form SEI. Nevertheless, we detect neither apparent variation of the I_D/I_G nor shifting of D and G bands position until discharging to 0.25 V. It indicates that K ions storage within this region arises mainly from the surface adsorption on the isolated graphene sheets or defects, consistent with previous reports 108, 109. Subsequently, an obvious splitting peak at 1613 cm⁻¹ of G band emerges when discharged to 5 mV as an indicator of the stiffening of G-mode, which is caused by the disruption of Born-Oppenheimer expansion in the graphene layer and implies the formation of graphite intercalation compounds (GICs) with high stage number (stage II GIC KC24)110, 111. As the discharging proceeds to the CVDi stage, a significant downshift of the G band is discerned and the G band displays an asymmetrical Fanoy resonance shape. Such a phenomenon is typically observed in graphitic carbon anodes, like highly graphitized soft carbon, because of the existence of deeply intercalated GICs like stage I KC₈^{112, 113}. The intercalation of K ions and the electrons conveyed to graphitic layers cause the redshift for the G band, which can be ascribed to occupied π^* antibonding bands and weakened C-C bonds and the resonant phono scattering process ^{114, 115}.

To testify whether intercalation could take place in the partially ordered carbon

prepared here, we first conducted the ex-situ XRD test for the fully discharged sample, the peaks at 30.3° and 33.4° likely ascribed to K-GICs (KC₂₄ and KC₈)¹¹⁶ are detected (**Figure 3.7**), confirming the intercalation during CVDi process. Then we deliberately plate K metal on the HC-1300 electrode by discharging to blow 0 V. A spike is observed in the voltage profile (Figure 3.7a) before the K plating to overcome the nucleation energy, which is widely observed in the metal electrode. The absence of such a spike in the cell with the CVDi process also excludes the possibility of K metal plating in the CVDi process. The surface of the electrode after plating K is covered by K metal plots with a metallic shine. On the contrary, the electrode after CVDi remains black. XRD confirms the plated K metal (Figure 3.7b) after discharging an additional merely 30 mAh g⁻¹ capacity (based on the weight of HC-1300) below 0 V. The K ion intercalation shows poor kinetics, the reason why a clear shift of the G band only appears in the CVDi instead of the constant current discharge stage.

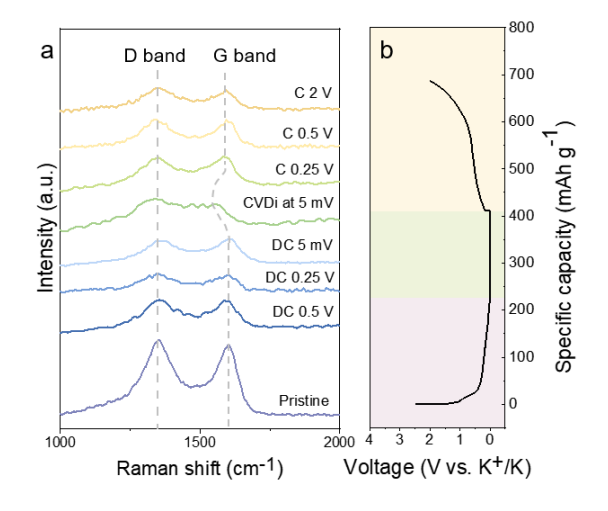


Figure 3.6. (a) Ex situ Raman curves of HC-1300/K collected at different charge-

discharge states with (b) the corresponding charging-discharging profile.

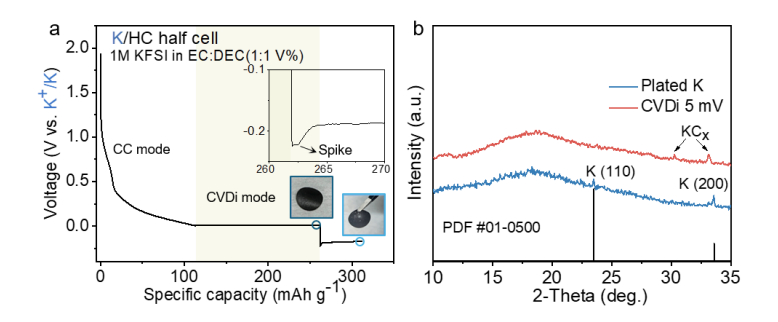


Figure 3.7. (a) Initial discharging profiles of HC-1300 in CC-CVDi mode followed by 2 h plating at 25 mA g⁻¹. (b) Ex situ XRD patterns for the sample after CVDi and the plated K sample.

When it comes to charging, the G band in Raman spectra witnesses a preliminary sudden blue shift at 0.25 V with improved intensity, attributed mainly to the extraction of potassium ions from the graphitic layers. The D and G band positions and their intensity ratio almost recover to the initial stage after charging to 2 V, evidencing the remarkable reversibility. Note that the presence of intercalation cannot exclude pore-filling in the low-voltage region. For instance, the weakening and broadening of the D band in the Raman spectrum after holding at 5 mV could also be associated with the filling of K ions into the nanopores because of the reduced sp² ring vibration 101, 117.

XPS was further utilized to detect K states upon charging/discharging. The plated K metal, as discussed before in **Figure 3.7**, is adopted as a reference to compare with the K ions storage in HC-1300. To avoid the interference of the SEI layer, the samples

are etched by Ar-beam with a depth of around 40 nm. There is not any clear change of the K 2p peak until discharging to 5 mV. In contrast, we observe the shift of the K 2p peak towards metallic K (**Figure 3.8a**) of the electrode after CVDi, which cannot be detected without Ar etching (**Figure 3.8b**). The K 2p position is recovered when charging to 0.25 V. This observation indicates the presence of another K form, other than the adsorbed/intercalated K ions and plated K metal, which is most likely to be quasi-metallic K nanoclusters filled in the nanopores according to the similar phenomenon in Na case^{118, 119}.

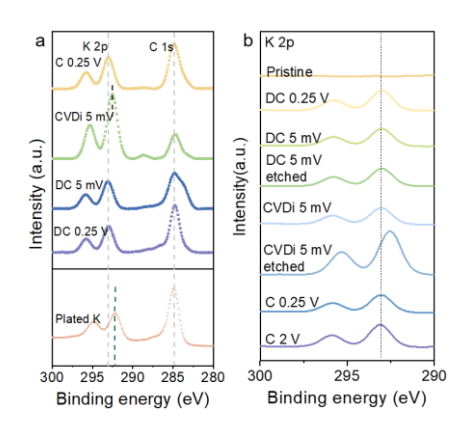


Figure 3.8. (a) Ex situ K 2p-C 1s spectra of samples at different charge-discharge states after Ar-beam etching (40 nm depth with rate of 0.25 nm s⁻¹) with plated K as the reference. (b) Ex situ K 2p peaks of samples at different states. Here DC and C represent the discharge and charge, respectively. All the spectra are normalized through C-C peak at 284.8 eV.

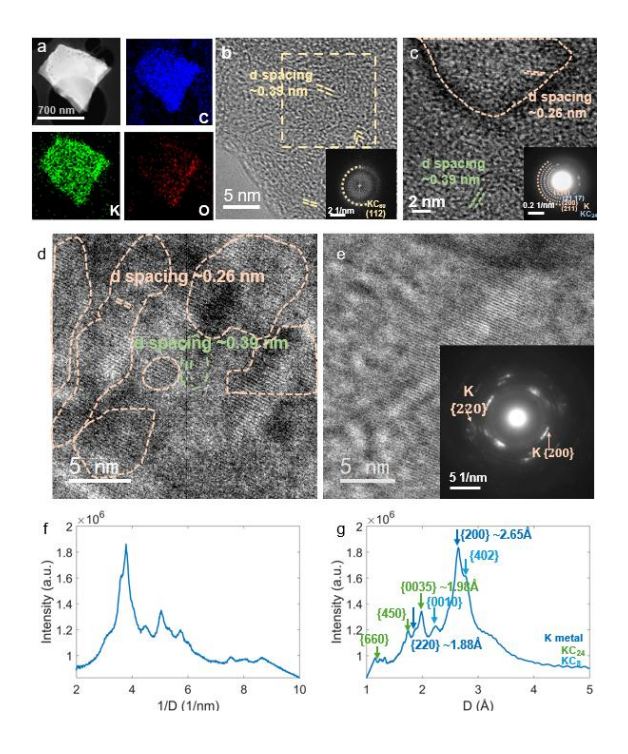


Figure 3.9. (a) Annular dark-field STEM image and the simultaneous EDS elemental maps for C, K, and O of CVDi-5 mV sample. Ex situ HR-TEM images of discharged HC-1300 at 5 mV (b) DC 5 mV sample, with the corresponding FFT pattern (inset), and (c-e) CVDi 5 mV (K deeper insertion) sample, with the corresponding SAED pattern presented in the inset. (f-g) Intensity plots derived from SAED image. All the TEM observation was taken at a cryogenic temperature of ~98 K to preserve the pristine state of the samples.

We adopted cryo-scanning transmission electron microscopy (cryo-STEM) to probe the detailed charge storage mechanism. The elemental mapping (**Figure 3.9a**) from energy-dispersive X-ray spectroscopy (EDS) shows the uniform distribution of K elements in samples. Compared to the pristine state in **Figure 3.3a**, the *d*-spacing of

{200} plane in the graphitic domain is slightly broadened after discharging to 5 mV, showing a value of 0.39 nm. (**Figure 3.9b**). This suggests the K-ion intercalation starts before 5 mV, which is confirmed in the corresponding fast Fourier transformation (FFT) pattern: apart from the {200} plane, the {112} plane of KC₆₀ (stage V GIC)¹²⁰ is observed. The CVDi at 5 mV allows the complete insertion of K ions under slow kinetics, leading to the deep intercalation of K ions into the graphitic domain. The {2117} plane of stage II GIC KC₂₄¹²⁰ (inset selected area electron diffraction (SAED) pattern in **Figure 3.9c**) and {0010} plane of stage I GIC KC₈ (**Figure 3.9f-g**) are detected after full discharge. It agrees well with the Raman spectra that show a clear G band shift at CVDi, which promotes the sufficient insertion of K ions with sluggish kinetics.

The upshift of the C π^* peak and the drop of π^* intensity after CVDi in electron energy loss spectroscopy (EELS) (**Figure 3.10a-b**) further supports the K ion intercalation. The C π^* peak corresponds to the excitations of electrons from 1s to the unoccupied anti-bonding π^* of carbon atoms¹²¹. Its intensity drop indicates the more occupied anti-bonding π^* by electrons from alkali ions^{122, 123}. Although detecting the K metal with EELS is challenging because of the lack of reliable potassium reference samples, clear K lattice with diffraction dots has been spotted in high-resolution TEM (HRTEM), which is most likely to be K nanoclusters filled in the nanopores and is

Na nanoclusters in hard carbon were captured by Kang's group before¹²⁴. The lattice spacing of 0.26 nm is well aligned with the {200} plane of the cubic K metal ($Im\overline{3}m$ (229) group) (**Figure 3.9c-e**). Furthermore, diffraction patterns corresponding to the {110}, {200}, and {211} planes of K metal are captured in the SAEDs (The insets in **Figure 3.9c** and **Figure 3.9e**). To the best of our knowledge, this is the first direct observation of quasi-metallic potassium storage in carbon-based electrodes.

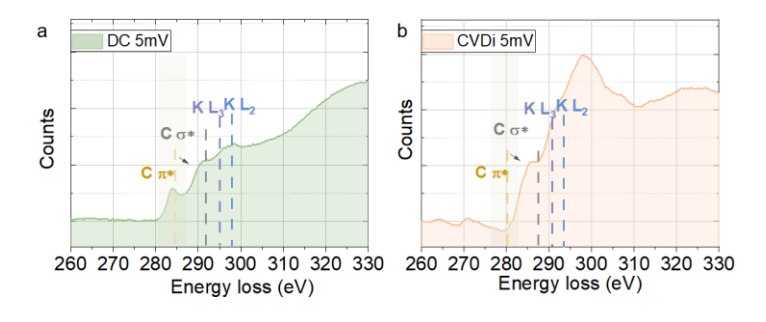


Figure 3.10. EELS of (a) the DC 5 mV sample and (b) the CVDi 5 mV sample.

Additionally, the signal of quasi-metallic K after CVDi (**Figure 3.11a**) is also detected through EPR, a powerful technique to capture the unpaired or delocalized electrons for alkali metal and transition metal elements¹²⁵. The pristine sample exhibits no pronounced signal but a tiny defect one originating from functional groups¹²⁶. As discharge proceeds, the broad peak ($\Delta B_{pp} \approx 5.1 \text{ mT}$) in Lorentz line shape (The absolute ratio of the maximum to the minimum of the intensity (A/B) is about unity) emerges, which represents more delocalized π -electrons of graphitic crystallites after K intercalation⁸⁴. This broad peak becomes more pronounced after the CVDi process as

shown in the inset of **Figure 3.11a**, which indicates the existence of GICs of low stage number in the CVDi stage due to the stronger interaction between the σ -spin of K ion with π -electrons in the graphitic molecule¹²⁷, consistent with the above-mentioned Raman and XRD results. Notably, a new sharp narrow peak ($\Delta B_{pp} \approx 0.8 \text{ mT}$) centered at a g-value of 2.00193 appears after discharge to 5 mV. It becomes strongly intense after CVDi due to the presence of delocalized electrons around the inserted K ions as a result of partial electron transfer from the hard carbon to the inserted K ions (from K⁺ to $K^{(1-x)+}$, 0 < x < 1, the form of quasi metallic K) in deep discharge 118, 128. Moreover, the symmetrical Lorentz shape (A=B) is obviously distinguished from the Dysonian asymmetrical shape (A>B) of the large bulk metal 129, which suggests the quasi-metallic K clusters are nanoscale not plated bulk ones¹³⁰. Based on the above discussion, apart from the adsorption in the sloping region, it can be interpreted that "intercalation-pore filling" hybrid behavior occurs in the low-voltage region, and the former starts first (Figure 3.11b).

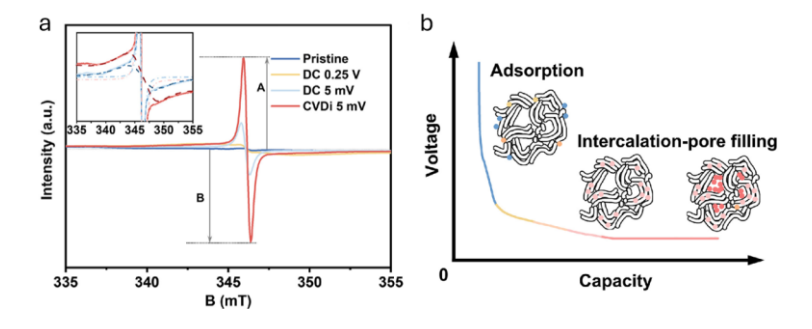


Figure 3.11. (a) EPR spectra of samples at different stages of cycling. (b) Schematic

illustration of proposed K ion storage behavior along with discharging.

3.2.4 Discussion

Having confirmed the presence of K ion pore filling in HC-1300, we next discuss whether such phenomenon exists in other hard carbon anodes and the approaches to promote the pore filling for gaining a high capacity at the low-voltage region.

i). Universality of K ion pore filling. To examine whether K ion filling in the nanopores occurs in other types of hard carbon, we prepared the lignin-derived one (Lig-HC) following the previous work¹³¹. Similar to the results on HC-1300 derived from pistachio, an over 50 mAh g⁻¹ capacity is delivered in the low-voltage plateau of Lig-HC (**Figure 3.12a**). A K 2p peak shift is found in XPS after the CVDi process, indicating the presence of K pore-filling behavior in hard carbon derived from different precursors.

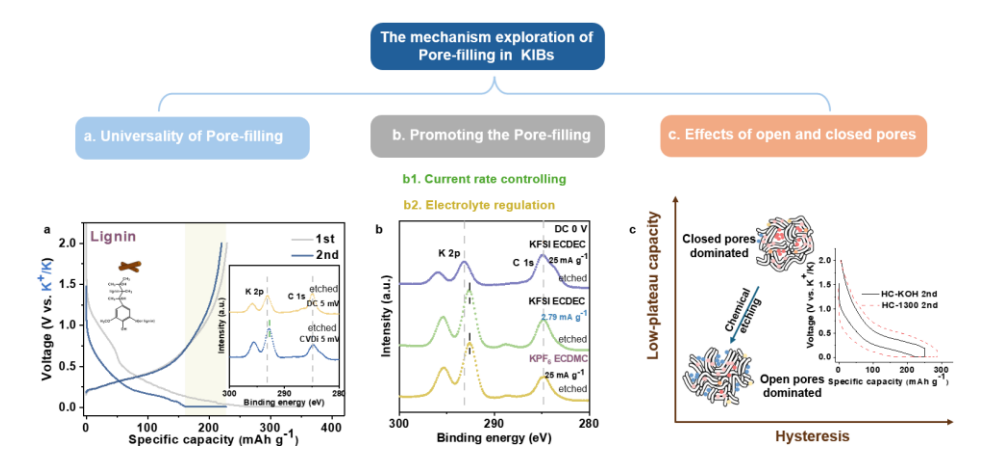


Figure 3.12. (a) The validity of pore-filling. (b) Strategies to avoid CVDi. (c) Effects of open and closed pores.

ii). Promoting the pore-filling behavior. The long duration of CVDi might restrict its practical utilization. We investigate whether CVDi is essential for such K storage behavior from two aspects. First, we directly discharge the HC-1300 at an extremely low current of 2.79 mA g⁻¹ (~1/100 C) to 0 V (**Figure 3.13a**). An obvious shift of the K 2p peak suggests that the pore filling of K ions could take place without CVDi (**Figure 3.12b**). Furthermore, the charge transfer kinetics is affected by the SEI, which is closely related to the electrolyte formulation³⁶. Our preliminary investigations show that 0.8 M KPF₆ in EC/DMC helps the construction of robust SEI favoring the K ions transfer. It allows the K ion pore filling at a relatively large constant current density of 25 mA g⁻¹ (voltage profiles are presented in **Figure 3.13b**). Therefore, the pore filling of K ions could be realized without resorting to the CVDi through further electrolyte engineering to circumvent the slow kinetics.

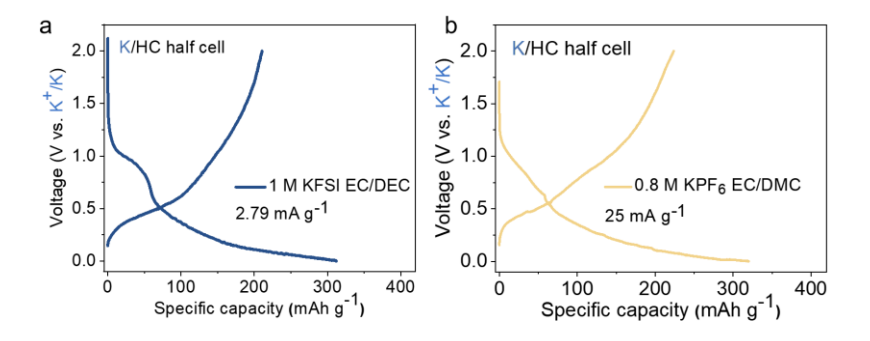


Figure 3.13. (a) The voltage profiles of HC-1300 cycled (a) at 2.79 mA g⁻¹ in 1M KFSI EC/DEC electrolyte and (b) at 25 mA g⁻¹ in 0.8 M KPF₆ EC/DMC electrolyte.

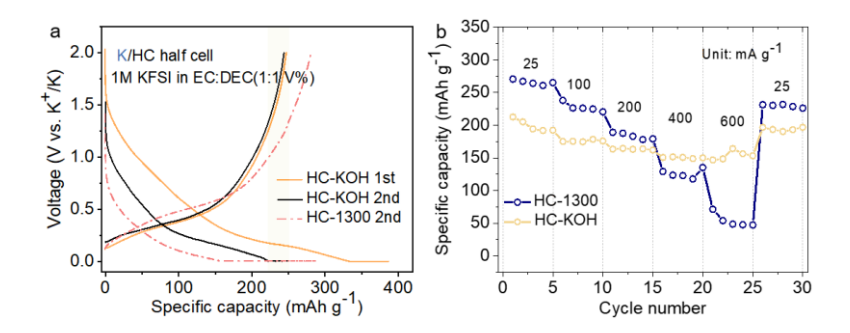


Figure 3.14. (a) The initial first two charging-discharging profiles of HC-KOH compared with HC-1300 2nd profile. (b) The rate performance of HC-1300 and HC-KOH (under the galvanostatic potentiostat discharging-galvanostatic charging mode).

iii). Effects of open and closed pores. After clarifying the validity of the porefilling mechanism, a question remains whether we could improve the K ion storage
capacity by increasing the porosity. We apply the classic chemical activation by KOH
to create additional pores as potential active sites, and the sample is denoted as HCKOH with an over ten times improved BET surface area of 22.3 m² g⁻¹. The HC-KOH
sample shows a much-reduced voltage hysteresis in the charge/discharge curves
(Figure 3.14). This does not come as a surprise as the high porosity could shorten the
solid diffusion path to ameliorate the kinetics, leading to small polarization and high
rate capability¹³². Nevertheless, the chemical activation fails to promote the K ion porefilling, as evidenced by the short low-voltage plateau. We speculate that only closed
pores could be utilized for hosting the K ions as the studies on Na ion pore-filling have

voltage plateau capacity^{61,89}. Additionally, we calculated the closed pore volume of the HC-KOH from the helium pycnometer-based true density test. It shows an increased true density of 2.16 g cm⁻³, indicating a decreased closed pore volume of 0.02 cm³ g⁻¹. It is over 50% reduced compared to the value (0.043 cm³ g⁻¹) for HC-1300. Such a dramatic decrease in closed pore volume might limit the pore-filling behavior (**Figure 3.12c**), thus calling for the preparation of hard carbon with rich closed pores to boost the capacity in future studies.

3.3 Interfacial Chemistry Regulation

3.3.1 Solvation Structures of Different Electrolytes

To search for potential electrolyte formulations in regulating the interfacial chemistry of hard carbons and promoting the rate performance, we first compare the physical-chemical properties, including the dielectric constant (ε), donor number (DN), dipole moment (μ), and viscosity of different solvents (**Table 3.3**). These parameters could reflect the solvating capability of the solvents to some extent, thus greatly affecting the desolvation and the charge transfer kinetics across the SEIs ^{133, 134}. The polar solvent EC, a main member of the carbonate family, exhibits an extremely high ε of 89.8 strongly coordinating with the K ion. Linear carbonate like DMC usually serves as a supplement for carbonate electrolytes to lower the viscosity of EC. A common electrolyte containing 1M KFSI in EC/DMC (1:1 vol.%) is used in this work as the

control electrolyte. Ethers usually exhibit lower solvating/desolvating energy than esters and support excellent cycling performance. We first focus on the most popular DME solvent, which has a linear structure, and then compare it with the less explored cyclic THF ether. These two ethers have similar ε and DN, but THF possesses a much higher μ/ε than DME (0.26 vs. 0.17), which endows THF with weak cation-solvent interaction according to the following relationship¹³⁵: $U_{ion-solvent} \propto [-\frac{n}{r^2}(\frac{\mu}{\varepsilon})]$. In this relationship, n is the charge of cation and r represents the distance between the ion and solvent molecule center. In addition, previous studies reveal that the oxygen atom is the most preferred site to coordinate with the cation (K ion) during solvation⁵³. THF only offers one O atom, compared to two in DME, for serving as the potential coordination sites based on the structural skeleton in **Table 3.3**⁵⁶. The above theoretical analysis indicates the THF may exhibit weak cation-solvent intercalation in the electrolytes.

Table 3.3. Physical and chemical properties of different solvents.

Solvent	Structure formula	Dielectric constant (ε)	Donor number	Dipole moment (μ)	μlε	Viscosity (cP)
THF	X.	7.58	20	1.97	0.26	0.55 (20 °C)
DME	8 3 2 2	7.2	20	1.22	0.17	1.1 (20 °C)
EC		89.8	16.4	4.49	0.05	2.1 (25 °C)
DMC	. A. A. A.	2.6	16	0.36	0.138	0.78 (30 °C)

The solvation structure of electrolytes directly affects the interfacial chemistry and

electrochemical performance. Raman spectra (Figure 3.15a-b) are adopted to investigate the solvation structure in different electrolytes, including 1M KFSI in THF, 1M KFSI in DME, and 1M KFSI in EC/DMC. Specifically, the Raman peak at 700-780 cm⁻¹ of different electrolytes results from FSI⁻ anions. For the EC/DMC system, after the addition of KFSI salt, the vibration band of free solvent at 899 cm⁻¹ undergoes a right shift, indicating the strong interaction of EC/DMC with K ions. The band centered at 722.1 cm⁻¹ becomes wider, signifying the abundant free FSI⁻ (723 cm⁻¹) without the appearance of CIP (732.8 cm⁻¹) and AGG (742.5 cm⁻¹). It further proves the strong solvation power of EC/DMC, as suggested in previous studies¹³⁶. Additionally, a relatively strong solvation of solvent with K ion can also be found in the DME system: a new vibration band arises at 860 cm⁻¹, which corresponds to the coordinated K ion -DME¹³³. However, the FSI⁻ signal is more complex than that of the EC/DMC system, which will be discussed later. In contrast, for the THF system, the vibration bands at 916 cm⁻¹ of pure THF and KFSI-contained THF-based electrolytes are almost coincident, which suggests the weak interaction between K ion and THF solvent.

To further clarify the complex FSI⁻ signals in the DME system and THF system, the enlarged peaks of the S-N-S signal of the FSI⁻ anion have been fitted (**Figure 3.15b**). In the DME solvation structure, free FSI⁻ accounts for 47.7% with the low content of CIP (21.2%) and AGG (31.1%) contribution. On the contrary, the solvation structure in

the THF electrolyte is dominated by CIP (52.8%) and AGG (33.8%), with only 13.4% of free FSI⁻. As depicted in the right part of **Figure 3.15c**, the CIP and AGG dominant solvation structure in the THF system implies the stronger coordination power of K ion and anion FSI⁻, and the lower solvation power of THF solvent. The lower solvation/desolvation power of THF is likely to induce the anion-derived SEI and boost the kinetics¹³⁷.

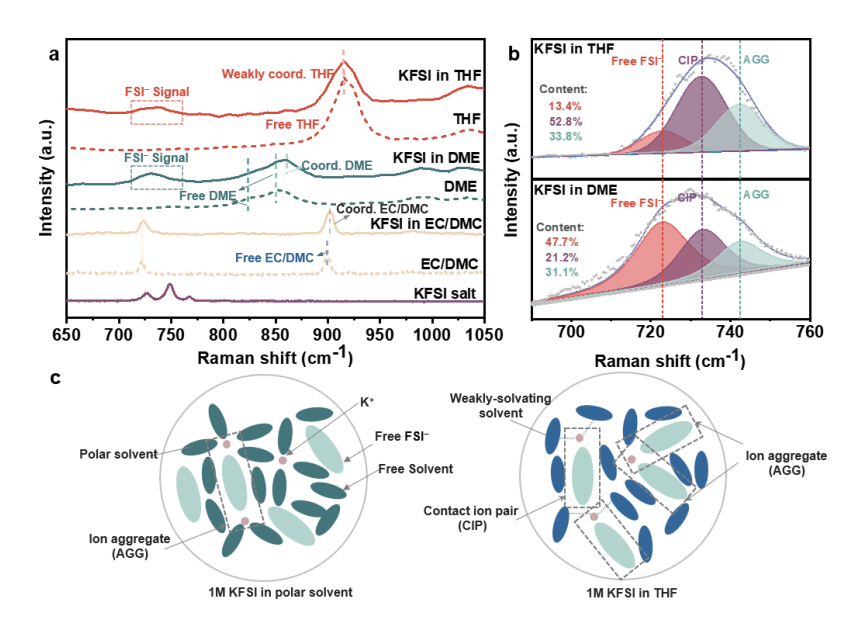


Figure 3.15. (a) Raman spectra of electrolytes, pure solvents, and KFSI salt. (b) Enlarged FSI⁻ peaks of 1M KFSI in THF and 1M KFSI in DME. (c) Schematic illustration of the solvating structure of 1M KFSI in DME and 1M KFSI in THF.

3.3.2 Different Kinetics Behaviors

To reveal the influence of solvation structure on interfacial chemistry and electrochemical performance of anodes, the freestanding CNF electrodes are adopted as the model system. A naturally abundant lignin polymer was used as the precursor to

produce CNFs. Because of the poor spinnability of pure lignin, a blended lignin/PAN was electrospun and thermal annealed to produce CNF film, as illustrated in Figure **3.16a**. The morphology of CNF is captured through SEM (Figure 3.16b) and TEM (Figure 3.16c), showing a bead-free structure with a diameter ranging from 221 to 566 nm. There is an absence of clear graphitic structure in the CNFs due to the low carbonization temperature. This is confirmed by the XRD result (Figure 3.16d), which exhibits a board (002) peak indicating poor crystallinity with a large d-spacing of 3.85 Å (vs. 3.38 Å for graphite). The CNFs show a surface area of 122.1 m² g⁻¹ and a pore volume of 0.03 m³ g⁻¹. A high carbon content of 96.8% is observed in the CNFs, as indicated by the XPS in Figure 3.17a. The high-purity carbon largely precludes the K ion storage through functional groups, which usually takes place at a high potential of over 1 V (vs. K^+/K). The prominent D-band in the Raman spectrum (**Figure 3.17b**) also suggests that a temperature of 1350 °C is insufficient to promote graphitization. Nevertheless, a sharp (101) diffraction peak is observed, indicating the presence of tiny graphitic domains.

The electrochemical performance of CNFs in different electrolytes is compared. Surprisingly, it delivers a super-low reversible capacity of 67 mAh g⁻¹ in 1M KFSI in DME electrolyte (**Figure 3.18a**). A detailed examination of the voltage profiles by the dQ (capacity)/dV(voltage) curve suggests the presence of solvent co-intercalation

during K ion insertion, as evidenced by the characteristic peak at $\sim 1.16~\rm V^{53}$. It suggests that the co-intercalation could occur in not only the perfectly ordered graphite anode but also in the hard carbon with tiny graphitic domains. Although it likely does not affect the stability of graphite, the solvent co-intercalation significantly decreases the cyclic life of the CNFs anode. Thanks to the weak K-solvent interaction in the THF electrolyte, there is not any trace of co-intercalation from the voltage profiles (**Figure 3.18b**).

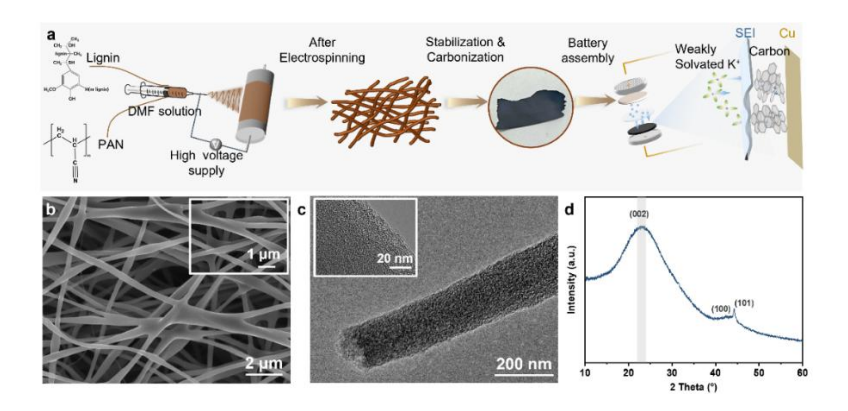


Figure 3.16. (a) Fabrication scheme of CNFs for PIBs. (b) SEM and (c) HRTEM images of CNFs. (d) XRD pattern of CNF.

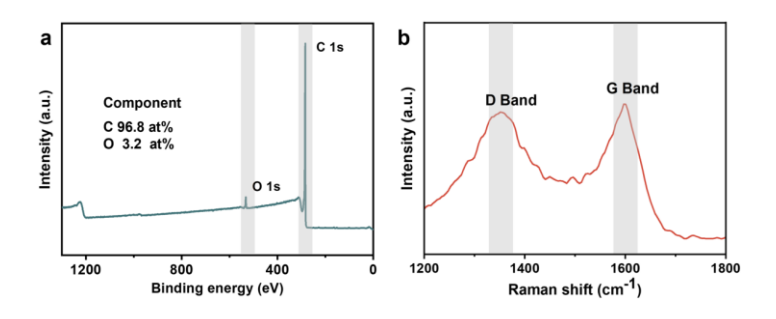


Figure 3.17. (a) XPS results and (b) Raman pattern of as-prepared CNFs.

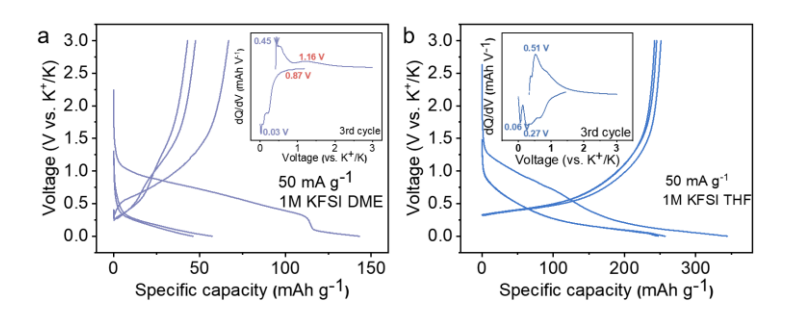


Figure 3.18. Charge-discharge profiles of CNFs in different electrolytes with inset of dQ/dV curve (a) 1M KFSI in DME electrolyte. (b) 1M KFSI in THF electrolyte.

It shows a high capacity of 245 mAh g⁻¹ in 1M KFSI in THF at 50 mA g⁻¹, which also outperforms the 158 mAh g⁻¹ in 1M KFSI in EC/DMC (**Figure 3.19a**). Note that despite the even stronger solvation in EC/DMC than in DME, the solvent cointercalation rarely takes place in carbonate electrolytes except propylene carbonate ¹³⁸. Therefore, we focus on the EC/DMC and THF electrolytes in the following part to probe the effect of interfacial chemistry.

The CNFs deliver an attractive rate performance in 1M KFSI in THF, with a capacity of 245, 205, 186, 175, 157, and 143 mAh g⁻¹ at 50, 100, 250, 500, 1000, and 1500 mA g⁻¹, respectively (**Figure 3.19b**). Here 1500 mA g⁻¹ corresponds to \sim 5.4 C based on the theoretical capacity of KC₈ formation (279 mAh g⁻¹). The capacity could fully recover after the current density returns to 50 mA g⁻¹. This performance is superior to most previously reported works (**Table 3.4**), especially those with essential K ion insertion with a practicable average potential of < 1 V vs. K⁺/K. In contrast, the CNFs undergo a fast capacity decrease with the increase in the current density in the

electrolyte of 1M KFSI in EC/DMC. A merely 63 mAh g⁻¹ of capacity remains at 1000 mA g⁻¹, which further reduces to 31 mAh g⁻¹ at 1500 mAh g⁻¹. We note that the different carbonate solvents could also affect the rate capability. A 1M KFSI in EC/ Ethyl methyl carbonate (EMC) electrolyte is assessed considering the beneficial effect of EMC in graphite anode. Although a high initial capacity of 266 mAh g⁻¹ is achieved in 1M KFSI in EC/EMC at 50 mA g⁻¹ for CNF, it sharply declines by over 50% (< 130 mAh g⁻¹) at the current density of 250 mA g⁻¹, which is even poorer than that in 1M KFSI in EC/DMC. Additionally, to examine whether a similar phenomenon occurs in classical electrodes, a pure lignin powder-based electrode with a much smaller surface area (12.3 m² g⁻¹ vs. 122.1 m² g⁻¹ for CNFs) is measured as well (**Figure 3.19c**). LigP delivers an initial capacity of 215 mAh $g^{\text{-1}}$ at 50 mA $g^{\text{-1}}$ in THF electrolyte and maintains over half (119 mAh g⁻¹) when the current density comes to 250 mA g⁻¹. However, the capacity of LigP sharply decreases from 131 mAh g⁻¹ at 50 mA g⁻¹ to below 50 mAh g⁻¹ at 250 mA g⁻¹ in the EC/DMC system. It confirms the advantage of THF electrolytes in achieving high-rate carbon anodes although the capacity is unsatisfactory in comparison with CNFs. Such an enhancement in the rate capability does not sacrifice stability. The CNF exhibits a stable specific capacity of 232 mAh g⁻¹ with a retention of 97% after 50 cycles at 100 mA g⁻¹ (Figure 3.19d).

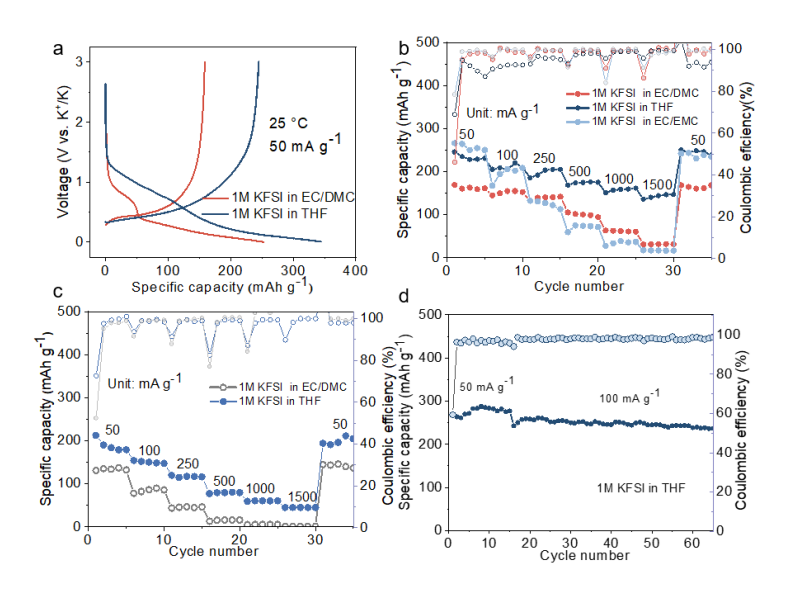


Figure 3.19. (a) Initial charge/discharge profiles of CNFs. (b) Rate behaviors of CNFs at 25 °C in 1M KFSI in EC/DMC, 1M KFSI in THF, and 1M KFSI in EC/EMC electrolytes. (c) Rate performances of Lignin powder in different electrolytes. (d) Cyclic performance of CNFs in 1M KFSI in THF at 100 mA g⁻¹ at 25 °C.

Table 3.4. Comparison of the electrochemical performance of PIB hard carbon anodes.

Ref.	Potential window (V)	Operating potential at charging capacity half (V)	Initial capacity (mAh g ⁻¹)	Capacity below 1 V (mAh g ⁻¹)	Capacity retention under the high rate*	Initial Coulombic efficiency (%)
92	0-3.0	~1.5	250 at 25 mA g ⁻¹	82	64% at 7.1C	65
82	0.01-2.8	~1.4	240 at 50 mA g ⁻¹	91	59% at 3.6C	70
93	0.01-3.0	1.275	339.3 at 50 mA g ⁻¹	85	32.4 at 3.6C	55.72
94	0.01-3.0	~1.5	150 at 100 mA g ⁻¹	95	66% at 1.8C	43
91	0.01-3.0	~1.5	352 at 50 mA g ⁻¹	120	44% at 3.6C	39.1
139	0.01-1.5	~0.4	262 at 27.9 mA g ⁻¹	~210	52% at 5C	61
83	0.01-2.3	~0.9	233.2 at 20 mA g ⁻¹	175	17% at 1.8C	56.9
97	0.01-3.0	~1.5	116 at 70 mA g ⁻¹	100	67% at 1.43C	24.7
98	0.01-2.5	~1.0	463 at 100 mA g ⁻¹	~200	39.3% at 7.1C	64

140	0-3.0	~0.8	320 at 50 mA g ⁻¹	~190	46% at 3.6C	43.2
This	0-3.0	0.7	245 at 50	200	64% at 3.6C	68.9
work	0-3.0	~0.7	mA g ⁻¹	~200	58.4% at 5.4C	08.9

^{*:} $1C=279 \text{ mAh g}^{-1}$.

Pushing to the limit, we examine the performance at a low temperature of 0 °C (Figure 3.20a). The electrode delivers a competitive capacity of 200 mAh g⁻¹ at 50 mA g-1 in 1M KFSI in THF systems, showing superiority in both capacity and stability compared to the one in carbonate electrolytes. GITT tests are applied for CNF electrodes in the two electrolytes to compare the charge transfer kinetics. The diffusivity evolutions with respect to the charging/discharging potential are presented in Figure 3.20b-c. Upon discharging, the K-ion diffusion coefficient declines gradually in the EC/DMC electrolyte. Compared with the EC/DMC system, the higher coefficient in the THF electrolyte between 1.0-0.5 V (during the SEI formation period) indicates a smoother SEI formation in the THF electrolyte. Nevertheless, there is almost no difference between coefficients in the low-voltage region, likely suggesting that the insertion mechanism is not affected by the disparity in the two electrolytes. The coefficient of K ion in THF electrolyte is generally half an order of magnitude larger than that in carbonate in the following charging process.

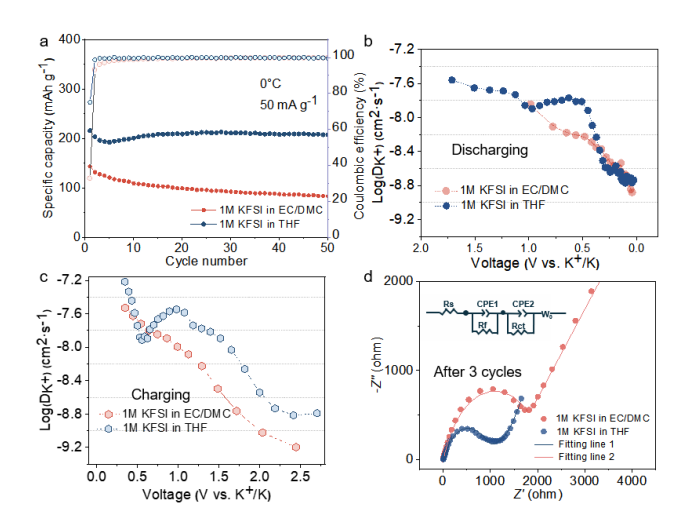


Figure 3.20. (a) Cyclic performances of CNFs at 0 °C. K ion apparent diffusion coefficient calculated from GITT results of CNF upon (b) discharging and (c) charging. (d) EIS plots of 3rd-cycled CNF electrode in different electrolytes at 100 mA g⁻¹.

Additionally, although the original impedance of CNF is over 2000 Ohm for both electrolytes, a drastic decrease of 50% in the impedance of the CNF electrode is found in 1M KFSI in THF after 3 cycles at 100 mA g⁻¹. In contrast, the impedance R_{ct} remains great (1985 Ohm) for CNF in the EC/DMC system after 3 cycles (**Figure 3.20d**). Therefore, a significant boost in kinetic is achieved by changing the EC/DMC electrolyte into the THF electrolyte, which is aligned with the above theoretical analysis.

3.3.3 Charge Storage Mechanisms and Interfacial Chemistry

The reaction kinetics could be affected by both the charge storage mechanism and interface properties. The in-situ Raman is first conducted to distinguish whether the different electrolytes change the K ion insertion behavior. Once discharged in the THF electrolyte (**Figure 3.21a**), the G band at 1598 cm⁻¹ of CNF begins to redshift and

becomes wider arising from the new splitting peak G_c corresponding to the graphite intercalation compounds (GICs). That results from the intercalation of K ion and electrons conveyed to graphic layers 101, 114, 115. The gradual blue shift of the G band implies the leaving of K ion from the graphitic layer during the charging process, which is the typical change for graphitic anodes¹¹³. These results confirm the neat K ion insertion in THF-electrolyte, in contrast to the solvent co-intercalation in the DME. In the EC/DMC system (Figure 3.21b), the almost identical evolution of the G band for the CNF electrode is found, with the tendency of gradual red shift of the G-band upon discharging and continuous blue shift upon charging. A similar pace of K ion insertion exists in the two electrolyte systems. Therefore, the better kinetics in the THF electrolyte arise mainly from the fast interfacial process, involving the de-solvation of K ion and the followed diffusion across the SEI. As the former Raman analysis of electrolytes demonstrated, the weak K-THF interaction benefits the de-solvation process.

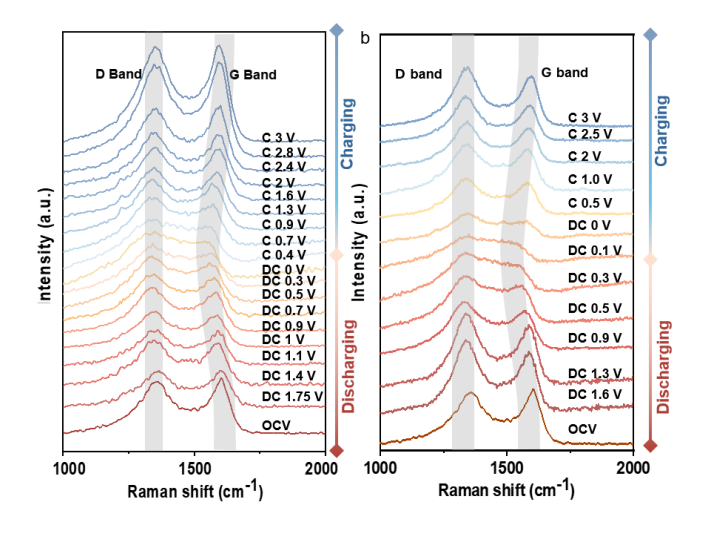


Figure 3.21. In-situ Raman plots of CNF electrode using the electrolyte of (a) 1M KFSI in THF and (b) 1M KFSI in EC/DMC.

We further examine the SEIs formed on CNFs in different electrolytes by HRTEM (Figure 3.22a). For CNFs cycled in 1M KFSI in THF, a thin and uniform SEI with a thickness of 4.5 nm is covered on the nanofiber. Turning to the SEI formed in 1M KFSI in EC/DMC (Figure 3.22b), it exhibits uneven thickness ranging from 2 to 8.3 nm. In particular, tiny inorganic crystals like K₂SO₄ and K₂O, as identified from the Fast Fourier Transformation (FFT) patterns, are embedded in the SEIs formed in EC/DMC electrolytes. In comparison, there is the absence of crystal phases in the SEIs under THF electrolytes, possibly due to the thin SEIs that restrict the crystallization and growth of inorganic species¹⁴¹. The thick and uneven SEI in the carbonate electrolyte would increase the impedance and deteriorate the K ion transport kinetics^{142, 143}, explaining the inferior K ion diffusivity in EC/DMC-based electrolyte despite the same K ion insertion process.

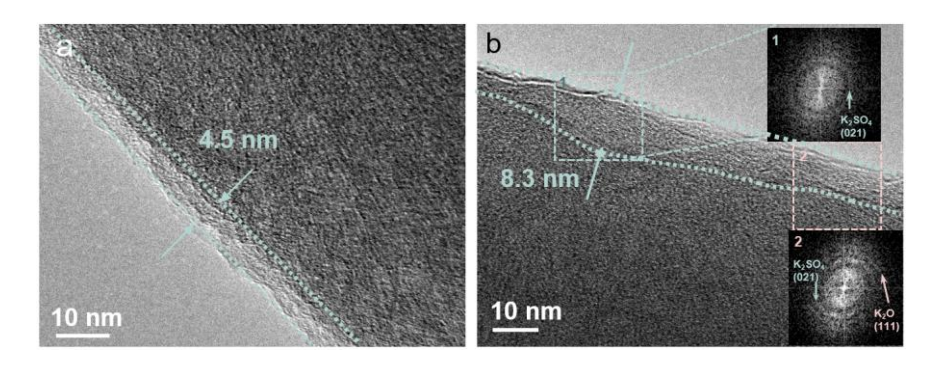


Figure 3.22. TEM images of third-cycled CNFs in (a) 1M KFSI/THF and (b) 1M KFSI/

ECDMC with corresponding FFT patterns in the marked area at 50 mA g⁻¹.

The dramatic difference in the SEI morphology and the resulting electrochemical performance inspires us to get further insight into their chemical compositions. XPS spectra of C 1s, K 2p, O 1s, and F 1s are collected. A significant amount of organic species are observed, signified by the C-O (285.9 eV), C=O (286.6 eV) in C 1s spectra, C-O (532.14 eV), and C=O (531.1 eV) in O 1s (Figure 3.23a-b). Parallelly, the K-O (292.8, 295.4 eV), K-F (293.7, 296.3 eV), CO₃²⁻ (288.2 eV) in K 2p spectra, with the K-F (683.6, 685.3 eV) and S-F (686.9, 688.2 eV) in F 1s spectra (**Figure 3.23c**) reflect the inorganic components. In general, both the SEIs formed in ether and ester-based electrolytes have a composite structure with the inorganic species distributed in the organic matrix. The SEIs in THF electrolyte have a higher overall content of the inorganic components, as suggested by the lower carbon content of 72.8at.% compared to 77.7at.% for the one in the EC/DMC counterpart (Figure 3.23d). The reason lies in the strong solvation of EC/DMC as discussed before, leading to the more severe decomposition of the solvent that mainly contributes to the organic species. Additionally, the stronger peak of CO₃²⁻ implies more solvent decomposition in the EC/DMC system. In comparison, more FSI are coordinated with the K ion in THF electrolytes¹⁴⁴, resulting in the significant anion decomposition to form the inorganic components, which can be reflected by the higher F content.

The K-F and S-F peaks for the THF system are more distinct than those in the EC/DMC system, implying a higher proportion of K-F and S-F coordination and more inorganic components (like KF) from the FSI decomposition in the SEI under THF electrolyte. Moreover, the SEI in the THF system possesses 2.5at.% F, which is twice larger than that of the EC/DMC counterpart (1.1at.%) shown in Figure 3.23d. Under the pre-condition that both solvents (THF and EC/DMC) contain no F element, the fluorine-rich SEIs in THF electrolyte are mainly from the decomposition of FSI. The rich F species could potentially benefit from the charge transfer, as widely observed in the LiF counterpart 145, 146. Furthermore, in TEM figures, the inorganic components are almost amorphous for the SEI in the THF electrolyte, whereas crystallized particles are observed for the ones in EC/DMC electrolytes. Compared to the crystalline phase, the amorphous one is preferable for boosting ionic conductivity^{147, 148}. In short, the thin and homogeneous SEIs in THF electrolytes significantly contribute to the superior rate performance.

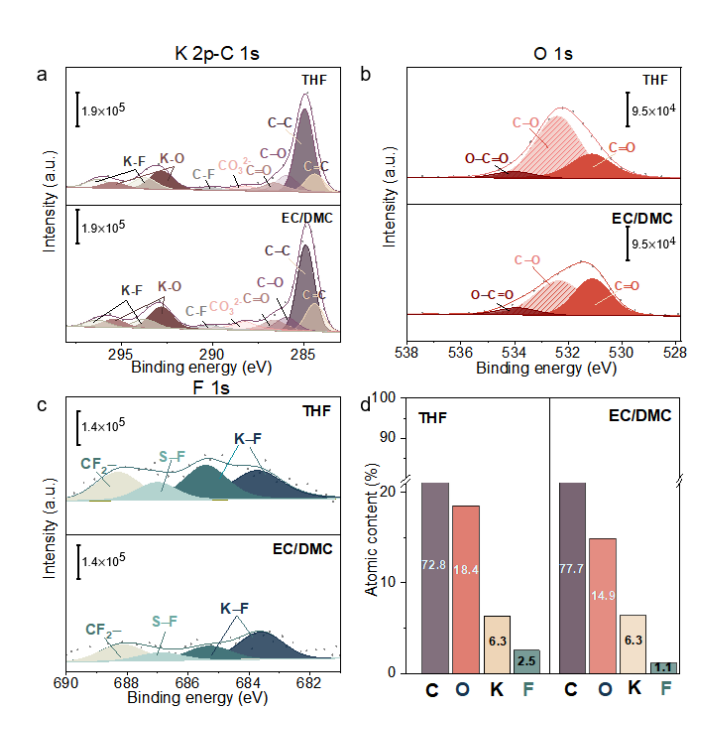


Figure 3.23. The surficial composition analyzed by XPS. (a) K 2p-C 1s, (b) O 1s, and (c) F 1s spectra of CNFs after 3 cycles at 50 mA g⁻¹ using electrolyte of 1M KFSI in THF or 1M KFSI in EC/DMC; (d) The atomic fractions of pristine CNFs cycled in 1M KFSI in THF or 1M KFSI in EC/DMC.

3.4 Summary

We first prepare a hard carbon material from pistachio shell waste for exploring the K ion storage performance and the associated charge storage mechanism. It is found that the K ion insertion exhibits much lower kinetics than the Na ion, requiring a CVDi at the end of discharge to allow the full K ion insertion. The as-prepared anode delivers a decent charging capacity of over 200 mAh g⁻¹ at below 1 V, making biomaterials-derived hard carbons attractive candidates for low-cost PIBs. Assisted by the cryo-TEM and EPR, we clearly observe the quasi-potassium nanoclusters after fully discharging,

evidencing that the K ion filling could also occur in the hard carbon. Such behavior could be promoted by optimizing cycling protocol and electrolyte engineering to circumvent poor kinetics. We also show that the open pores created through classic chemical etching do not enhance the pore-filling capacity but only boost the kinetics. It indicates the design of appropriate closed pores is the key to achieving high-capacity hard carbon in future studies.

Noting the unsatisfactory rate performance, we prepare a CNF film by electrospinning lignin and PAN, which serves as a freestanding electrode to probe the effect of interfacial chemistry on the kinetics of hard carbon anodes. We examine the physical and chemical properties of different solvents to screen the potential electrolytes for regulating the K ion solvation structure. The THF with the weak Ksolvent interaction is selected because of low polarity and high μ/ε , as confirmed by the Raman analysis. Such low solvation brings about several advantages. Firstly, it inhibits the solvent co-intercalation that occurs in the most widely investigated DME electrolyte, which deteriorates the electrode stability. Secondly, the facile de-solvation process would enhance the K ion insertion. Most importantly, a considerable amount of FSIenters the solvation sheath, leading to an inorganic-rich SEI that benefits the charge transfer. HRTEM images indicate the SEI formed in the THF electrolyte is more uniform and thinner than the one in the EC/DMC counterpart, further boosting the

stability and kinetics across the SEI. Consequently, the CNFs show superior rate capability (143 mAh $\rm g^{-1}$ at 1.5 A $\rm g^{-1}$) and cyclic performance in the THF-based electrolyte even at 0 °C. These results suggest that the hard carbon anodes could sustain the high rate PIBs with the rational electrolyte design, where cyclic ether may offer unique merits.

Chapter 4. Tailoring Solid Electrolyte Interphase by Carbonaceous Materials for Advanced Potassium Metal Anodes

Besides the role of anodes discussed in the previous chapter, carbonaceous materials are widely used as decoration materials of current collectors or hosts for potassium metal anodes, which possess greater capacity and are promising to achieve high energy density. However, the performance of the K metal anode is still unsatisfactory. This chapter introduced a modified current collector with a lower Fermi level and potassiophilic species to induce an inorganic-rich SEI and promote nucleation of K, finally achieving a 4.4 V anode-free potassium metal batteries (PMB).

4.1 Introduction

The poor cyclic stability and the inferior reversibility hinder the practical application of PMBs, mostly attributed to unstable solid electrolyte interphase (SEI)⁹⁹ and uncontrollable potassium dendrite growth¹⁴⁹. A variety of modifications have been put forward to strengthen the stability of SEI through modulating the composition of SEI, including electrolyte design³⁶⁻³⁸ and employment of artificial protecting coatings³¹⁻³³. However, little attention is paid to the origin of SEI generation, which hinders the design of the anode and current collector to build PMBs with little or no anode excess. The electrolyte remains thermodynamically stable within its electrochemical window

and will undergo reduction or oxidization to form a passivating interphase beyond this potential range 150 . Upon the K plating period, the electric potential of the anode will decrease, accompanied by an increase in the Fermi level (E_f) of the anode $^{151-153}$. Once the E_f of the anode surpasses the energy level associated with the reduction potential of the electrolyte (E_r), electrons will flow from E_f to E_r due to the positive energy gap, resulting in the decomposition of anions and solvents. Reducing the E_f of the anode is expected to narrow such a gap, thereby suppressing the severe electrolyte decomposition. In an anode-free cell, the current collector serves as the anode at the beginning of discharge, thus playing a critical role in SEI formation. This is well illustrated in previous works where the current collector with a lower Fermi level effectively inhibits copious electrolyte reduction

Apart from the nanostructure of SEI, the K metal deposition morphology could also affect its stability. Various effective strategies^{34,35,39} are put forward to control the nucleation behavior and enhance the cyclic stability, in particular, tuning the surface functionality of the current collector by carbonaceous for the promising mass production as mentioned before^{40, 41}. In contrast to building 3D skeletons with larger surface areas^{29, 30}, a thin carbon-based coating layer on the current collector reduces the risk of side reactions, thereby enhancing the Coulombic efficiency (CE)¹⁵⁴. Nevertheless, the performance is still unsatisfactory but normally requires high-

concentration electrolytes.

Here we design a decorated Al current collector by directly spraying carbon nanofibers grown with nickel species (CNFNi@Al). Benefitting from the difference in work functions between Al and CNFNi, the CNFNi@Al induces an anion-derived thin SEI structure. Additionally, potassiophilic nickel species promote the smooth lateral plating behavior of K metal to prevent dendrite formation. Stemming from these synergy effects, the CNFNi endows the asymmetric cell with an average CE of 99.2% and a duration of over 1500 h in a 1M electrolyte. Even under a harsh anode-free condition with the high-voltage cathode MnHCF, it guarantees the operation of 50 cycles with a specific energy density of 381 Wh kg⁻¹ (based on the MnHCF and CNFNi mass) without anode precycling.

4.2 Results and Discussion

4.2.1 Properties of CNFNi@Al

The synthesis procedure of CNFNi@Al current collector involves electrospinning of CNF, the chemical growth of nickel species on CNF to produce CNFNi, and uniformly spray painting the Al foil with CNFNi dispersion (**Figure 4.1**). The nickel species of Ni₃N, NiO, and metallic Ni particles with sizes of around 20 nm were generated on CNF with a diameter of 200 nm, as shown in TEM images (**Figure 4.2a-b**). These can

be confirmed by the SAED pattern (**Figure 4.2c-d**). Multiple pairs of diffraction spots emerge on the pattern of CNFNi samples that can be indexed as the Ni, NiO, Ni₃N, and Ni₃C species.

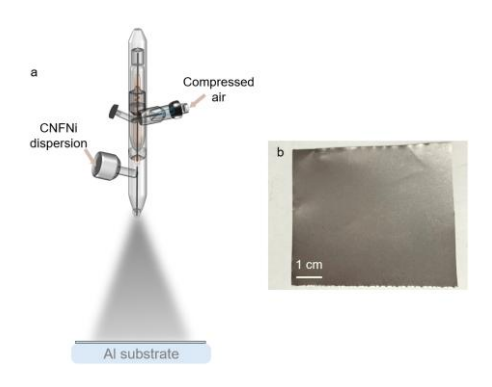


Figure 4.1. (a) Illustration of spray-painting and (b) photograph of CNFNi@Al.

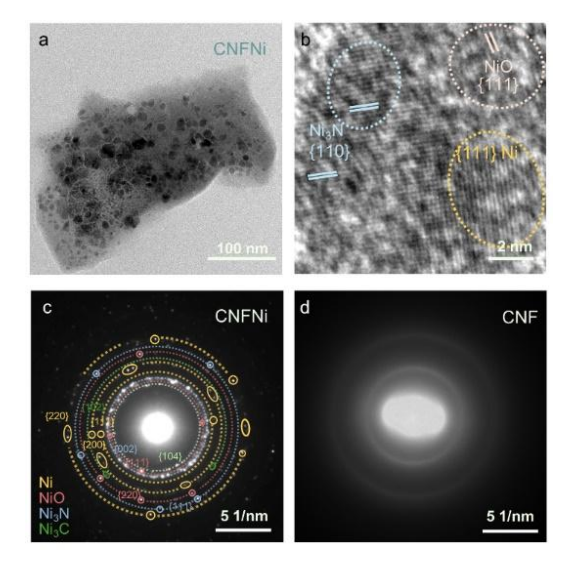


Figure 4.2. (a) Morphology and (b) lattice fringes of components of CNFNi captured via high-resolution TEM. SAED patterns for (c) CNFNi and (d) CNF.

The NiO is formed from the oxidation of Ni particles, and Ni₃N stems from the reaction between the NiCl₂ solution and N₂H₄ reducant during the chemical reduction procedure. They exhibit a high affinity to K according to previous reports $^{155, 156}$. A few

Ni₃C species should be derived from the interaction between Ni²⁺ and carbon atoms on the CNF matrix. It is found that with the introduction of Ni species, the ratio of D band to G band intensity (I_D/I_G) decreased from 1.03 to 0.98 from Raman patterns (**Figure 4.3a**). This originates from the catalysis effect of Ni species to increase the crystallinity of CNF¹⁵⁷. The presence of Ni-N, Ni-O, Ni-C, and Ni⁰ peaks in the Ni 2p spectrum (**Figure 4.3b**) obtained from XPS supports the above results as well. Based on the TGA results (**Figure 4.3c**), the amount of overall Ni species in CNFNi is estimated to be approximately 31wt.%. Most of them are presented in terms of metallic Ni, as indicated by the XRD results (**Figure 4.3d**).

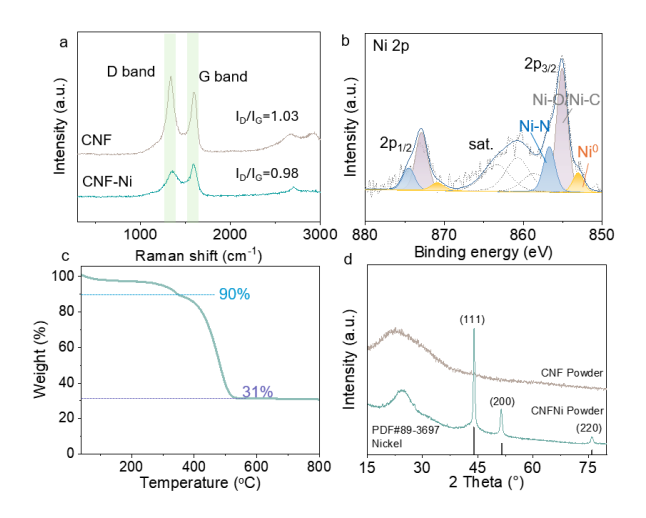


Figure 4.3. (a) Raman patterns of CNF and CNFNi samples. (b) Ni 2p spectrum and (c) TGA curve of CNFNi powder under synthetic air atmosphere (80% N₂+20% O₂). (d) XRD profiles of CNF and CNFNi.

After spray painting the CNFNi dispersion on Al foil, contact angle measurements were then employed between bare or spray-coated Al foils and the 1M 83

bis(fluorosulfonyl)imide potassium/ethyl glycol diethyl ether (1M KFSI/DEE) which is selected for its superior stability towards the K anode according to our previous work⁶². CNFNi@Al exhibits better wettability with a lower contact angle of 10.9° (**Figure 4.4a**), which guarantees the electrolyte contact and promotes uniform SEI generation¹⁵⁸. Additionally, the dropping angle of molten K on CNFNi@Al is 35.2° (**Figure 4.4b**), much smaller than that of Al (90.1°), indicating the improved K affinity.

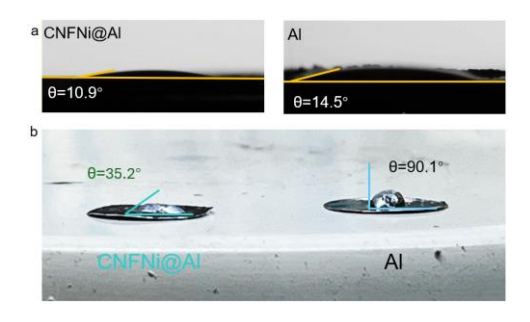


Figure 4.4. Wetting angles of (a) the DEE electrolyte and (b) molten K on Al or CNFNi@Al.

The work function (W_f) values of different current collectors were determined by UV photoelectron spectroscopy (UPS) (**Figure 4.5**). Compared to bare Al foil, the CNF-coated Al foil (denoted as CNF@Al), and CNFNi@Al possess high work function values of 3.97 eV and 4.2 eV, respectively, which corresponds to a low E_f for CNF@Al and CNFNi@Al (W_f = E_{vac} - E_f , E_{vac} =0 eV)¹⁵⁹. It can be ascribed to the higher electronegativity of Ni and CNF than Al^{160, 161}, causing a lower electron density for modified Al. Upon discharging for the asymmetric cells coupled with K as the counter

electrode, the Fermi level of current collectors undergoes an ascending trend (**Figure 4.6** as a result of electron rearrangement on the current collector ¹⁶². The E_f positions of CNF@Al and CNFNi@Al are found lower than that of Al regardless of the discharging depth, implying the narrowed energy gap between E_f and E_r. A narrowed energy gap is favorable for restricting the excessive consumption of electrolytes and regulating SEI ingredients.

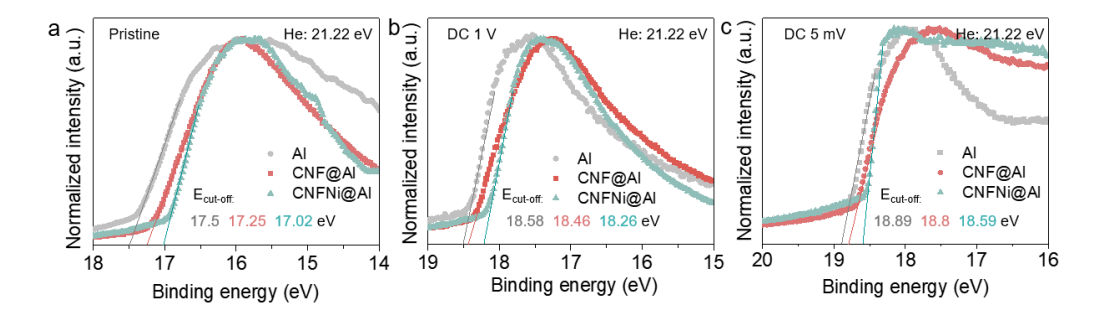


Figure 4.5. UPS profiles of Al, CNF@Al, and CNFNi@Al at different states.

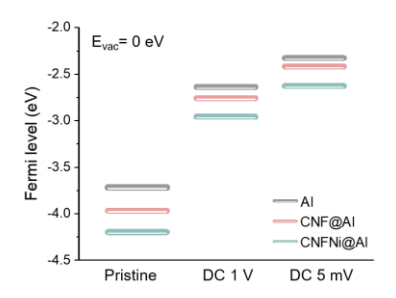


Figure 4.6. Calculated Fermi-level positions based on work function.

To verify this assumption, we probe compositions of SEI generated on different current collectors after three formation cycles at 5 mV-1 V under the current density of 0.05 mA cm⁻¹ via XPS tests. The overall percentages of elements are compared first (**Figure 4.7**). Generally, F, N, S, and K elements stem from the reduction products of

[K ion-FSI anion] and the C element comes from the reduction of solvents. Both reductions of anions and solvents can generate O-containing products but solvents are the main contributors¹⁶³. Considering the possible interference of carbon from CNFs on modified Al, we mainly compare the amount of F, N, S, and K elements. They account for a higher amount for CNF@Al and CNFNi@Al samples compared to bare Al, suggesting relatively more anions reduction on the modified Al with a lower Fermi level, and implicating the role of CNF in modulating the SEI formation. The sharp decrease in O element content and the weakened O 1s peak (**Figure 4.8a-b**) of decorated Al samples further confirm the less solvent decomposition.

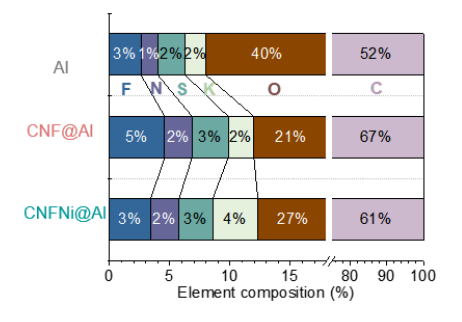


Figure 4.7. Overall element composition of SEIs generated after 3 formation cycles at 5 mV-1 V.

There are also distinct differences in organic or inorganic reduction species of SEIs, as indicated in N 1s, S 2p, and F 1s spectra (**Figure 4.8c-e**). According to **Figure 4.8f**, N_xO_y and ROSO₂- from organic species account for 76% of N 1s and 64% of S 2p for bare Al, which are higher than 70% and 61% for CNF@Al. These values further

drastically decrease to 47% and 31% for CNFNi@ Al, corresponding to an inorganic-rich SEI on CNF@Al and CNFNi@Al. Additionally, CNFNi@Al induces a greater content of K-F, K-N¹⁶⁴, KNO₃, KNO₂¹⁶⁵, and K₂SO₄ in SEI, as a result of [K ion-anion] reduction. Among these inorganics, the KF is typically considered to exhibit a high electron tunneling barrier, similar to the role of LiF¹⁶⁶, which prevents continuous electrolyte consumption.

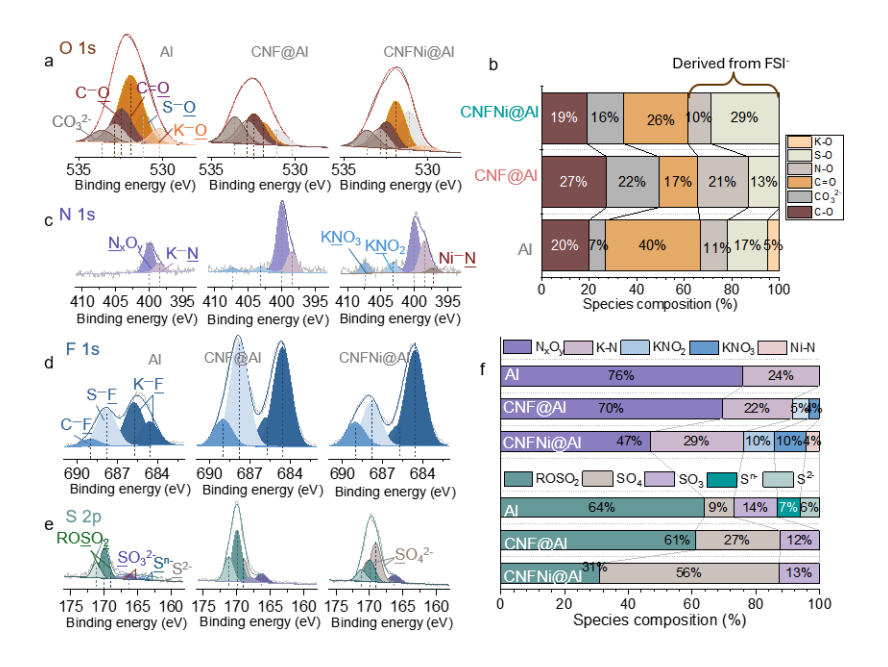


Figure 4.8. (a) O 1s of SEIs generated after 3 formation cycles at 5 mV-1 V. (h) Species composition analyzed based on N 1s and S 2p spectra. (b) Species composition in O 1s spectra. (c) N 1s, (d) F 1s, (e) S 2p spectra of SEIs. (f) Species composition based on N 1s and S 2p spectra, respectively.

4.2.2 Potassium Nucleation Behavior

We then explored the nucleation dynamics of K on different current collectors. As

shown in **Figure 4.9a**, the nucleation potential of Al, CNF@Al, and CNFNi@Al is 374.8, 141.9, and 80.3 mV respectively. It means a smooth K embryo generation process with a lower formation barrier for decorated Al. Moreover, the less mass-transfer potential of K on CNFNi@Al (**Figure 4.9b**) indicates a relatively facile growth period to achieve an intact metallic layer as well. The reason lies in the fast charge transfer in the CNFNi@Al-based cell. It exhibits the highest current exchange density of 3.82×10^{-2} mA cm⁻², as determined by Tafel curves (**Figure 4.9c**).

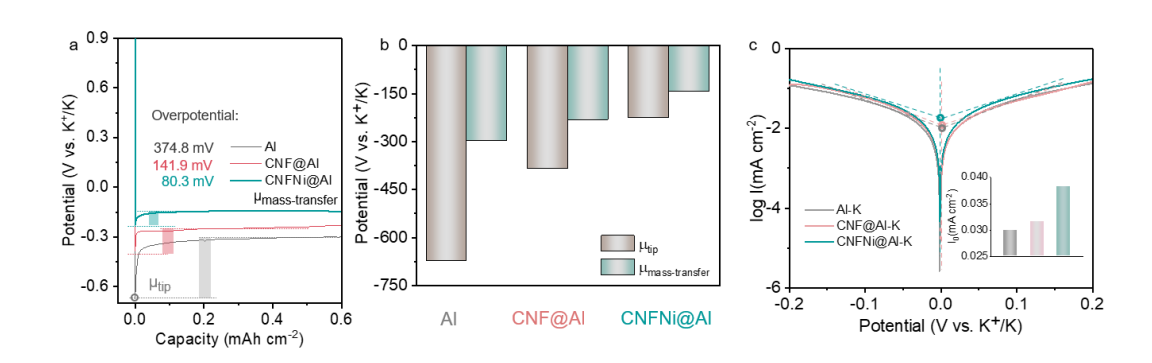


Figure 4.9. (a) The potential-capacity plots of K||current collector cells at 0.5 mA cm⁻²-1 mAh cm⁻². (b) Comparison of μ_{tip} and $\mu_{mass-transfer}$ of asymmetric cells based on different current collectors. (c) Tafel plots of symmetric cells based on different current collectors.

To further probe the nucleation behavior, the I-t measurements at different overpotentials were carried out and we compared the shape of normalized $(I/I_m)^2$ - (t/t_m) profiles (**Figure 4.10**) with nucleation models described by Scharifker and Hills^{167, 168}. Typically, they introduced two models named instantaneous (Equation 4.1) and

progressive ones (Equation 4.2) (**Figure 4.11**) through the following equations:

$$\left(\frac{I}{I_m}\right)^2 = \frac{1.9542}{t/t_m} \left\{1 - exp[-1.2564(t/t_m)]\right\}^2 \tag{4.1}$$

$$\left(\frac{l}{l_m}\right)^2 = \frac{1.2254}{t/t_m} \left\{1 - exp[-2.3367(t/t_m)^2]\right\}^2 \tag{4.2}$$

where $I_{\rm m}$ is the maximum absolute value of current density, and $t_{\rm m}$ indicates the corresponding time. The experimental profiles for all the samples nearly coincide with the instantaneous model no matter the differences in overpotentials.

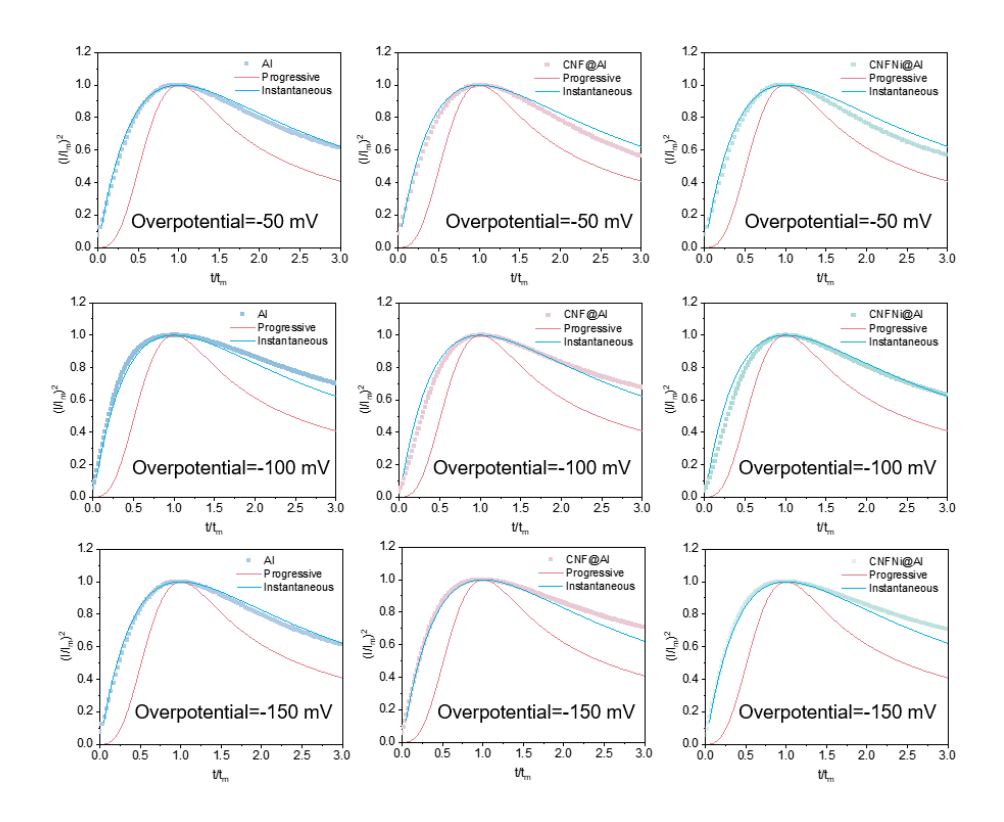


Figure 4.10. $(I/I_m)^2$ - (t/t_m) profiles of different asymmetric cells with different current collectors with the overpotential of -50, -100, and -150 mV.

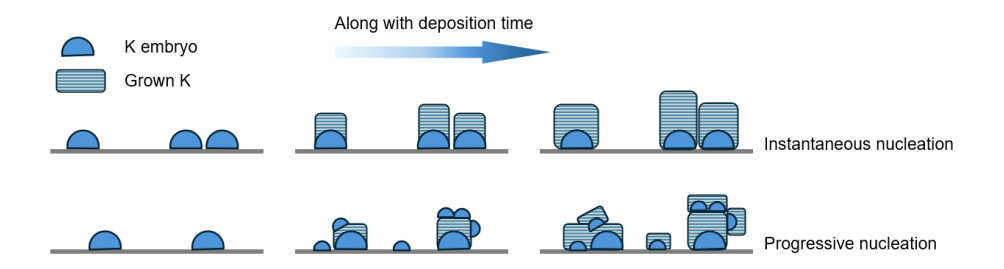


Figure 4.11. Illustration of two nucleation models.

This can be interpreted that the K embryo is only generated in the initial deposition period, and the initial nucleation number drastically influences the subsequent deposition behavior and morphology. We then calculated the nucleation density based on the instantaneous model and the following equation 169:

$$N = 0.065 (8\pi C V_m)^{-1/2} \left(\frac{nFC}{I_m t_m}\right)^2 \tag{4.3}$$

In this relationship, C represents the K ion concentration in the electrolyte, $V_{\rm m}$ is the mole volume (39.098/0.862 cm³·mol⁻¹), the ratio of mole weight to density, of deposited K, and nF indicates the transferring charge (1×96485 C·mol⁻¹).

It is a delight that the K nuclei number density on CNFNi@Al is much greater than that of Al under different overpotentials (**Table 4.1**). Abundant K nuclei can provide more ideal growth sites for the subsequent deposition of K, guaranteeing a more comprehensive and coherent K deposition layer. This proves the above assumption that nickel-containing species decorated Al can induce a smoother nucleation process.

Table 4.1. Calculated nucleation density at different overpotentials.

Current collector	$I_{\rm m}$ (mA cm ⁻²)	<i>t</i> _m (s)	Nucleation density (N cm ⁻²)	Overpotential (mV)
	-0.0888	0.0072	$1.39*10^{15}$	-50
Al	-0.1913	0.012	$1.07*10^{14}$	-100
	-0.173	0.012	$1.32*10^{14}$	-150
	-0.0919	0.0064	1.64*10 ¹⁵	-50
CNF@Al	-0.1359	0.01	$3.47*10^{14}$	-100
	-0.164	0.011	$1.74*10^{14}$	-150
	-0.0598	0.0064	3.87*10 ¹⁵	-50
CNFNi@Al	-0.1272	0.0094	$3.5*10^{14}$	-100
	-0.154	0.0104	$2.2*10^{14}$	-150

SEM and AFM were subsequently employed to detect the morphology of 10th plated K at 0.5 mA cm⁻²-1 mAh cm⁻². Upon disassembly for sample preparation, we observed numerous K dendrites penetrating the Celgard separator and trapped on the GF/D separator in the K||Al cell and several K tiny particles left in the K||CNF@Al one (Figure 4.12a). In stark contrast, almost no K signals were discernible in the separator of CNFNi@Al-based cell. Additionally, CNFNi@Al induces a relatively compact and uniform K deposition layer with a homogenous SEI component (C atom as the presentative) over a large area (Figure 4.12b), while there are numerous irregular protrusions on the deposited K in the pure Al case (Figure 4.12c). The captured pores should be related to these K dendrites left on the separator, resulting in broken SEI with limited detective C signal. Such flat deposition of K can be further explained by the extremely highest intensity of K {110} plane on the CNFNi@Al sample (Figure 4.12d)

compared to the bare Al and CNF@Al ones, which is likely derived from more negative adsorption energy of Ni to K, as the similar case in LMB¹⁷⁰.

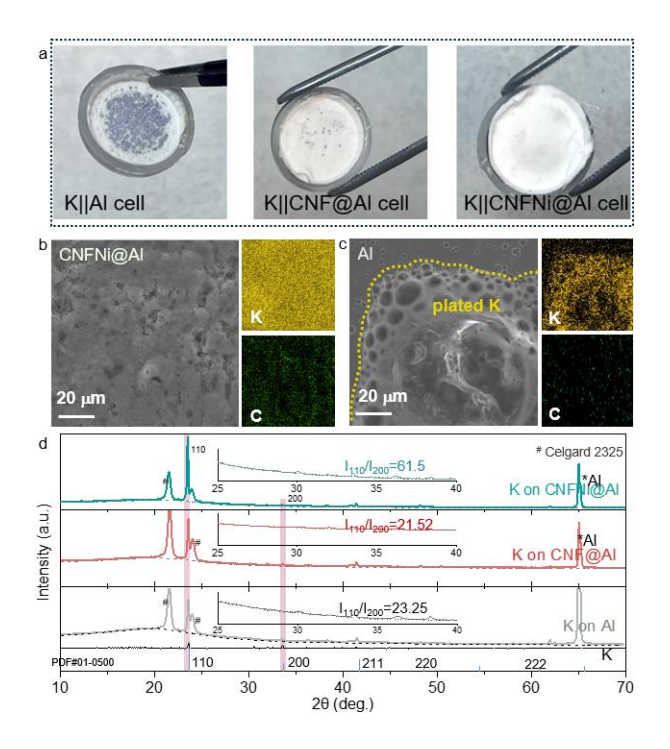


Figure 4.12. (a) Photographs of the GF/D separator in disassembled coin cells. (b-c) SEM images with EDS mappings and (d) XRD patterns of 10th-plated K on different current collectors.

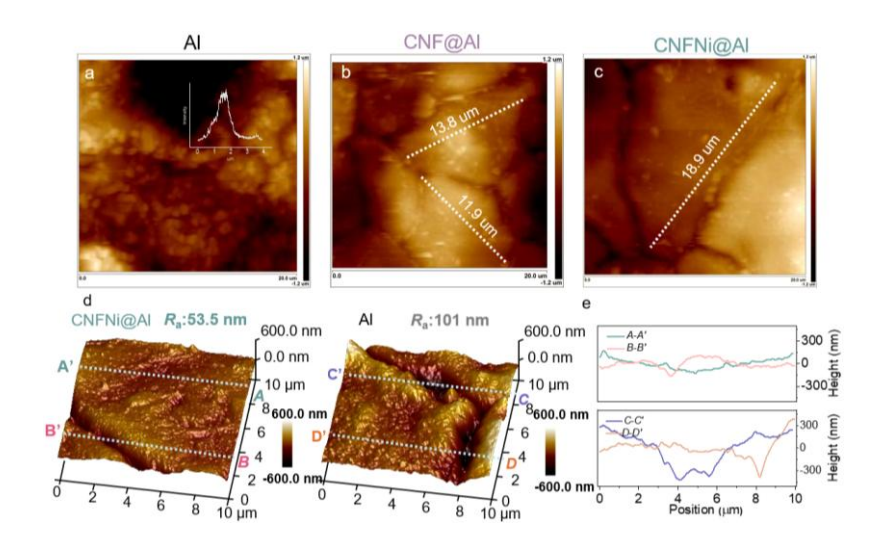


Figure 4.13. (a-c) Planer images of 10th-plated K on Al, CNF@Al, and CNFNi@Al.

(d) Three-dimensional AFM topography of 10th-plated K on A and CNFNi@Al. (e)

Height variation curves on marked lines in d.

We then probed the grain size and the roughness of plated K. The deposited K on bare Al behaves as randomly aggregated tiny grains with an average diameter of 2 µm (**Figure 4.13a**). In comparison, the K on CNF@Al possesses a larger grain size of around 13 µm and a relatively plane morphology (**Figure 4.13b**). The K grain size is even as large as 19 µm on the CNFNi@Al collector, showing a smoothest morphology with limited roughness *R*a of 53.5 nm and a smaller height variation (**Figure 4.13c-e**), evidencing the facilitated nucleation process. Having demonstrated the benefits of Ni incorporation in potassium nucleation, we center mainly on the CNFNi@Al sample in the following discussion for clarity.

4.2.3 SEI on Deposited K

We examined the composition of SEI generated on plated K layers through XPS and TOF-SIMS measurements. The overall intensities of C 1s-K 2p, O 1s, S 2p, and F 1s spectra are considerably weakened for the CNFNi@Al sample compared to those for bare Al except for the N 1s (**Figure 4.14-4.15**), which is due to the initial presence of Ni₃N species. Such declined intensities can be attributed to the suppressed electrolyte decomposition including both solvents and [K ion-FSI anion]. It is also proven by a downshift in K 2p as a result of the appearance of strong K⁰ peaks in C 1s (Figure 4.14a)

after etching for 20 s.

Comparable findings are observed in TOF-SIMS images and depth profiles. The overall S and F signals are weaker in CNFNi@Al (Figure 4.16). For both samples, the density of K ions increases with sputtering but it is more uniform for CNFNi@Al. The intensity of K ions reaches the maximum after sputtering 270 s (Figure 4.17a) for CNFNi@Al, compared to 640 s for Al. The strong signals of metallic K and a short time to reach maximum intensity suggest a small SEI thickness due to limited electrolyte reduction in CNFNi@Al-based cells. It is consistent with the thickness (t) obtained from AFM-based nanoindentation curves for the CNFNi@Al sample (Figure 4.17b).

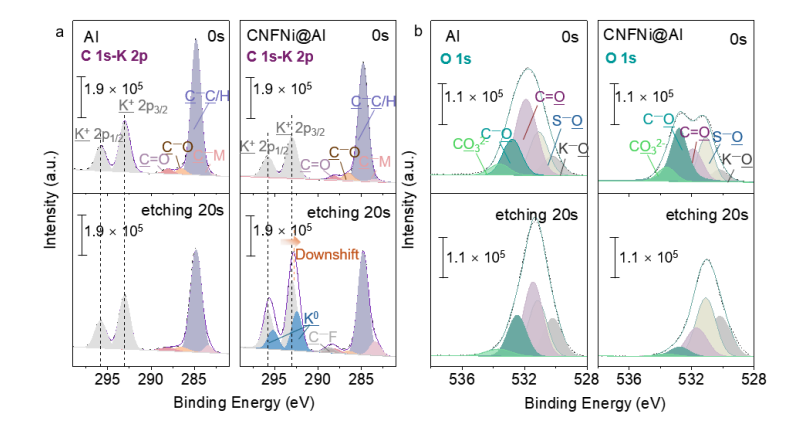


Figure 4.14. (a) C 1s-K 2p and (b) O 1s spectra of 10th-plated K on Al and CNFNi@Al current collectors, respectively.

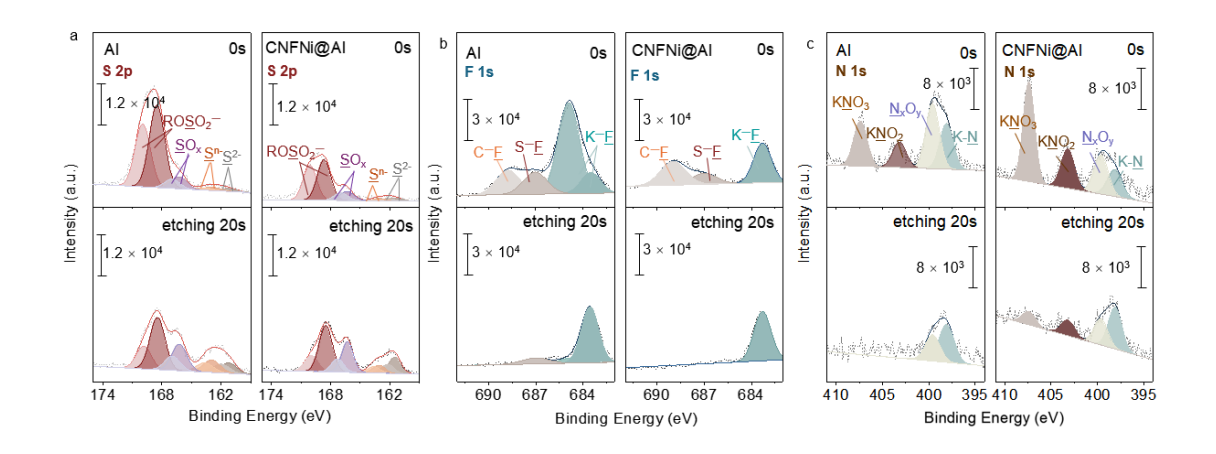


Figure 4.15. (a) S 2p, (b) F 1s, and (c) N 1s spectra of 10th-plated K on Al and CNFNi@Al current collectors, respectively.

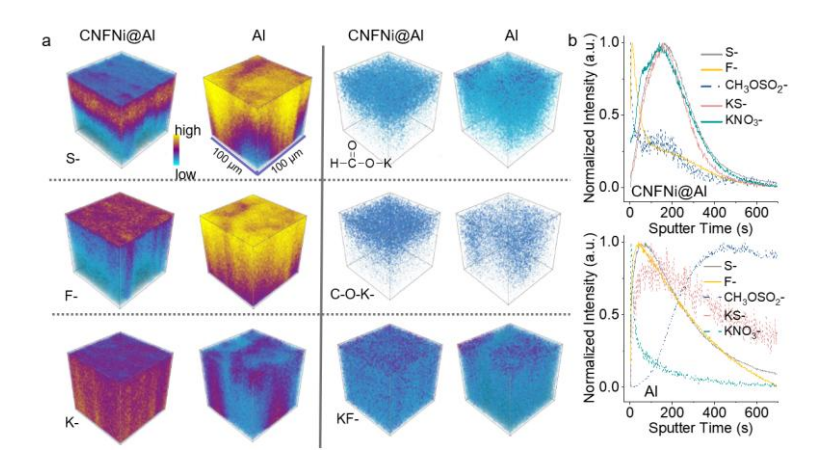


Figure 4.16. (a) TOF-SIMS 3D rendering images of S, F, K, HCO₂K, C-O-K, and KF signals. (b) Depth profiles for S, F, CH₃OSO₂, KS, and KNO₃.

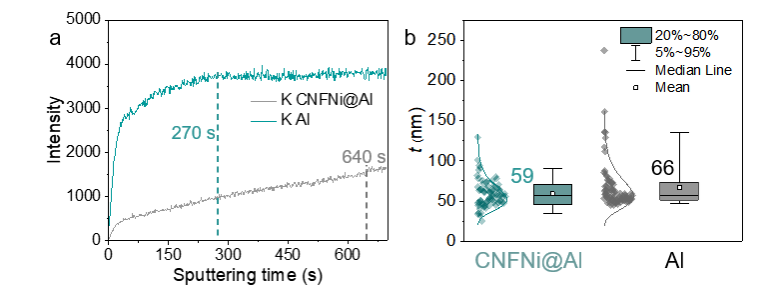


Figure 4.17. (a) TOF-SIMS depth profiles for K signal. (b) The approximate SEI thickness (*t*) obtained from AFM-based nanoindentation measurements on 10th-plated

K on different substrates.

XPS results also indicate that the SEI composition for the CNFNi@Al sample is composed of a higher content of inorganic species (Figure 4.14-4.15) and a higher C-O proportion than C=O compared to that for bare Al. This observation aligns with the findings from the previous analysis of the formed sample. 3D TOF-SIMS rendering images with corresponding depth profiles further visualize such composition (Figure 4.16). HCO₂K displays as a dominant component for the Al sample within almost depth, while C-O-K accounts for a small proportion. In contrast, HCO₂K and C-O-K only appear at the upper of the modified sample, with a relatively high content of C-O-K. It can be attributed to a more severe and deeper decomposition of DEE solvent on Al, with a lower content of elastic oligomer [CH₂OCH₂]_n but a higher content of HCO₂K¹⁷¹, 172, as illustrated in the proposed decomposition of DEE (Figure 4.18). This decomposition, however, is suppressed for the CNFNi@Al. The KCO3 signal from K₂CO₃ on the surface of the CNFNi@Al sample (Figure 4.19) could be a good insulating medium for electron tunneling¹⁷³. Considering that the C-containing species only stem from the solvent decomposition, the decrease of these C-based signals with sputtering in both samples suggests the latter beginning of the solvent decomposition compared to salts, aligned with the assumption before.

Figure 4.18. Proposed typical decomposition scheme of DEE solvent with the interaction of K ion.

Additionally, KF, a better insulator than $K_2CO_3^{28,166}$, is homogeneously distributed within the SEI layer of CNFNi@Al, effectively prohibiting excessive electrolyte decomposition. The KS, KNO₃, and K_2N account for higher contents in the CNFNi@Al sample than those of the bare Al (**Figure 4.19a**) originating from a relatively higher content of anion decomposition. More inorganic components with high ionic conductivity for SEI on deposited K would facilitate the K ion diffusion¹⁷⁴. As a result, the impedance of SEI (R_{SEI}) of the CNFNi@Al-based cell is 27.1 Ohm, half of that for Al-based. The charge transfer resistance is dramatically decreased from 2634 Ohm to 454.5 Ohm with the CNFNi decoration on Al (**Figure 4.19b-c**). This is further validated by the calculation results from Nyquist plots at various temperatures (**Figure 4.20** and **Table 4.2**). The K||CNFNi@Al cell exhibits a lower activation energy for charge transfer, at 40.65 kJ mol⁻¹, half of that in the K||Al cell.

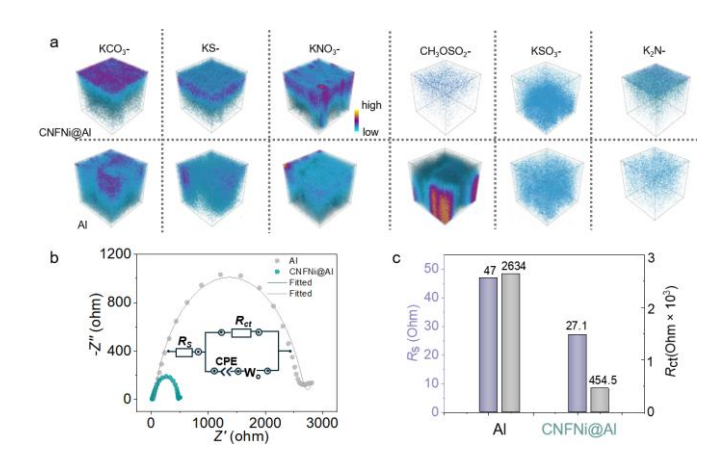


Figure 4.19. (a) TOF-SIMS 3D redering images of KCO₃, KS, KSO₃, CH₃OSO₂, KNO₃, and K₂N signals. (b) EIS results with (c) simulated resistance values of asymmetric cells after 10th plating based on different current collectors.

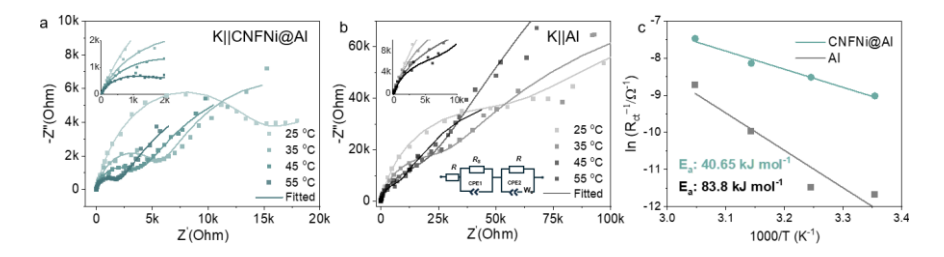


Figure 4.20. Nyquist plots of (a) CNFNi@Al and (b) Al-based asymmetric cells at different temperatures with the inset of equivalent circuit. (c) Derived activation energy values for charge transfer.

Table 4.2. Summary of the fitted interface resistance values from Nyquist plots.

$R(\Omega)$	Sample	25 ℃	35 ℃	45 °C	55 ℃
D	Al	22	20	17	16
R_b –	CNFNi@Al	9	7	6	6
R _{SEI}	Al	230,570	230,610	328,900	327,700
	CNFNi@Al	12,204	19,053	21,257	20,876
R _{ct} -	Al	117,500	97,800	21,340	6,130
	CNFNi@Al	8,250	5,003	3,427	1,760

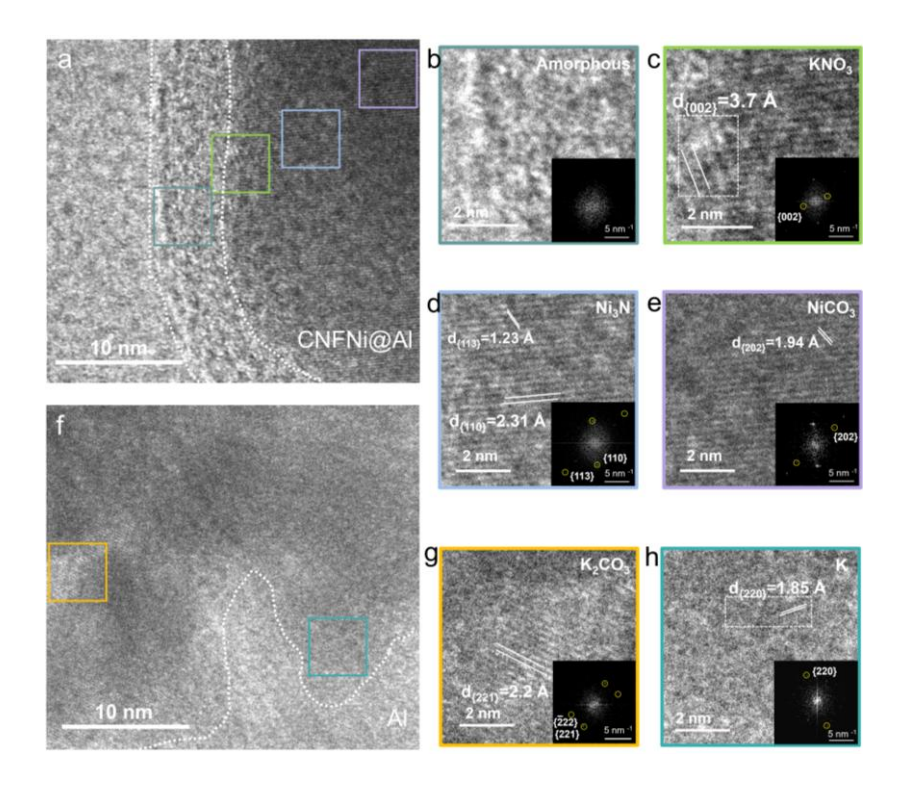


Figure 4.21. HRTEM images of SEI formed on (a-e) CNFNi@Al and (f-h) Al.

We collect the high-resolution transmission electron microscopy (HRTEM) images of SEIs to further explore their morphology and composition. As shown in **Figure 4.21a-c**, an almost amorphous layer with a uniform thickness of about 5 nm was generated on cycled CNFNi@Al, with a few low-crystalline inorganic species of KNO₃. It implies that most generated inorganic species in SEI over CNFNi@Al exist in the non-crystalline state. The KNO₃ is confirmed by the lattice fringe of 3.7 Å for {002} plane and the corresponding FFT pattern of {002} and {202} planes in Figure 4.21c. Apart from the lattice of KNO₃, the most obvious fringes and FFT patterns are indexed to Ni₃N by {110} and {113} planes (**Figure 4.21d**), the bulk species of CNFNi. We speculate that the generation of low-crystalline KNO₃ was partly catalyzed by Ni₃N.

Furthermore, in the bulk region, we observed the fringes of {202} plane of NiCO₃ (**Figure 4.21e**), which is not an ingredient in the initial CNFNi and should be a possible result of the interaction between the Ni species with electrolyte¹⁷⁵. In stark contrast, K₂CO₃ in a size of several nanometers has been observed on the bare Al sample (**Figure 4.21f-g**) with the {222} and {221} planes detected. It derives from deep electrolyte decomposition (Figure S30). As shown in **Figure 4.21h**, the captured lattice of 1.85 Å is well aligned with the {220} plane of K, as a potential dendrite isolated within the SEI on the Al surface.

The SEI composition would have a great impact on the mechanical properties, which were explored through AFM-based nanoindentation tests. Three typical mechanical parameters Young's modulus E, elastic strain limit ε_Y , and the maximum energy of elastic deformation $U(U \propto E \cdot \varepsilon_Y^5)^{62}$ were calculated and compared. The SEI generated on bare Al possesses a high E of 582 MPa and a low ε_Y of 0.24 (**Figure 4.22a-b**). In comparison, the CNFNi@Al induces an SEI with a higher ε_Y of 0.39 and a lower E of 278 MPa, implying superior elastic properties. It results from the existence of more oligomer-like species $[CH_2OCH_2]_n$ in modified samples, which further decompose into HCO₂K under the continuous electron convey in bare Al counterpart 171,172 , as indicated in previous XPS and TOF-SIMS results. The four times larger U value of 63 pJ for the CNFNi@Al sample than the Al-based one suggests a stronger overall mechanical

property (**Figure 4.22c**). Therefore, this thin yet elastic SEI generated in the CNFNi@Al-based cell is promising to protect deposited K from parasitic reaction from SEI fraction.

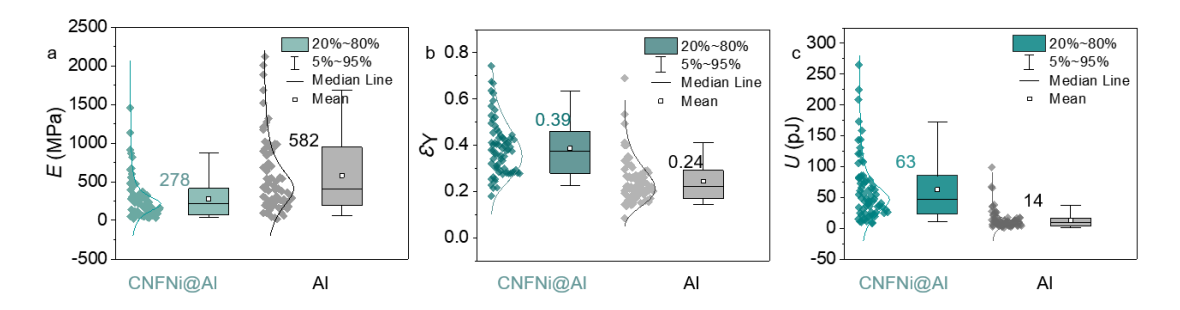


Figure 4.22. Distribution curves of testing values of (a) Young's modulus E, (b) elastic strain limit ε_Y , and (c) U values of SEI on different substrates.

4.2.4 Electrochemical Performance

Benefitting from stable SEI and promoted nucleation behavior, CNFNi@Al induced an initial CE of 99.3%, as measured through the Aurbach method¹⁷⁶ (**Figure 4.23a**). In contrast, the bare Al and CNF@Al witness a short circuit after being plated with a 2.5 mAh capacity of K, resulting in inferior performance. The CE over 100% can be attributed to the soft short circuit for CNF@Al. In terms of the long-term operation (**Figure 4.23b**), CNFNi@Al also guarantees K with an ultra-stable plating-stripping behavior of over 1500 h with an average Coulombic efficiency (ACE) over 99.2% at 0.5 mA cm⁻²-1 mAh cm⁻², outperforming than CNF@Al of 98.7%. This value is superior to reported modified potassium metal anodes (**Table 4.3**).

Table 4.3. Comparison of electrochemical performance of asymmetric cells between state-of-the-art modified anode and this work.

Electrodes	Condition	Electrolyte	Cycle number	Coulombic Efficiency, %	Ref.
SnS ₂ @CP	0.25 mA cm ⁻² 0.25 mAh cm ²	3M KFSI DME	150	>95	177
Al@G	0.5 mA cm ⁻² 0.5 mAh cm ²	4M KFSI DME	500	99	178
NG@P-Al	0.5 mA cm ⁻² 0.5 mAh cm ²	4M KFSI DME	1000	99.3	154
NC@GDY-Al	0.2 mA cm ⁻² 0.2 mAh cm ²	4M KFSI DME	800	99.93	179
MCNF	1 mA cm ⁻² 1 mAh cm ²	1.6M KFSI DME/TTE (3:2 in mol)	500	99.3	36
rGO@3D-Cu	1 mA cm ⁻² 0.5 mAh cm ²	0.8M KPF ₆ EC/DEC/PC	100	60	180
DN-Mxene/CNT	0.5 mA cm ⁻² 1 mAh cm ²	0.8M KPF ₆ EC/DEC	200	98.6	181
Cu ₃ Pt-Cu mesh	0.25 mA cm^{-2} 0.05 mAh cm^{2}	1M KPF ₆ EC/DEC 5%FEC	270	70	182
CBC-K	1 mA cm ⁻² 1 mAh cm ²	1M KFSI DME	350	98	183
PCNF@SnO2	1 mA cm ⁻² 1 mAh cm ²	1M KFSI DME	280	98.3	184
CNFNi@Al	0.5 mA cm ⁻² 1 mAh cm ²	1M KFSI DEE	400	99.3	This work

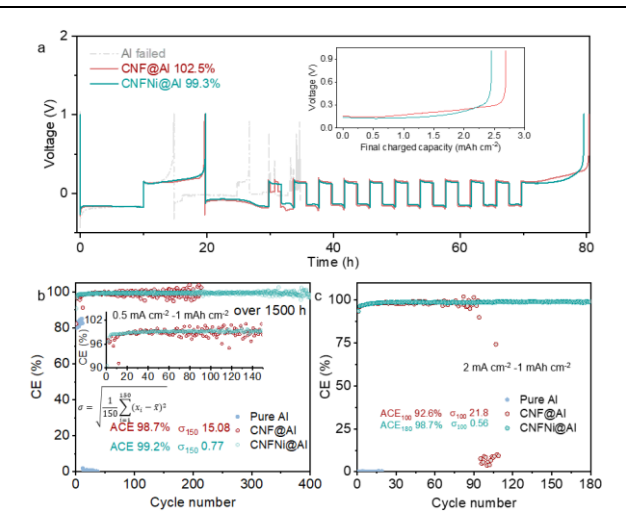


Figure 4.23. (a) Aurbach cycling profiles of asymmetric cells based on different current collectors. The long-term cycling performance of asymmetric cells at (b) 0.5 mA cm⁻²-1 mAh cm⁻² and (c) 2 mA cm⁻²-1 mAh cm⁻², respectively.

Apart from the ACE value, the fluctuation of CE varies in different current collector-based cells, which reflects the stability of the deposition-detraction behavior of K (Insets in Figure 4.23b). Here the average standard deviation values (denoted as σ) are introduced to quantify the degree of CE value fluctuation during different cycles (**Table 4.4**). In the initial 50 cycles, the CE in the bare Al-based and the CNF@Al-based one fluctuate severely, giving rise to a high σ of 37.56% and 25.97%, respectively It originates from the random deposition behavior of K leaving a certain content of "dead" K on Al and CNF@Al, which is a threat to the stability of SEI and the overall lifetime. In comparison, σ is only 1.22% in 50 cycles and further decreases to 0.61% after 300 cycles, implying the smooth plating-stripping behavior of K and stable SEI on CNFNi@Al. This advantage becomes even more distinct under a larger current density of 2 mA cm⁻² (Figure 4.23c and Table 4.5). CNFNi@Al endows the cell with an ACE of 98.7% and a low σ value of 0.56%. In contrast, bare Al cannot tolerate this great current density and fails in the initial cycle. The CNF@Al-based cell exhibits an improved performance but still fails in 90 cycles.

Table 4.4. Calculated standard deviation of CE at 0.5 mA cm⁻²-1 mAh cm⁻².

$\sigma = \sqrt{\frac{1}{n} \sum_{i=1}^{n} (\mathbf{x}_i - \overline{\mathbf{x}})^2} $ (%)	50 cycles (n=50)	100 cycles (n=100)	150 cycles (n=150)	200 cycles (n=200)	250 cycles (n=250)	300 cycles (n=300)
Al	37.56	-	-	-	-	-
CNF@Al	25.97	18.43	15.1	13.1	12.68	-
CNFNi@Al	1.22	0.91	0.77	0.68	0.65	0.61

Table 4.5. Calculated standard deviation of CE at 2 mA cm⁻²-1 mAh cm⁻².

$\sigma = \sqrt{\frac{1}{n} \sum_{i=1}^{n} (\mathbf{x}_i - \overline{\mathbf{x}})^2} $ (%)	50 cycles (n=50)	100 cycles (n=100)	150 cycles (n=150)	180 cycles (n=180)
Al	-	-	-	-
CNF@Al	0.93	21.8	30.46	-
CNFNi@Al	0.89	0.91	0.6	0.56

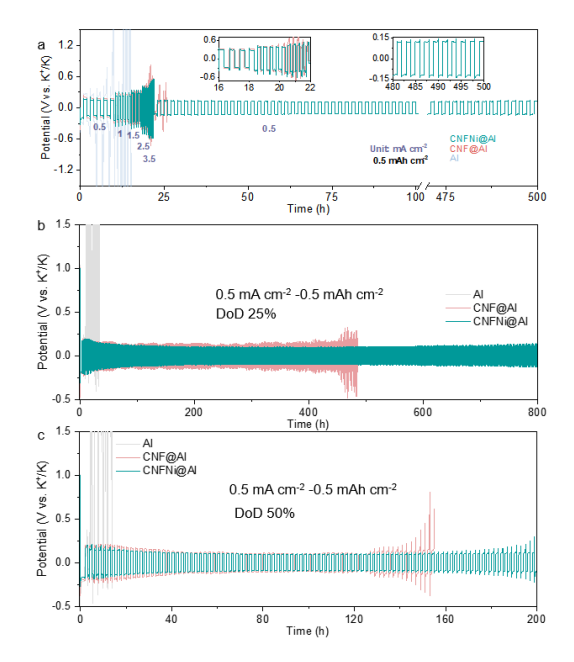


Figure 4.24. (a) Rate performance of the symmetric cells with the pre-plating capacity of 2 mAh on different current collectors. Cycling performance of asymmetric cells under (b) 25% DoD and (c) 50% DoD at 0.5 mA cm⁻²-0.5 mAh cm⁻².

To evaluate the rate performance, we pre-plated K with 2 mAh cm⁻² capacity onto different current collectors and assembled symmetric batteries. CNFNi@Al enables an excellent rate performance, especially at the current density of 3.5 mA cm⁻²: The polarization is two-thirds that in the CNF@Al cell (**Figure 4.24a**). After the current

density declines to 0.5 mA cm⁻², it still retains stable cycling for almost 500 h, while the CNF@Al-based cell undergoes a sharp short-circuit within 25 h. The harsh cycling condition was also explored by predepositing four times or twice the testing capacity of K (DoD 25% or 50%) on current collectors (**Figure 4.24b-c**). CNFNi@Al endows the cell with a lower voltage hysteresis over 800 h compared to the severe polarization in Al-based one and fierce fluctuation of CNF@Al one under 25%. Even under DoD up to 50%, the CNFNi@Al-based cell displays stable voltage profiles with limited hysteresis for over 200 h, demonstrating enhanced cyclic stability.

Having determined the improved K anode stability, the full-cell performance of PMBs was finally assessed. We initially couple the K metal anode with a FeHCF cathode that possesses an average discharge voltage of 3.3 V (Figure 4.25a-b). Compared to the Al and CNF@Al-based cells with fluctuated CE and short lifetime, the CNFNi@Al-K||FeHCF cell demonstrates a superior cycling performance with an ACE of 99.3% and the capacity retention of 91.9% after 350 cycles under the negative/positive ratio (N/P ratio) of 5. We then examined the performance in high-voltage MnHCF, which is critical to realizing a high energy density. Under a lower N/P ratio of 1, the CNFNi@Al allows stable cycling of the cell for more than 100 cycles (Figure 4.25c). Pushing to the limit, we tested the stability under the critical anode-free condition (Figure 4.25d), without precycling on the anode since it could introduce an

extra K source as pointed out by Hatzell¹⁸⁵. The CNFNi@Al||MnHCF cell can run for 50 cycles. It displays the normal charging-discharging profile with an energy density of 381 Wh kg⁻¹ (based on the mass of the MnHCF and the CNFNi), which is an improvement of anode-free PIBs using a normal-concentration electrolyte compared to the previous work listed in **Table 4.6**.

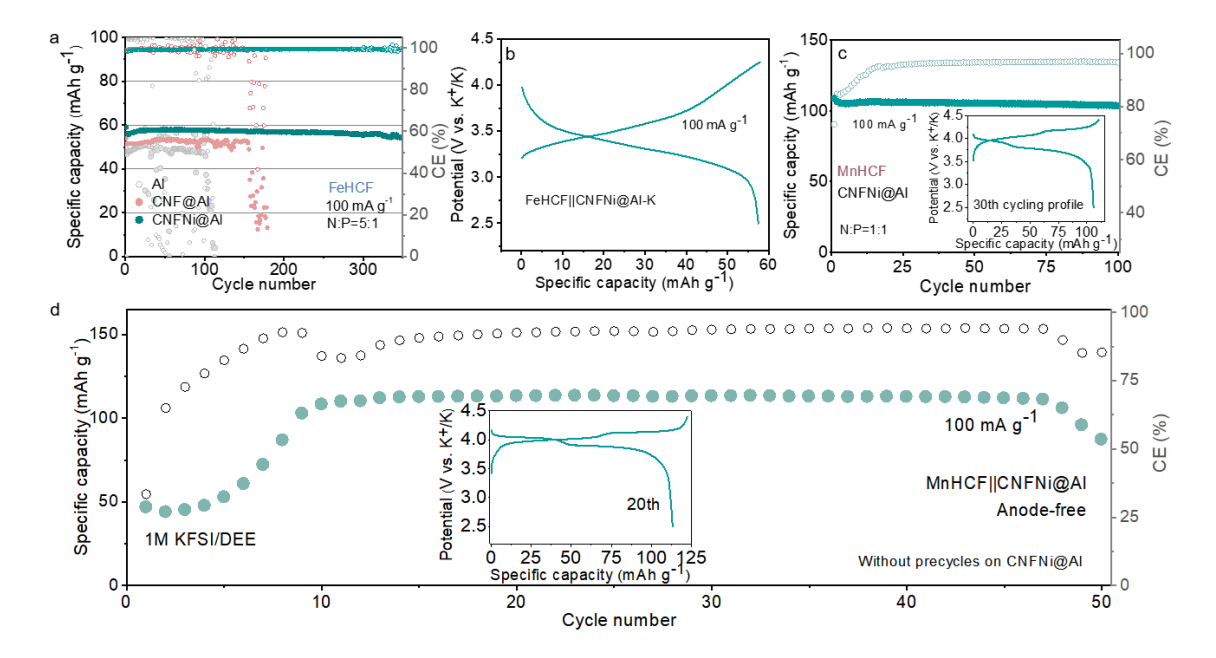


Figure 4.25. (a) The cycling performance of CNFNi@Al-K||FeHCF with an N/P ratio of 5 with (b) the cycling profile at the 50th cycle. The cycling performance of CNFNi@Al-K||MnHCF with (c) an N/P ratio of 1 and (d) an N/P ratio of 0 (Anodefree).

Table 4.6. Comparison of electrochemical performance of anode-less or anode-free full cells between state-of-the-art modified anode and this work.

Current	Anode preparation condition	Cathode	Current (mA g ⁻	Electrolyte	Cycles	Energy density* (Wh kg ⁻¹)	Capacity retention (%)	Ref.
With an almos	t unlimited supply of K on the	anode side						
Cu ₃ Pt-Cu-K	Incorporated with K (overall 12 mg cm ⁻²)~ 7920 mAh cm ⁻²	FeHCF	100	1M KPF ₆ EC/DEC 5%FEC	200	18	71.8	182
P-PMCFs	Electrodeposited with K	PTCDA	2000	1M KFSI EC/DEC	1000	-	85	29
NC@GDY- Al-K	Plated with K	FeHCF	200	4M KFSI DME	200	-	99	179
DN- Mxene/CNT	Adsorbed with 2.8 mg cm ⁻² 2 K ~ 1850 mAh cm ⁻²	SPAN	400	0.8M KPF ₆ EC/DEC	500	63.3	69.4	181
With a high su	apply of K on the anode side							
SnS ₂ @CP	Plated with 5 mAh cm ⁻² K (N/P ratio of over 10)	FeHCF	100	3M KFSI DME	200	67.6	83.7	177
NG@P-Al	Plated with 5 mAh cm ⁻² K (Unknown N/P ratio)	FeHCF	100	4M KFSI DME	400	-	72.8	154
	Plated with 0.8 mAh cm ⁻² K K- (N/P ratio of 5) PTCDA 200		560	152	80	_		
CNFNi@Al	Plated with 0.5 mAh cm ⁻² K (N/P ratio of 5)	FeHCF	100	1M KFSI DEE	350	116	97.2	This
	Plated with 0.16 mAh cm ⁻² K (N/P ratio of 1)	MnHCF	100		100	302	95.1	95.1
With a low sup	oply of K on the anode side							
MCNF	3 formation cycles between 0.01-1 V and 5 plating-stripping cycles at 0.5 mA cm ⁻² -0.5 mAh cm ⁻² (0.027 mAh cm ⁻²)	МпНСГ	20	1.6M KFSI DME/TTE (3:2 in mol)	100	362	86	36
Al@G	5 formation cycles between 0-1 V	K-FeS ₂	100	4M KFSI DME	30	95	26	178
CLYTTA' C	5 formation cycles between (1.6 mg (1.002 mAh cm ⁻²)	MnHCF (1.6 mg)	160	5M KFSI DME	200	323	87.9	This
CNFNi@Al		MnHCF (4 mg)	100	1M KFSI DEE	60	416	81.6	work
With no suppl	y of K on the anode side							
CNFNi@Al	No precycles	MnHCF (1.8 mg)	100	1M KFSI DEE	50	381	89	This work

4.3 Summary

We finely tune the surface chemistry to change the Fermi level of the Al current collector and then suppress the electrolyte decomposition using the CNFNi decoration.

Delightedly, benefitting from the elevated work function of CNFNi@Al, a thin inorganic-rich SEI with superior elasticity is generated. Secondly, potassiophilic nickel species promote the nucleation behavior of K embryos. As a result, the K anodes based on CNFNi@Al realize a high CE of 99.2% with a lifetime of over 1500 h. An anode-free MnHCF||CNFNi@Al cell can be realized with 89% capacity sustained after 50 cycles at 100 mA g⁻¹, which delivers a specific energy density of 381 Wh kg⁻¹ (based on the MnHCF and CNFNi mass). This work would provide new insight into enhancing interphase stability and achieving advanced potassium metal batteries from the perspective of electrode surface chemistry.

Chapter 5. Designing Electrolytes with Steric Hindrance and Film-forming Booster for High-voltage Potassium Metal Batteries

Apart from the anode-side modification, the electrolyte engineering on the cathode/electrolyte interface is critical as well. Ethers have been the primary electrolyte solvent candidates for reversible potassium metal anodes, but their poor oxidative stability at high voltage restricts the application, like THF and DEE reported in previous chapters. In this chapter, we focus on ether molecule design to enhance the anodic stability of ether electrolytes for advanced high-voltage potassium metal batteries.

5.1 Introduction

The realization of the high-energy PMBs relies heavily on the electrolytes, which significantly impact the stability of both the cathode and anode. On the cathode side, the full activation of Mn redox in MnHCFs necessitates a high charging voltage of 4.4 V, which may trigger severe electrolyte decomposition. Worse still, the Mn³⁺ and Fe³⁺ in the charged MnHCFs can catalyze the oxidation process of electrolytes¹⁸⁶, leading to an inferior initial Coulombic efficiency (ICE)^{8, 50, 187-189}. Moreover, the crystal structure damage from Mn dissolution in the electrolyte accelerates capacity degradation¹⁹⁰. Apart from the cathode active materials, the high-voltage charging also challenges the stability of the Al current collector. The corrosion of Al at a high voltage has been

widely observed, particularly in KFSI-based electrolytes that are preferred by the anodes and have been extensively adopted in PMBs¹⁹¹. Although the issue could be partly mitigated after forming a protection layer, this layer tends to be dissolved in the electrolytes in the presence of solvents with high salt-dissolving capability¹⁹². To alleviate the above issues, multiple strategies, including electrode materials and interphase modification, have been applied. Compared to the optimization of electrode materials¹⁹³, electrolyte regulation can concurrently cope with both cathode and anode obstacles. However, there are few proper dilute electrolytes for PMBs until now.

Instead of increasing the concentration, we tailor the molecular structure of the ether based on the most widely used G2 solvent to boost oxidative stability. By replacing the ending methoxy groups in G2 with larger-sized butoxy ones, the solvation capability of the resulting DiDBE to K ion is greatly reduced to suppress the severe solvent decomposition and thus regulate the composition of SEI/CEI in DiDBE-based electrolyte (Figure 5.1). The relatively high viscosity associated with a longer solvent chain could be readily resolved through a functional additive, i.e., DTD, which also contributes to S-rich interphases with ROSO₂K species to benefit the kinetics. Consequently, a high ICE of 92.1% has been achieved in MnHCF-type PMBs with long-term cyclic stability of over 200 cycles. The average CE of the K||carbon-coated Al (Al-C) cell has been elevated to 98.8%, accompanied by a 6-fold improvement in

the cyclic life of K||K symmetric cells compared to classic G2 and ethylene carbonate/diethyl carbonate (EC/DEC) electrolytes.

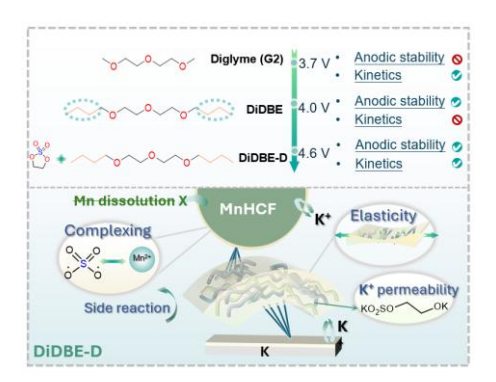


Figure 5.1. Rational design of ethers with high anodic stability and kinetics and the synergic effects of customized electrolyte in K metal batteries.

5.2 Results and Discussion

5.2.1 Rational Electrolyte Design

Glymes are the most widely explored solvents in the electrolyte for alkali-metal batteries. We first study the electrolytes of 1M KFSI in G2 by linear sweep voltammetry (LSV) (**Figure 5.2a**) in K||Al-C cells, where a carbon-coated Al is used as the working electrode to alleviate the corrosion at a high voltage. The leakage current increases to 2 μ A cm⁻² at 3.7 V for 1M KFSI/G2 due to the corrosion of Al-C (**Figure 5.2b**), consistent with the previous work¹⁹⁴. Extending the solvent chain length only slightly increases the onset voltage to 3.75 V for 1M KFSI/tetraglyme (G4), which is still unsatisfactory for developing high-voltage PMBs. It is well known that the electrochemical window of the electrolytes could be boosted by building stable interphases. Therefore, we

extend the ending alkyl groups from the methoxy group in G2 into butoxy groups to obtain the DiDBE solvent (**Figure 5.1**), aiming to weaken the K-solvent interaction to suppress the parasitic reaction. The reason lies in the i) reduced O/C ratio in the solvent molecule from 0.5 in G2 to 0.25 in DiDBE, as oxygen is the preferred K ion coordination site¹⁹⁵. ii) A steric hindrance arising from the large butoxy groups, which restrains the solvent from coordination with K ion. The resulting 1M KFSI/DiDBE electrolyte appears to be stable with the Al-C electrode up to 4.0 V with a leakage current of 2 μA cm⁻² and remains stable even when held at 4.3 V for 10 h (**Figure 5.2c-d**). Since DiDBE has the same chain length as G4, it suggests that the ending alkyl groups instead of the chain length contribute to improved oxidative stability.

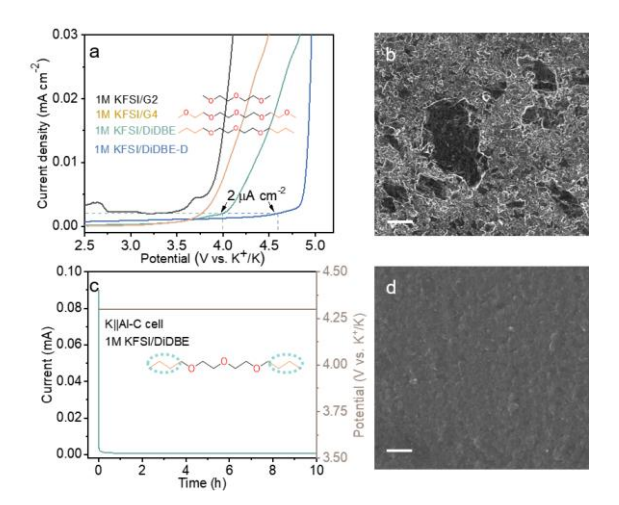


Figure 5.2. (a) LSV curves of different electrolytes with the scanning rate of 1 mV s⁻¹. (b) SEM images of the Al-C electrode after being held at 3.7 V for 10 h in 1M KFSI/G2 electrolyte. (c) Curves obtained from the Chronoamperometry measurement to hold K||Al-C cell in 1M KFSI/DiDBE electrolyte at 4.3 V for 10 h with (d) corresponding

SEM images of the tested Al-C electrode.

One drawback is that the long chain length of DiDBE also increases the viscosity (**Table 5.1**). Therefore, a commercially available solvent DTD is incorporated as an electrolyte additive, and the resulting electrolyte is denoted as DiDBE-D. With the addition of 6wt.% DTD, the viscosity of DiDBE-D is decreased from 10.96/4.4 to 8.33/2.3 mPa·s at room temperature (RT)/60 °C (**Figure 5.3a**), resulting in an increase of the electrolyte ionic conductivity from 0.56 mS cm⁻¹ to 2.15 mS cm⁻¹ at RT (**Figure 5.3b**). Furthermore, the DTD could also benefit the interphases by forming sulfur species (will be discussed later). The combined effects of the solvent steric hindrance and functional additive expand the oxidative stability to around 4.6 V which well matches the high-energy MnHCF cathode.

Table 5.1. Viscosity of G2 and DiDBE electrolytes at different temperatures.

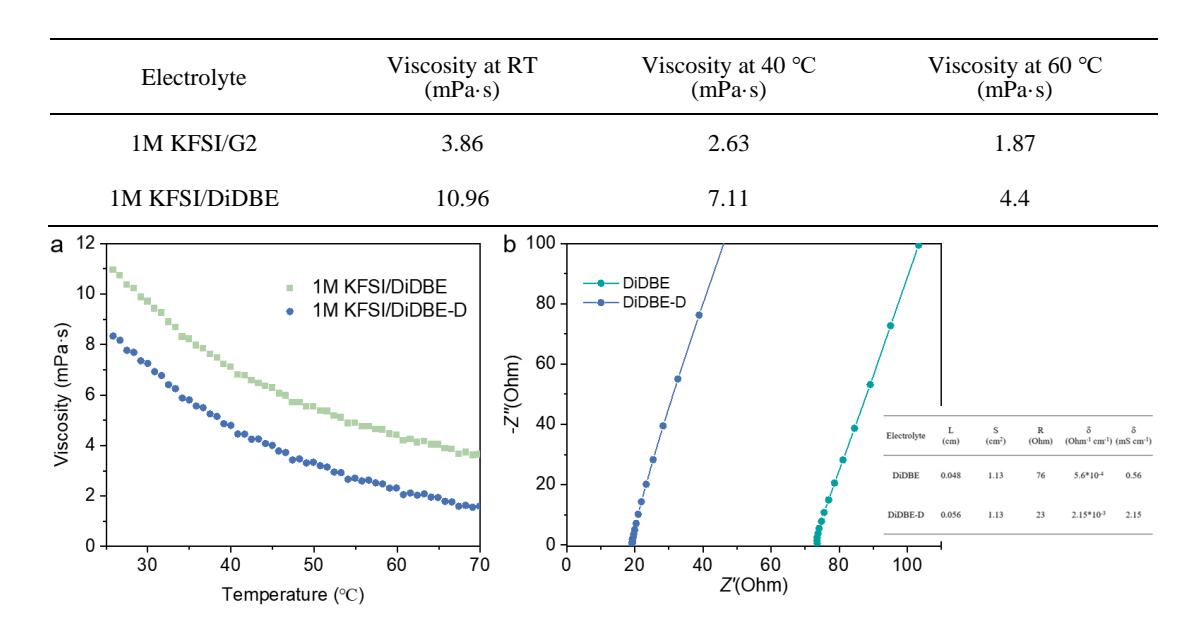


Figure 5.3. (a) The viscosity of DiDBE electrolyte and DiDBE-D electrolyte. (b) EIS

plots of two stainless steels with GF/D filled with DiDBE and DiDBE-D electrolytes for ionic conductivity measurement with corresponding data.

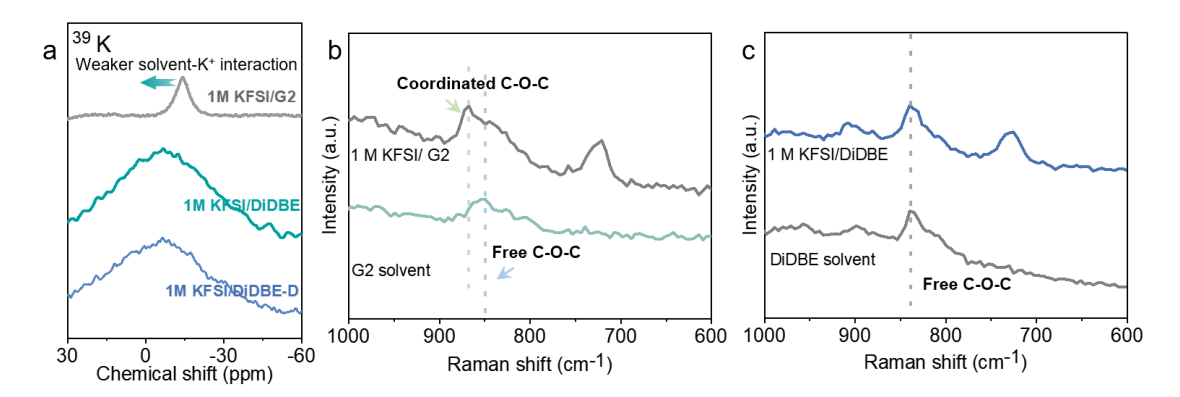


Figure 5.4. (a) ³⁹K NMR spectra of different electrolytes. Raman spectra of C-O-C vibration of (b) G2 electrolyte and (c) DiDBE electrolyte with or without salt.

To verify the above hypothesis, we first conducted nuclear magnetic resonance (NMR) measurements (**Figure 5.4a**) to analyze the ³⁹K spectrum. The cation spectrum is sensitive to the coordinating states in the solvation structures, which has been widely adopted in analyzing the electrolytes of Li/Na-based batteries through the ⁷Li/²³Na spectra^{196, 197}. Compared to the G2 electrolyte, a clear downfield shift (from -14.2 ppm to -6.7 ppm) occurs in the ³⁹K peak for the DiDBE electrolyte, implying the de-shielded K ion nuclei and reduced electron density around K ions as a result of the weaker K ion solvation in DiDBE electrolyte¹⁹⁸. The comparable ³⁹K pattern observed in the DiDBE-D electrolyte to that of DiDBE suggests that the presence of the DTD additive does not affect the weak solvating nature of DiDBE. Similar results are presented in Raman spectra of C-O-C stretching peaks in the electrolytes. The C-O-C peak of G2 blue shifts

by 18.15 cm⁻¹ in 1M KFSI/G2 electrolyte due to the K coordination (**Figure 5.4b**). In sharp contrast, a minor change is observed in DiDBE before and after dissolving the KFSI salt, confirming the weak K coordination (**Figure 5.4c**).

The coordinating environment of FSI also reflects the solvation structure. We compare the Raman peaks of the S-N-S vibration in FSI at around 700-760 cm⁻¹ for different electrolyte systems (Figure 5.5a). The deconvoluted three peaks correspond to the coordination state of solvent-separated ion pairs (SSIP), coordinated ion pairs (CIP), and ion aggregates (AGG) from low to high wavenumbers. 55.6% FSI- anions exist in the form of free SSIP under G2 electrolyte. In contrast, CIP and AGG dominate in the DiDBE electrolyte with a cumulative 66.2% concentration, further demonstrating the weaker solvating ability of DiDBE. The SSIP occupation proportion increases from 33.8% to 44.8% after DTD addition, a reflection of the ejection of several FSI anions out of the solvation structure and the DTD additive as the new participant. The difference in S=O vibration for DiDBE and DiDBE-D electrolytes (Figure 5.5b) verifies this. Upon the inclusion of DTD, the primary peak at 1219 cm⁻¹ undergoes a redshift to 1215 cm⁻¹, which reflects a reduction in ion pairings and a concurrent increase in free FSI anions. Meanwhile, a shoulder at 2102 cm⁻¹ emerges, resulting from the DTD solvent and implying the incorporation of DTD into the solvation shell that would impact the interfacial chemistry. Despite this, the DiDBE-D electrolytes still

present weak solvation compared to the G2 counterpart.

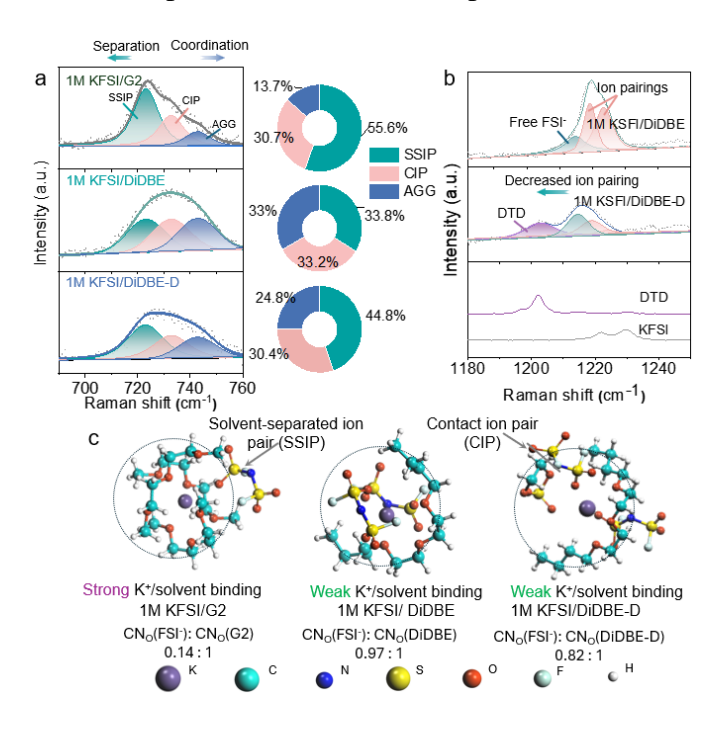


Figure 5.5. (a) Raman spectra of S-N-S vibration of different electrolytes with the relative contents of SSIP, CIP, and AGG. (b) Raman spectra of S=O vibration of different species. (c) Illustrations of the most probable solvation structure of different electrolytes extracted from MD simulations.

We further probe the solvation structure using molecular dynamics (MD) simulations. Generally, the O atom in both the solvent and the anion can coordinate with the K ion. Therefore, the ratio of the coordinated O atoms from the FSI⁻ anion and the solvent (denoted as the A/S ratio) could be used to signify the solvating capability of various solvents. As depicted in **Figure 5.5c**, there is a large preference for most G2 solvents appearing in the first inner solvation shell of K ion, leaving most FSI⁻ anions as the free SSIP state with an A/S ratio of only 0.14 in G2 electrolyte. In contrast, the

A/S ratio increases to 0.97 for the DiDBE electrolyte, suggesting a greater abundance of FSI anions surrounding K ion in the inner solvation sheath. Radial distribution functions (RDFs) (**Figure 5.6**) also imply more coordinated FSI⁻ anions and less solvent in the first solvation shell of the DiDBE electrolyte. Furthermore, the calculated solvation energy ΔG_{Solvation} for the DiDBE electrolyte is -2.16 eV, less negative than -2.93 eV for the G2 electrolyte (**Table 5.2**), which indicates that DiDBE is more weakly solvated to K ion. As a result, the average coordination number of O in DiDBE to K ion is only 3.5 (K ion-3.5 O_{DiDBE}), notably smaller than that (K ion-7.0 O_{G2}) of G2 solvent. This discrepancy indicates that DiDBE with larger-sized terminal groups and a longer chain length exhibits a weaker solvation ability than G2. The DTD additive only slightly decreases the coordinated A/S ratio to 0.82 with a $\Delta G_{Solvation}$ of -2.45 eV for DiDBE-D (Figure 5.5c), thus maintaining the weaker solvation to K ion than in the G2 electrolyte.

Table 5.2. Calculated solvation energy and coordination numbers of O in FSI anion and solvent in different electrolytes by MD simulation.

Electrolyte	Es (eV)	CN for O (FSI-)	CN for O (solvent)
1M KFSI in G2	-2.93	1.0	7.0
1M KFSI in DiDBE	-2.16	3.4	3.5
1M KFSI in G4	-3.09	1.3	7.0
1M KFSI in DiDBE-D	-2.45	3.1	3.8

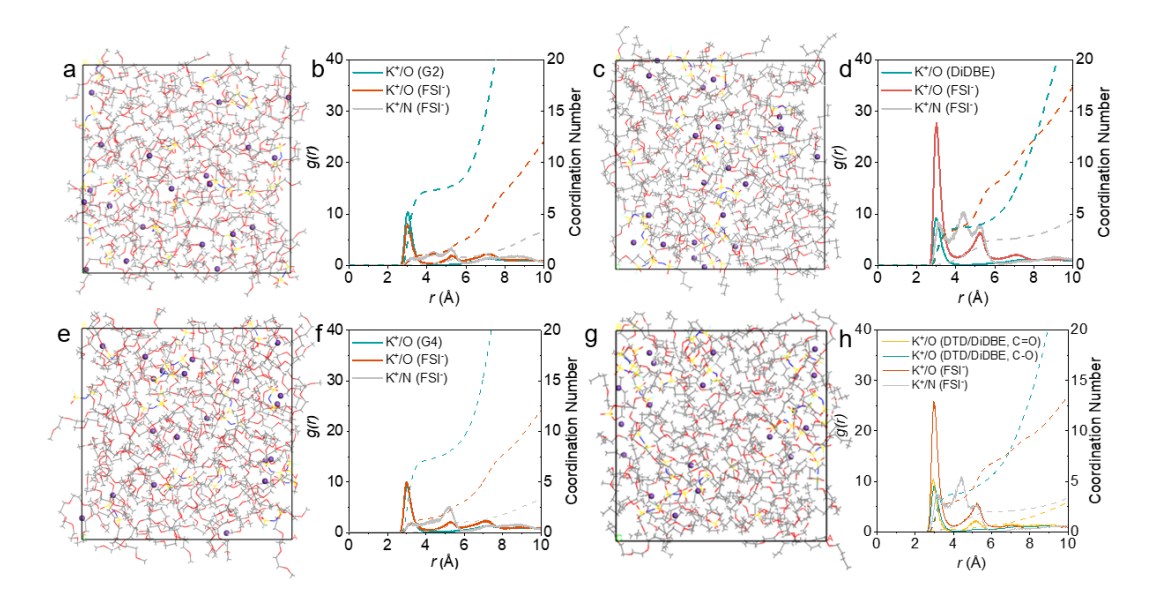


Figure 5.6. (a) Snapshots of the MD simulation cell and corresponding radial distribution function (RDF) plots for (a, b) 1M KFSI/G2, (c, d) 1M KFSI/DiDBE, (e, f) 1M KFSI/G4, (g, h) 1M KFSI/DiDBE-D.

5.2.2 Compatibility of Modified Electrolyte with MnHCF Cathode

We then studied the compatibility of each electrolyte with the MnHCF cathode, which is synthesized through the traditional co-precipitation method with iminodiacetic acid as the chelating agent. The particle size of MnHCF is around 20 nm (**Figure 5.7**). Significant over-charging is observed at 4.08 V and 4.2 V for G2 and G4 electrolytes (**Figure 5.8**), respectively, which agrees well with the LSV results. Therefore, we adopted a commonly used carbonate electrolyte (1M KFSI in EC/DEC) as a comparative benchmark to explore interfacial chemistry, which exhibits higher stability than G2 and G4 electrolytes at high voltage.

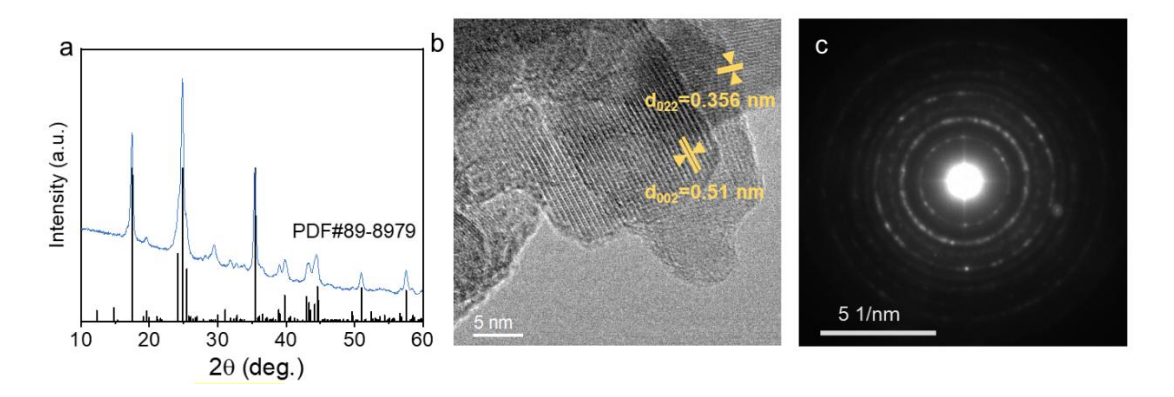


Figure 5.7. (a) XRD pattern; (b) TEM image and (c) SAED pattern of KMF.

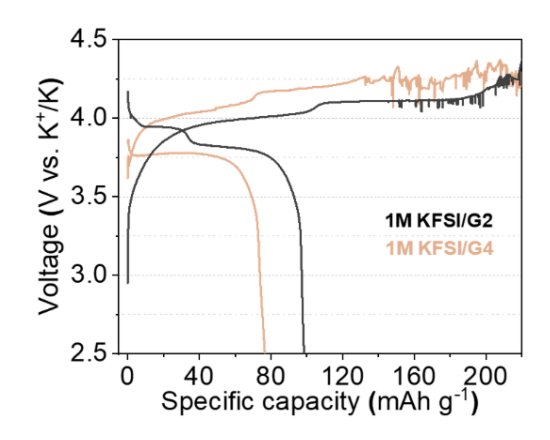


Figure 5.8. Voltage profiles of KMF in G2 and G4 electrolytes.

Although the MnHCF could be reversibly charged/discharged in carbonate electrolyte, it leaves a substantial irreversible capacity with a low ICE of 65.7% (**Figure 5.9a**) at 25 mA g⁻¹. In comparison, DiDBE electrolyte allows reversible operation of MnHCF||K cells with an ICE of 82.0%. This value is further boosted to 92.1% with the DTD additives, which is the highest one achieved in a dilute electrolyte and even exceeds most high-concentration electrolytes (**Figure 5.9b**). The outstanding ICE obtained here arises from the stabilization of not only the cathode surface but also the Al-C current collector. This is reflected by the chronoamperometry measurement

results (**Figure 5.9c**) and Al-C corrosion images (**Figure 5.9d**). Severe Al-C corrosion is detected in the EC/DEC electrolyte after being held at 4.3 V for 10 h. In contrast, the Al-C remains a smooth surface in the DiDBE-D electrolyte due possibly to the formation of a stable passivation layer, which is proved by the negligible current leakage for K||Al-C cells.

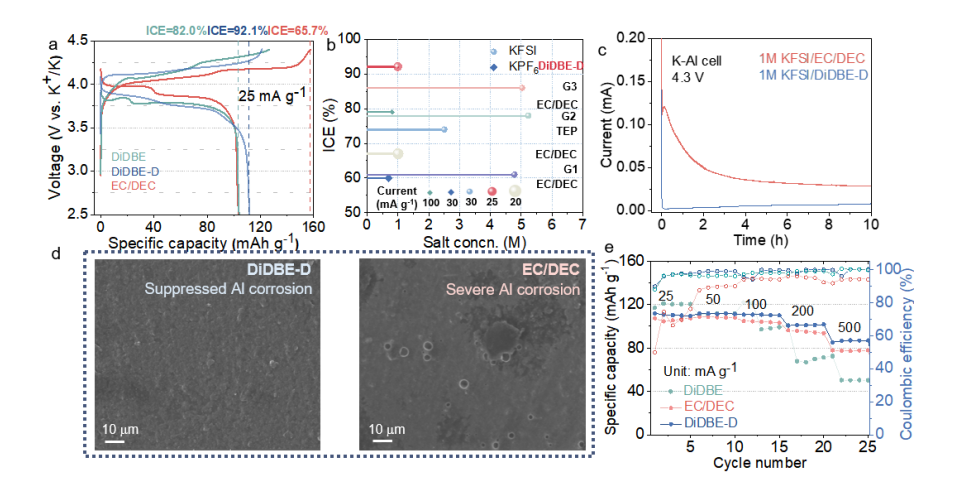


Figure 5.9. (a) Initial voltage curves of MnHCF in different electrolytes under 25 mA g⁻¹. (b) Comparison of ICE and salt concentration in state-of-art electrolytes for MnHCF. (c) Chronoamperometry measurements to hold K||Al-C cells at 4.3 V for 10 h and (d) corresponding SEM images of tested Al-C electrodes. (e) Rate performances.

Regarding the rate performance, the MnHCF in the DiDBE electrolyte conveys limited capacity at over 200 mA g⁻¹ (**Figure 5.9e**) because of the high viscosity. As expected, the addition of DTD greatly improves the rate capability, enabling a capacity of 80 mAh g⁻¹ at 500 mA g⁻¹, outperforming the EC/DEC electrolytes. Furthermore, DiDBE-D endows MnHCF with stable cycling performance. It demonstrates a

consistently high average CE of more than 98.2% and ensures a stable charge-discharge process without any fluctuation in both CE and capacity for 200 cycles (**Figure 5.10a**). In comparison, the capacity and CE of MnHCF in the EC/DEC electrolyte fluctuate significantly within 200 cycles with an average CE of below 95% (**Figure 5.10b**). We also compare the mean discharging potential, i.e., the voltage value at half discharge capacity, of MnHCF in the two electrolytes. The value gradually increases in DiDBED electrolyte due to reduced polarization (inset of **Figure 5.10a**). It maintains a high value of 3.83 V after activation, compared to ~3.77 V for the EC/DEC (**Figure 5.10c**).

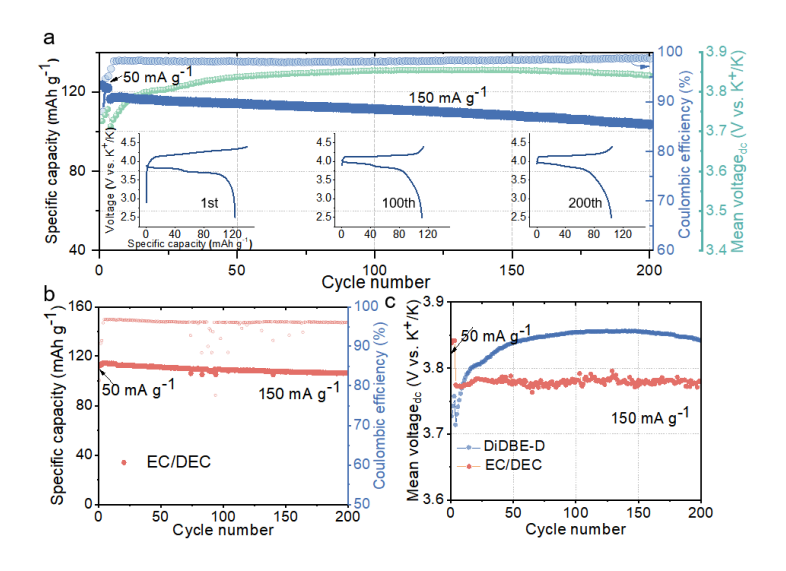


Figure 5.10. (a) Cycling performances of MnHCF in the DiDBE-D electrolyte with corresponding profiles in specific cycles. (b) Cycling performance of the MnHCF electrode in EC/DEC electrolyte. (c) The mean voltage evolution upon cycling in different electrolytes.

Apart from the electrochemical performance, thermal stability is also crucial to the

practical application. Thermogravimetric analysis (TGA) measurement was thus conducted on each electrolyte to assess the thermal stability. Compared to the G2 electrolyte that loses most weight (70wt.%) at below 150 °C (Figure 5.11a), both DiDBE and DiDBE-D electrolytes exhibit much-enhanced stability with over 83 wt.% remaining at 200 °C. This also outperforms the common ester-based electrolyte: the EC/DEC electrolyte starts to lose weight as early as 71 °C. Besides the electrolytes, we also examine the thermal stability of 3rd-cycled MnHCF electrodes in EC/DEC and DiDBE-D electrolytes at 25-250 °C through differential scanning calorimetry (DSC) (Figure 5.11b). A broad exothermic peak with 141 J g⁻¹ is found from 75-150 °C for MnHCF cycled in the EC/DEC electrolyte, arising mainly from the CEI degradation ¹⁹⁹. In contrast, the thermal reaction is calmer for MnHCF cycled in the DiDBE-D electrolyte, characterized by two exothermic peaks with a cumulative thermal energy of 42.5 J g⁻¹, less than one-third of that in the EC/DEC electrolyte.

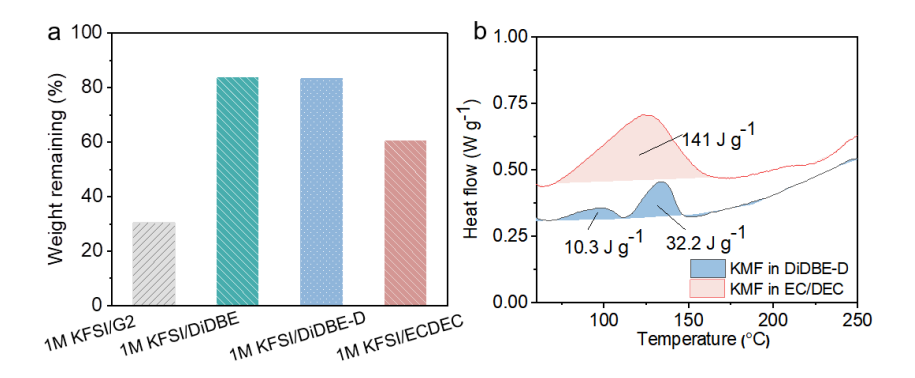


Figure 5.11. (a) Comparison of the remaining weight of different electrolytes at 150 °C based on TGA measurement. (b) DSC curves of cycled MnHCF.

The morphology and structure of cycled MnHCF were examined through high-resolution transmission electron microscopy (HRTEM). Although the bulk parts of cycled MnHCF in both electrolytes retain the original structure with clear lattices of (002) and (022) planes, there is a significant difference in the CEI. A conformal amorphous CEI with a thickness of 3 nm covers the MnHCF particles cycled in the DiDBE-D electrolyte (**Figure 5.12a**). In sharp contrast, for the one cycled in EC/DEC counterpart, homogenous and continuous CEIs are barely observed but it is common to capture unevenly aggregated crystals on the MnHCF surface (**Figure 5.12b**). Based on the inset FFT pattern, these crystals can be assigned to orthorhombic K₂SO₄ with the space group of Pnam (62).

We further use the XPS to probe the chemical composition of the CEIs in the two electrolytes. The prominent C 1s spectra (**Figure 5.12c**) suggest significant amounts of organic species derived from solvent decomposition. A large proportion of C-O is observed in both C 1s and O 1s spectra of electrodes cycled in both electrolytes (**Figure 5.12d**). The C-O bond in EC/DEC is assigned to the potassium ethylene decarbonate²⁰⁰. Instead, the one in DiDBE-D counterpart suggests the presence of PEO-like polymer species^{24, 201} originating from DiDBE decomposition, which features a high flexibility to retain an intact CEI in HRTEM. Furthermore, the ROSO₂- peak related to S-containing organics is outstanding in the S 2p spectrum (**Figure 5.12e**) on the surface

of the DiDBE-D sample, whose intensity is over two times that of the EC/DEC one. The pronounced S-F peak in the F 1s spectrum (**Figure 5.12f**) further confirms more S-containing organic species in the CEI formed in DiDBE-D, which mainly comes from the DTD decomposition. Such a high content of S in CEI is expected to inhibit the Mn²⁺ dissolution of the cathode through complexing them with organic -OSO₂- group²⁰². This is evidenced by the weaker Mn signal on the 150th-cycled separator from inductively coupled plasma-mass spectrometry (**Table 5.3**).

Table 5.3. ICP-MS result of Mn residue proportion at the separator in MnHCF||K cells with DiDBE-D and EC/DEC electrolytes after 150 cycles.

Utilized electrolyte	Mn residue proportion on the separator (mg kg ⁻¹)
1M KFSI/ECDEC	1.18
1M KFSI/DiDBE-D	0.12

5.2.3 Enhanced Stability of Modified Electrolyte against K Anode

The electrolyte chemistry would also greatly impact the stability of the K metal anode. We first evaluate the long-term plating/striping behaviors in K||Al-C cells (**Figure 5.13a**), the stability is poor in the EC/DEC electrolyte and the CE fluctuates severely after only 30 cycles with an average CE of 96.5%, whereas the DiDBE-D electrolyte enables the K||Al-C cell with a high average CE of 98.8% during 120 cycles at 0.5 mA cm⁻²-1 mAh cm⁻². The performances of K||K symmetric cells in different electrolytes

are also assessed (**Figure 5.13b**). Despite the relatively great voltage hysteresis in DiDBE-D at the initial cycles, it undergoes a gradual reduction in voltage polarization and a steady cycling for over 700 h. In striking contrast, a noticeable surge in voltage hysteresis appears from 200 h for the DiDBE electrolyte (**Figure 5.13c**), suggesting the positive effect of the DTD additive on the K metal anode. The K||K cell in EC/DEC witnesses a continuous increase in voltage polarization and fails with a lifespan of only 100 h (**Figure 5.13b**). It is worth mentioning the DTD addition in the EC/DEC electrolyte does not bring a positive effect (**Figure 5.13d**), and the synergistic effect could only be realized between the DiDBE and DTD.

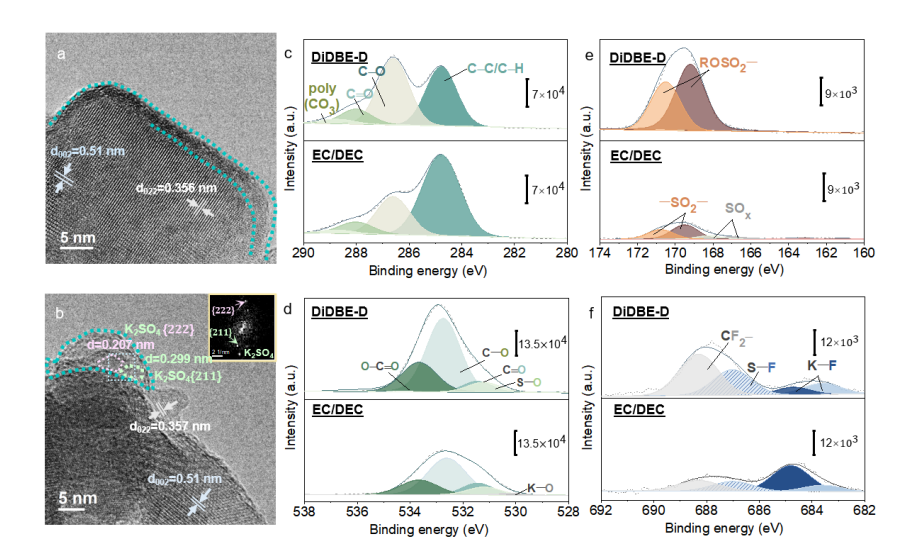


Figure 5.12. HRTEM images of MnHCF cycled in (a) DiDBE-D and (b) EC/DEC electrolyte with corresponding FFT in the selected square area. XPS spectra of (c) C 1s, (d) O 1s, (e) S 2p, and (f) F 1s.

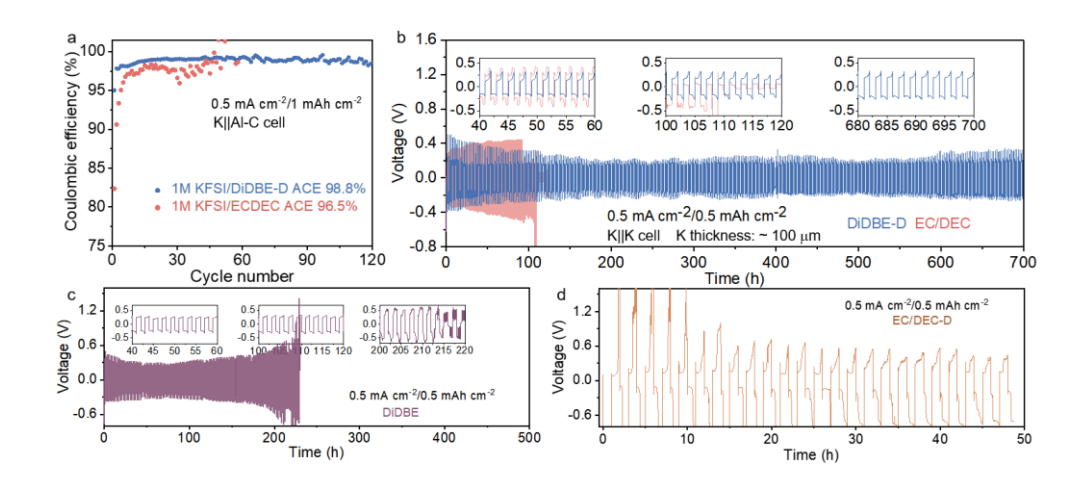


Figure 5.13. (a) Long-term CE tests of K||Al-C cells. Cycling performances of K||K cells at 0.5 mA cm⁻² and 0.5 mAh cm⁻² in (b) DiDBE-D and EC/DEC, (c) DiDBE, and (d) EC/DEC-D electrolytes.

The morphologies of plated K were captured through atomic force microscopy (AFM) in the Ar-filled glove box (**Figure 5.14**). R_a is the arithmetic mean of the observed surface height departure from the mean plane in absolute terms, representing the surface roughness of plated K. To guarantee the data credibility, three areas of about $100 \, \mu m^2$ without any overlap were selected for each sample for R_a calculation. R_a of the deposition surface reduces in the order of EC/DEC, DiDBE, and DiDBE-D electrolyte from 124, 117 to 71 nm, which can also be reflected by the flatter surface of plated K in DiDBE-D electrolyte compared to the irregular chunks-rich surface in EC/DEC electrolyte (**Figure 5.14a-c**). The detailed surface changes in height are visualized in **Figure 5.14d-f**. In contrast to the significant fluctuation within $\pm 300 \, \text{nm}$ in the EC/DEC electrolyte, a smoother K plating surface with $\pm 150 \, \text{nm}$ height change is

generated in the DiDBE-D electrolyte, accounting for the longer cyclic life of K||K cells.

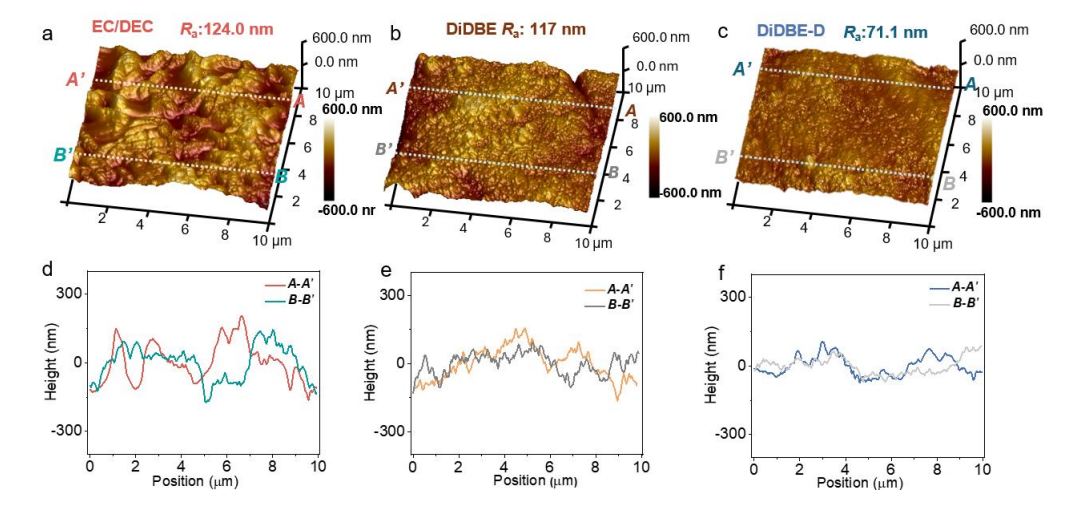


Figure 5.14. (a-c) Three-dimensional 10th-plated K topographic images in different electrolytes from AFM. (d-f) Corresponding sectional height curves of plated K on Al-C electrode.

To explore the underlying mechanism, we measure the mechanical properties of SEI on the K anode through the AFM-based nanoindentation test⁶² (**Figure 5.15**). For each sample, over 70 testing positions were tested for calculating Young's modulus E, elastic strain limit ε_Y , and the maximum energy of elastic deformation $U(U \propto E \cdot \varepsilon_Y^5)^{143}$. In the first step (**Figure 5.15a**), a maximum force of 30 nN was set to obtain as much force-displacement data as possible within the elastic region of SEI with the reversible deformation. For the second step (**Figure 5.15b**), 900 nN was set as the maximum force to deform the SEI and collect the elastic strain limit of SEIs. The SEI generated in the EC/DEC electrolyte (**Figure 5.15c-d**) possesses a high E of 873 MPa but a low ε_Y of 0.255. In sharp contrast, the DiDBE-D electrolyte induces an SEI with a higher ε_Y of

0.306 and a lower E of 538 MPa. The U value, which combines the effect of Young's modulus and maximum elastic strain, is adopted to predict the stability of SEI during repeated K plating/stripping. It shows a higher value of 58.3 pJ in the as-developed electrolyte than 34.7 pJ for the benchmark carbonate counterpart (**Figure 5.15d**).

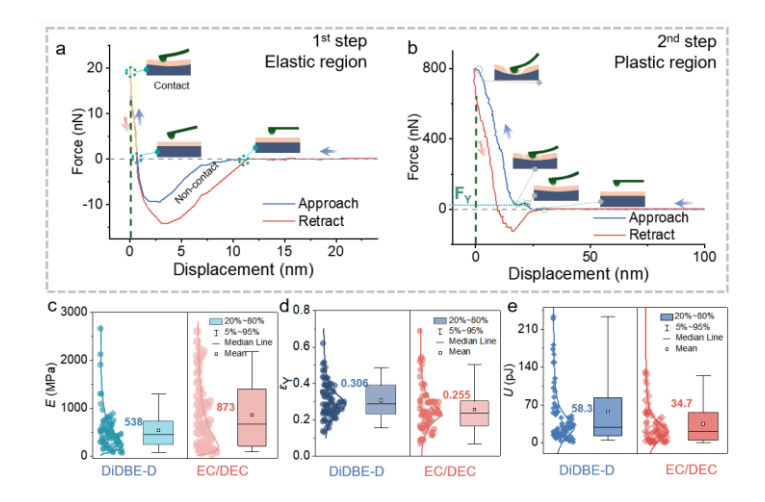


Figure 5.15. Typical force-displacement curves at different regions for (a) the elastic region obtained with a small force of less than 30 nN and curves for (b) the plastic region obtained with a larger load, about 900 nN. Box charts with the distribution curve for (c) Young's modulus E, (d) elastic strain limit ε_Y , and (e) U values of elastic deformation of more than 70 testing positions.

XPS measurements in different depths were performed to explore the compositional reasons for the distinct mechanical response. There is not much difference in the overall C content (**Figure 5.16**) but with distinct compositions. Similar to the CEIs, a large proportion of the C-O bond corresponding to the PEO-like [CH₂CH₂O]_n organic components¹⁸² is presented in the DiDBE-D sample. They are

generated by the DiDBE reduction, where the possible formation mechanism is proposed in **Figure 5.17**.

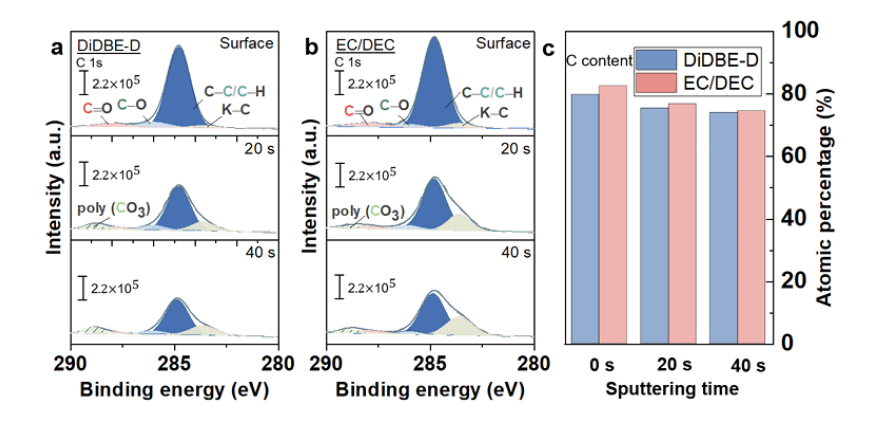


Figure 5.16. C 1s XPS spectra of plated K anode cycled in (a) DiDBE-D and (b) EC/DEC electrolytes. (c) C atomic percentage of different samples.



Figure 5.17. Decomposition mechanism of DiDBE. Reproduced with permission¹⁴¹. Copyright 2019. Royal of Society Chemistry.

5.18a), indicating they are distributed throughout the SEI. These oligomers possess a high elasticity²⁰³ for realizing outstanding mechanical stability as measured in the nanoindentation test. It is also noticed that the S-O peak dominates in O 1s spectra for the DiDBE-D sample compared to the EC/DEC one (**Figure 5.18b**), which arises from the decomposition of either S-containing solvents or salts. S 2p spectra (**Figure 5.18c-d**) are analyzed to further unveil this component. The presence of the ROSO₂- peak in

the DiDBE-D sample steadily rises with sputtering times and exhibits a significantly greater intensity, indicating more S-containing organic species ROSO₂K in the SEI from the decomposition of DTD²⁰⁴ (**Figure 5.19**). These species with high polarity and ionic conductivity can promote ionic diffusion within SEI²⁰⁵⁻²⁰⁷, which explains the higher I_0 calculated from DiDBE-D Tafel curves.

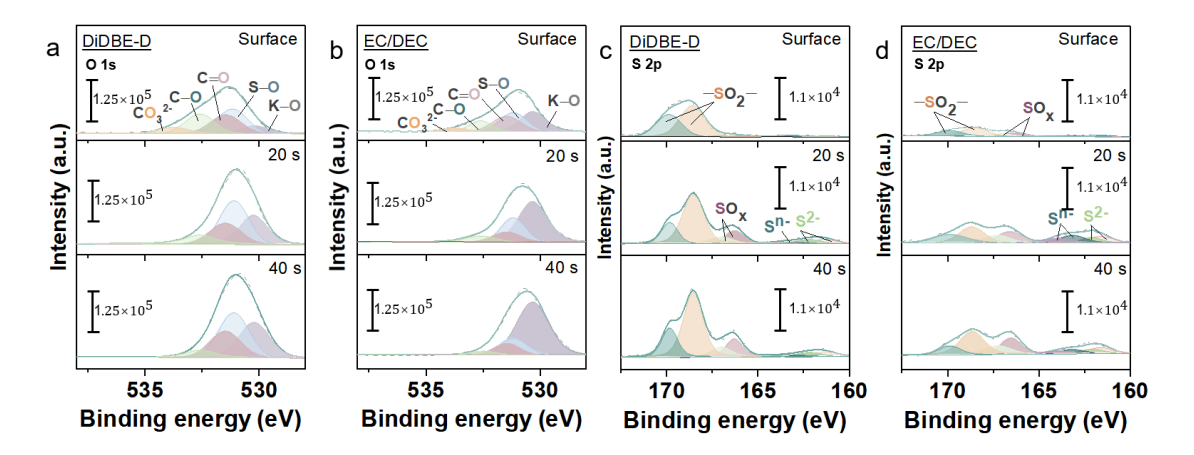


Figure 5.18. (a-b) O 1s spectra and (c-d) S 2p spectra of 10th-plated K on Al-C current collectors in DiDBE-D and EC/DEC electrolytes.

Figure 5.19. Proposed reduction mechanism of DTD. Reproduced with permission²⁰¹. Copyright 2021. Wiley-VCH.

5.2.4 Performance of K||MnHCF Cells Under a Harsh Condition

Having confirmed the beneficial impact of DiDBE-D electrolyte on both MnHCF cathode and K anode, we analyze the cycling performance of K||MnHCF cells under a more challenging condition with a negative/positive (N/P) capacity ratio of 4 (**Figure**

5.20a). The CE of the cell in the EC/DEC electrolyte continuously fluctuates at around 80%, and its capacity suddenly degrades after 150 cycles (**Figure 5.20b**). Encouragingly, the K||MnHCF cell in the DiDBE-D electrolyte demonstrates a high ICE of 90.9% and delivers a steady capacity in a longer lifespan of 200 cycles with a mean voltage of over 3.81 V and ACE of over 99.4%, resulting from the concurrent enhancement in both cathode and anode.

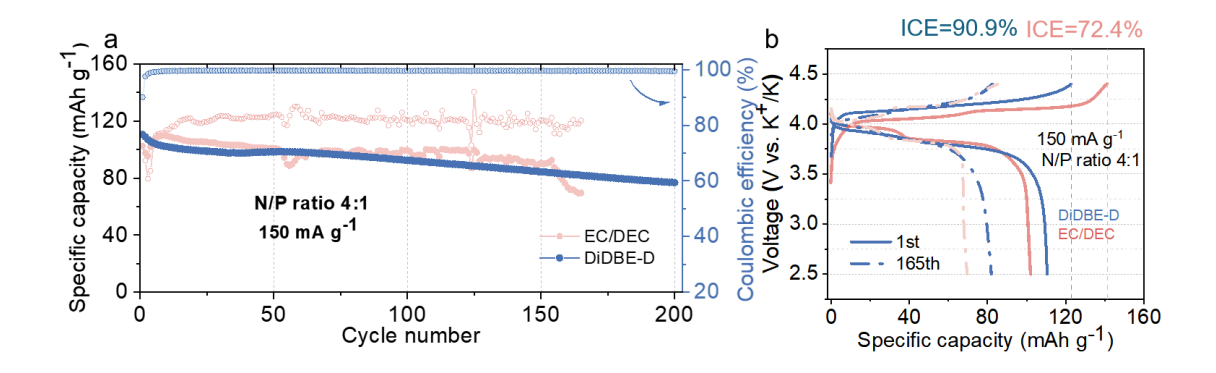


Figure 5.20. (a) The cycling performance of K||MnHCF cell with an N/P ratio of 4 in different electrolytes with (b) corresponding voltage profiles at the first cycle and 165th cycle.

5.3 Summary

We demonstrate that extending the terminal alkyl chain of ether could effectively reduce solvent reactivity through the steric hindrance associated with large-sized end groups. Consequently, it weakens the K ion-solvent interaction evidenced by the lower solvent proportion in the K ion solvation shell, which alleviates the solvent decomposition. The oxidative stability could be boosted to 4.6 V through an S-

containing additive, which also suppresses the corrosion of the Al-C current collector and Mn dissolution from the cathode. Delightedly, such an electrolyte benefits the mechanically stable SEI on the K metal anode as well. The decomposition of DiDBE gives rise to the formation of oligomers in the SEI, which are characteristic of high elasticity. Besides, the presence of S-rich species in SEI contributes to fast kinetics for homogeneous K deposition, explaining the higher Coulombic efficiency and longer cyclic life of K metal anode in DiDBE-D electrolyte. The cumulative ameliorations on the cathode and anode interphases allow the stable cycling of MnHCF||K cell with a limited K excess. This study provides an effective strategy to design the non-fluorinated ether electrolyte toward high-potential PMBs by modulating the solvation structure and the resulting interphases.

Chapter 6. Conclusion and Future Plan

6.1 Conclusion

PIBs have drawn much attention recently owing to their low K redox potential and abundant resources. However, the related research into both electrodes and electrolytes is still in its infancy with some vague underlying mechanisms. The unstable interphases also hamper the development of PIBs. This thesis is committed to boosting the interfacial stability at both the anode and cathode. The hard carbon anodes are firstly explored by clarifying the charge storage mechanism at the low voltage, followed by boosting the kinetics through regulation of the interfacial behavior. The carbon material is also applied as a coating on the Al current collector to tailor the SEI on the K metal anode. Lastly, electrolyte engineering is conducted to concurrently stabilize SEI and CEI for realizing high-energy potassium full cells. Three major findings are concluded as follows:

(1) We explored the K ion storage performance and the associated charge storage mechanism in biomass-derived hard carbon. It is found that the pore filling of K ions is partly responsible for the capacity of the low-voltage region, evidenced by the presence of quasi-potassium nanoclusters after fully discharging. The slow kinetics could be promoted by optimizing cycling protocol and electrolyte formulations.

To boost the unsatisfactory rate performance of hard carbons, we developed a

cyclic ether THF with weak K-solvent interaction owing to low polarity and high dipole moment/dielectric constant (μ/ε) ratio. Such weak solvent does not only avoid the cointercalation with K ion that occurs in the most widely investigated DME electrolyte but enhances the K ion insertion owing to the facile de-solvation process. Most importantly, an inorganic-rich SEI from more FSI⁻-decomposition benefits the charge transfer. Consequently, the CNFs show superior rate capability (143 mAh g⁻¹ at 1.5 A g⁻¹) and cyclic performance in the THF-based electrolyte even at 0 °C.

- (2) We applied the carbon-based coating to manipulate the SEI on K metal anodes by altering the extent of the electrolyte decomposition. A dual-modification approach consisting of CNF and Ni (CNFNi@Al) is adopted to achieve advanced potassium metal anodes through a synergy between stable interphase and nucleation. Firstly, the as-designed current collector features a reduced Fermi level due to an elevated work function, inducing the formation of a thin inorganic-rich SEI with superior mechanical properties to avoid SEI fracture during volume expansion. Secondly, nickel species endow the current collector with a high affinity towards K, promoting the nucleation and planar growth behavior of K embryos. As a result, an anode-free MnHCF||CNFNi@Al cell can be realized with 89% capacity sustained after 50 cycles at 100 mA g⁻¹.
- (3) We developed a novel electrolyte by extending the terminal alkyl chain of ether to

reduce solvent reactivity through the steric hindrance and alleviate the solvent decomposition at high voltages. The oxidative stability can be boosted to 4.6 V with the assistance of an S-containing additive, which also suppresses the corrosion of the Al-C current collector and Mn dissolution from the cathode. Delightedly, such an electrolyte benefits the mechanically stable SEI with high elasticity on the K metal anode as well. The cumulative ameliorations on the cathode and anode interphases allow the stable cycling of MnHCF||K cell with a limited K excess.

6.2 Future Plan

Upon completion of this thesis, there are still great obstacles in PIBs in both the electrodes and electrolytes. Two potential research directions are proposed as follows:

(1) Improving the performance of PIBs at a wide temperature. Wide-temperature PIBs

have been rarely reported, due possibly to the slow K ion transfer kinetics at the interface and within the electrodes. While novel electrodes are being intensively explored, electrolyte engineering is also crucial. Solvents with a larger liquid range (large difference between the melting point and boiling point) would help retain a reasonable ionic conductivity at a super low temperature and thermal stability at a high temperature. Apart from the electrolyte itself, the resulting SEI/CEIs play vital roles in the stability and kinetics. Simutaneously building SEI/CEI at a wide temperature remains challenging.

(2) Pursuing high-energy cathode materials. Note that the iron-based Prussian blue FeHCF utilized in Chapter 4 exhibits relatively great cyclic stability with an average discharging potential of 3.5 V but delivers only about 60 mAh g⁻¹ capacity. The manganese-based Prussian white (MnHCF) in Chapter 5 displays a higher capacity of 120 mAh g⁻¹ with an elevated potential of 3.8 V while suffering from poor cycling performance. Other high-voltage polyanion type KVPF witnesses a poor rate performance due to limited electric conductivity. In addition, it requires a super-high charging voltage of up to 5 V, which surpasses the oxidative stability of most electrolytes. Another issue that has been largely ignored is the low density of these polyanion and Prussian cathodes compared to layered oxides, which may cause a penalty on the volumetric energy density of PIBs.

References

- 1. Kubota, K.; Dahbi, M.; Hosaka, T.; Kumakura, S.; Komaba, S. Towards K-Ion and Na-Ion Batteries as "Beyond Li-Ion". *The Chemical Record* **2018**, *18*, 459-479.
- 2. Hosaka, T.; Kubota, K.; Hameed, A. S.; Komaba, S. Research Development on K-Ion Batteries. *Chemical Reviews* **2020**, *120*, 6358-6466.
- 3. Hironaka, Y.; Kubota, K.; Komaba, S. P2- and P3-K_xCoO₂ as an Electrochemical Potassium Intercalation Host. *Chemical Communications* **2017**, *53*, 3693-3696.
- 4. Weng, J.; Duan, J.; Sun, C.; Liu, P.; Li, A.; Zhou, P.; Zhou, J. Construction of Hierarchical K_{0.7}Mn_{0.7}Mg_{0.3}O₂ Microparticles as High Capacity & Long Cycle Life Cathode Materials for Low-Cost Potassium-Ion Batteries. *Chemical Engineering Journal* **2020**, *392*, 123649.
- 5. Liu, Z.; Wang, J.; Lu, B. Plum Pudding Model Inspired KVPO₄F@3DC as High-Voltage and Hyperstable Cathode for Potassium Ion Batteries. *Science Bulletin* **2020**, 65, 1242-1251.
- 6. Lin, X.; Huang, J.; Tan, H.; Huang, J.; Zhang, B. K₃V₂(PO₄)₂F₃ as a Robust Cathode for Potassium-Ion Batteries. *Energy Storage Materials* **2019**, *16*, 97-101.
- 7. Kim, H.; Seo, D.-H.; Urban, A.; Lee, J.; Kwon, D.-H.; Bo, S.-H.; Shi, T.; Papp, J. K.; McCloskey, B. D.; Ceder, G. Stoichiometric Layered Potassium Transition Metal Oxide for Rechargeable Potassium Batteries. *Chemistry of Materials* **2018**, *30*, 6532-6539.

- 8. Deng, L.; Qu, J.; Niu, X.; Liu, J.; Zhang, J.; Hong, Y.; Feng, M.; Wang, J.; Hu, M.; Zeng, L.; et al. Defect-Free Potassium Manganese Hexacyanoferrate Cathode Material for High-Performance Potassium-Ion Batteries. *Nature Communications* **2021**, *12*, 2167.
- 9. Gao, Y.; Li, W.; Ou, B.; Zhang, S.; Wang, H.; Hu, J.; Kang, F.; Zhai, D. A Dilute Fluorinated Phosphate Electrolyte Enables 4.9 V-Class Potassium Ion Full Batteries. *Advanced Functional Materials* **2023**, *33*, 2305829.
- 10. Tian, Y.; Zeng, G.; Rutt, A.; Shi, T.; Kim, H.; Wang, J.; Koettgen, J.; Sun, Y.; Ouyang,
 B.; Chen, T.; et al. Promises and Challenges of Next-Generation "Beyond Li-Ion"
 Batteries for Electric Vehicles and Grid Decarbonization. *Chemical Reviews* 2021, 121, 1623-1669.
- 11. Zhao, S.; Guo, Z.; Yan, K.; Guo, X.; Wan, S.; He, F.; Sun, B.; Wang, G. The Rise of Prussian Blue Analogs: Challenges and Opportunities for High-Performance Cathode Materials in Potassium-Ion Batteries. *Small Structures* **2020**, *2*, 2000054.
- 12. Xue, L. G.; Li, Y. T.; Gao, H. C.; Zhou, W. D.; Lu, X. J.; Kaveevivitchai, W.; Manthiram, A.; Goodenough, J. B. Low-Cost High-Energy Potassium Cathode. *Journal of the American Chemical Society* **2017**, *139*, 2164-2167.
- 13. Zhang, J.; Deng, L.; Feng, M.; Zeng, L.; Hu, M.; Zhu, Y. Low-Defect K₂Mn[Fe(CN)₆]-Reduced Graphene Oxide Composite for High-Performance

Potassium-Ion Batteries. Chemical Communications 2021, 57, 8632-8635.

- 14. Qin, M.; Ren, W.; Meng, J.; Wang, X.; Yao, X.; Ke, Y.; Li, Q.; Mai, L. Realizing Superior Prussian Blue Positive Electrode for Potassium Storage Via Ultrathin Nanosheet Assembly. *ACS Sustainable Chemistry & Engineering* **2019**, *7*, 11564-11570.

 15. Huang, B.; Liu, Y.; Lu, Z.; Shen, M.; Zhou, J.; Ren, J.; Li, X.; Liao, S. Prussian Blue [K₂FeFe(CN)₆] Doped with Nickel as a Superior Cathode: An Efficient Strategy to Enhance Potassium Storage Performance. *ACS Sustainable Chemistry & Engineering* **2019**, *7*, 16659-16667.
- 16. Desai, P.; Forero-Saboya, J.; Meunier, V.; Rousse, G.; Deschamps, M.; Abakumov, A. M.; Tarascon, J.-M.; Mariyappan, S. Mastering the Synergy between Na₃V₂(PO₄)₂F₃ Electrode and Electrolyte: A Must for Na-Ion Cells. *Energy Storage Materials* **2023**, *57*, 102-117.
- 17. Wernert, R.; Nguyen, L. H. B.; Iadecola, A.; Weill, F.; Fauth, F.; Monconduit, L.; Carlier, D.; Croguennec, L. Self-Discharge Mechanism of High-Voltage KVPO₄F for K-Ion Batteries. *ACS Applied Energy Materials* **2022**, *5*, 14913-14921.
- 18. Saurel, D.; Orayech, B.; Xiao, B.; Carriazo, D.; Li, X.; Rojo, T. From Charge Storage Mechanism to Performance: A Roadmap toward High Specific Energy Sodium-Ion Batteries through Carbon Anode Optimization. *Advanced Energy Materials* **2018**, *8*, 1703268.

- 19. Mizutani, Y.; Abe, T.; Ikeda, K.; Ihara, E.; Asano, M.; Harada, T.; Inaba, M.; Ogumi,
- Z. Graphite Intercalation Compounds Prepared in Solutions of Alkali Metals in 2-Methyltetrahydrofuran and 2,5-Dimethyltetrahydrofuran. *Carbon* **1997**, *35*, 61-65.
- 20. Jian, Z.; Luo, W.; Ji, X. Carbon Electrodes for K-Ion Batteries. *Journal of the American Chemical Society* **2015**, *137*, 11566-11569.
- 21. Pendashteh, A.; Orayech, B.; Suhard, H.; Jauregui, M.; Ajuria, J.; Silván, B.; Clarke, S.; Bonilla, F.; Saurel, D. Boosting the Performance of Soft Carbon Negative Electrode for High Power Na-Ion Batteries and Li-Ion Capacitors through a Rational Strategy of Structural and Morphological Manipulation. *Energy Storage Materials* 2022, 46, 417-430.
- 22. Loaiza, L. C.; Monconduit, L.; Seznec, V. Si and Ge-Based Anode Materials for Li-, Na-, and K-Ion Batteries: A Perspective from Structure to Electrochemical Mechanism. *Small* **2020**, *16*, 1905260.
- 23. Ramireddy, T.; Kali, R.; Jangid, M. K.; Srihari, V.; Poswal, H. K.; Mukhopadhyay, A. Insights into Electrochemical Behavior, Phase Evolution and Stability of Sn Upon K-Alloying/De-Alloying Via in Situ Studies. *Journal of The Electrochemical Society* **2017**, *164*, A2360.
- 24. Du, X.; Gao, Y.; Zhang, B. Building Elastic Solid Electrolyte Interphases for Stabilizing Microsized Antimony Anodes in Potassium Ion Batteries. *Advanced*

Functional Materials **2021**, *31*, 2102562.

- 25. Huang, J.; Lin, X.; Tan, H.; Zhang, B. Bismuth Microparticles as Advanced Anodes for Potassium-Ion Battery. *Advanced Energy Materials* **2018**, *8*, 1703496.
- 26. Cui, J.; Yao, S.; Ihsan-Ul-Haq, M.; Mubarak, N.; Wang, M.; Wu, J.; Kim, J.-K. Rational Exploration of Conversion-Alloying Reaction Based Anodes for High-Performance K-Ion Batteries. *ACS Materials Letters* **2021**, *3*, 406-413.
- 27. Hu, J.; Wang, H.; Wang, S.; Lei, Y.; Qin, L.; Li, X.; Zhai, D.; Li, B.; Kang, F. Electrochemical Deposition Mechanism of Sodium and Potassium. *Energy Storage Materials* **2021**, *36*, 91-98.
- 28. Wang, H.; Zhai, D.; Kang, F. Solid Electrolyte Interphase (SEI) in Potassium Ion Batteries. *Energy & Environmental Science* **2020**, *13*, 4583-4608.
- 29. Chen, Z.; Wang, L.; Zheng, J.; Huang, Y.; Huang, H.; Li, C.; Shao, Y.; Wu, X.; Rui, X.; Tao, X.; et al. Unraveling the Nucleation and Growth Mechanism of Potassium Metal on 3D Skeletons for Dendrite-Free Potassium Metal Batteries. *ACS Nano* **2024**, *18*, 8496-8510.
- 30. Feng, Y.; Rao, A. M.; Zhou, J.; Lu, B. Selective Potassium Deposition Enables Dendrite-Resistant Anodes for Ultrastable Potassium-Metal Batteries. *Advanced Materials* **2023**, *35*, 2300886.
- 31. Liu, P.; Hao, H.; Singla, A.; Vishnugopi, B. S.; Watt, J.; Mukherjee, P. P.; Mitlin, D.

- Alumina Stabilized SEI and CEI in Potassium Metal Batteries. *Angewandte Chemie International Edition* **2024**, *63*, e202402214.
- 32. Yang, H.; He, F.; Li, M.; Huang, F.; Chen, Z.; Shi, P.; Liu, F.; Jiang, Y.; He, L.; Gu, M.; et al. Design Principles of Sodium/Potassium Protection Layer for High-Power High-Energy Sodium/Potassium-Metal Batteries in Carbonate Electrolytes: A Case Study of Na₂Te/K₂Te. *Advanced Materials* **2021**, *33*, 2106353.
- 33. Wang, H.; Hu, J.; Dong, J.; Lau, K. C.; Qin, L.; Lei, Y.; Li, B.; Zhai, D.; Wu, Y.; Kang, F. Artificial Solid-Electrolyte Interphase Enabled High-Capacity and Stable Cycling Potassium Metal Batteries. *Advanced Energy Materials* **2019**, *9*, 1902697.
- 34. Lei, Y.; Chen, M.; Li, Y.; Zhang, W.; Zhao, D.; Zhu, Q. Dendrite-Free Potassium Metal Anode Induced by in-Situ Phase Transitions of MoS₂. *Materials Today Physics* **2023**, *35*, 101141.
- 35. Wang, S.; Yan, Y.; Xiong, D.; Li, G.; Wang, Y.; Chen, F.; Chen, S.; Tian, B.; Shi, Y. Towards Dendrite-Free Potassium-Metal Batteries: Rational Design of a Multifunctional 3D Polyvinyl Alcohol-Borax Layer. *Angewandte Chemie International Edition* **2021**, *60*, 25122-25127.
- 36. Li, S.; Zhu, H.; Gu, C.; Ma, F.; Zhong, W.; Liu, M.; Zhang, H.; Zeng, Z.; Cheng, S.; Xie, J. Customized Electrolyte and Host Structures Enabling High-Energy-Density Anode-Free Potassium–Metal Batteries. *ACS Energy Letters* **2023**, *8*, 3467-3475.

- 37. Fan, L.; Xie, H.; Hu, Y.; Caixiang, Z.; Rao, A. M.; Zhou, J.; Lu, B. A Tailored Electrolyte for Safe and Durable Potassium Ion Batteries. *Energy & Environmental Science* **2023**, *16*, 305-315.
- 38. Yu, Z.; Fan, K.; Liu, Q.; Wang, D.; Chen, C.; Zhu, Y.; Huang, H.; Zhang, B. Designing Electrolytes with Steric Hindrance and Film-Forming Booster for High-Voltage Potassium Metal Batteries. *Advanced Functional Materials* **2024**, *34*, 2315446.

 39. Hou, Z.; Gao, Y.; Zhou, R.; Zhang, B. Unraveling the Rate-Dependent Stability of Metal Anodes and Its Implication in Designing Cycling Protocol. *Advanced Functional Materials* **2022**, *32*, 2107584.
- 40. Li, S.; Zhu, H.; Liu, Y.; Han, Z.; Peng, L.; Li, S.; Yu, C.; Cheng, S.; Xie, J. Codoped Porous Carbon Nanofibres as a Potassium Metal Host for Nonaqueous K-Ion Batteries.

 Nature Communications 2022, 13, 4911.
- 41. Zhou, R.; Tan, H.; Gao, Y.; Hou, Z.; Du, X.; Zhang, B. Constructing Resilient Solid Electrolyte Interphases on Carbon Nanofiber Film for Advanced Potassium Metal Anodes. *Carbon* **2022**, *186*, 141-149.
- 42. Chen, X.; Bai, Y.-K.; Shen, X.; Peng, H.-J.; Zhang, Q. Sodiophilicity/Potassiophilicity Chemistry in Sodium/Potassium Metal Anodes.

 Journal of Energy Chemistry 2020, 51, 1-6.
- 43. Ponrouch, A.; Marchante, E.; Courty, M.; Tarascon, J.-M.; Palacín, M. R. In Search

- of an Optimized Electrolyte for Na-Ion Batteries. *Energy & Environmental Science* **2012**, *5*, 8572-8583.
- 44. Wang, T.; He, X.; Zhou, M.; Ning, J.; Cao, S.; Chen, M.; Li, H.; Wang, W.; Wang, K.; Jiang, K. In Situ Ions Induced Formation of KF-Rich SEI Layers toward Ultrastable Life of Potassium-Ion Batteries. *Advanced Materials* **2024**, *36*, 2401943.
- 45. Maider, Z.; Javier, C.-G.; Michal, L.; Henry, A.; Boyan, I.; Thomas, J. S. S.; Stefano, P.; Elizabeth, C.-M. Could Potassium-Ion Batteries Become a Competitive Technology? Energy Materials 2023, 3, 300046.
- 46. Tan, H.; Zhai, D.; Kang, F.; Zhang, B. Synergistic PF₆⁻ and FSI⁻ Intercalation Enables Stable Graphite Cathode for Potassium-Based Dual Ion Battery. *Carbon* **2021**, *178*, 363-370.
- 47. Zhu, D.; Ren, Y.; Yu, Y.; Zhang, L.; Wan, Y.; Wang, H.; Gao, W.; Han, B.; Zhang, L. Flame-Retardant Additive/Co-Solvent Contained in Organic Solution for Safe Second Batteries: A Review. *ChemElectroChem* **2023**, *10*, e202300009.
- 48. Wang, X.; Yasukawa, E.; Kasuya, S. Nonflammable Trimethyl Phosphate Solvent-Containing Electrolytes for Lithium-Ion Batteries: I. Fundamental Properties. *Journal of The Electrochemical Society* **2001**, *148*, A1058.
- 49. Wen, J.; Fu, H.; Zhang, D.; Ma, X.; Wu, L.; Fan, L.; Yu, X.; Zhou, J.; Lu, B. Nonfluorinated Antisolvents for Ultrastable Potassium-Ion Batteries. *ACS Nano* **2023**,

- *17*, 16135-16146.
- 50. Hosaka, T.; Matsuyama, T.; Kubota, K.; Tatara, R.; Komaba, S. KFSA/glyme Electrolytes for 4 V-Class K-Ion Batteries. *Journal of Materials Chemistry A* **2020**, 8, 23766-23771.
- 51. Yang, F.; Hao, J.; Long, J.; Liu, S.; Zheng, T.; Lie, W.; Chen, J.; Guo, Z. Achieving High-Performance Metal Phosphide Anode for Potassium Ion Batteries Via Concentrated Electrolyte Chemistry. *Advanced Energy Materials* **2021**, *11*, 2003346.
- 52. Ma, X.; Zhang, D.; Wen, J.; Fan, L.; Rao, A. M.; Lu, B. Sustainable Electrolytes: Design Principles and Recent Advances. *Chemistry* **2024**, *30*, e202400332.
- 53. Wang, D.; Du, X.; Zhang, B. Solvent Molecular Design to Regulate the Intercalation Behavior in Ether Electrolyte for Stable Graphite Anodes in Potassium-Ion Batteries.

 Small Structures 2022, 3, 2200078.
- 54. Hu, Y.; Fu, H.; Geng, Y.; Yang, X.; Fan, L.; Zhou, J.; Lu, B. Chloro-Functionalized Ether-Based Electrolyte for High-Voltage and Stable Potassium-Ion Batteries.

 *Angewandte Chemie International Edition 2024, 63, e202403269.
- 55. Zhang, F.; Wang, X.; Wu, M.; Yang, A.; Li, Y.; Man, M.; Li, Y.; Guo, J. Weakly Solvated Electrolyte Driven Anion Interface Chemistry for Potassium Batteries/Hybrid Capacitors. *ACS Energy Letters* **2023**, *8*, 4895-4902.
- 56. Yao, Y. X.; Chen, X.; Yan, C.; Zhang, X. Q.; Cai, W. L.; Huang, J. Q.; Zhang, Q.

- Regulating Interfacial Chemistry in Lithium-Ion Batteries by a Weakly Solvating Electrolyte*. *Angewandte Chemie International Edition* **2021**, *60*, 4090-4097.
- 57. Hosaka, T.; Kubota, K.; Kojima, H.; Komaba, S. Highly Concentrated Electrolyte Solutions for 4 V Class Potassium-Ion Batteries. *Chemical Communications* **2018**, *54*, 8387-8390.
- 58. Liang, H.; Kumar, P.; Ma, Z.; Zhao, F.; Cheng, H.; Xie, H.; Cao, Z.; Cavallo, L.; Li, Q.; Ming, J. Electrolyte Intermolecular Interaction Mediated Nonflammable Potassium-Ion Sulfur Batteries. *ACS Energy Letters* **2024**, *9*, 3536-3546.
- 59. Xu, W.; Wang, H.; Gao, Y.; Wei, Y.; Zhang, H.; Gao, C.; Kang, F.; Zhai, D. A Localized High Concentration Electrolyte for 4 V-Class Potassium Metal Batteries. *Energy Advances* **2022**, *1*, 191-196.
- 60. Zhang, C.; Xu, Y.; Zhou, M.; Liang, L.; Dong, H.; Wu, M.; Yang, Y.; Lei, Y. Potassium Prussian Blue Nanoparticles: A Low-Cost Cathode Material for Potassium-Ion Batteries. *Advanced Functional Materials* **2017**, *27*, 1604307.
- 61. Li, Y.; Lu, Y.; Meng, Q.; Jensen, A. C. S.; Zhang, Q.; Zhang, Q.; Tong, Y.; Qi, Y.; Gu, L.; Titirici, M. M.; et al. Regulating Pore Structure of Hierarchical Porous Waste Cork-Derived Hard Carbon Anode for Enhanced Na Storage Performance. *Advanced Energy Materials* **2019**, *9*, 1902852.
- 62. Gao, Y.; Du, X.; Hou, Z.; Shen, X.; Mai, Y.-W.; Tarascon, J.-M.; Zhang, B.

- Unraveling the Mechanical Origin of Stable Solid Electrolyte Interphase. *Joule* **2021**, 5, 1860-1872.
- 63. Hertz, H. Über Die Berührung Fester Elastischer Körper. *Reine Angew. Mathematik* **1881**, *92*, 156-171.
- 64. Tafel, J. Über Die Polarisation Bei Kathodischer Wasserstoffentwicklung. Zeitschrift für Physikalische Chemie **1905**, 50U, 641-712.
- 65. Plimpton, S. Fast Parallel Algorithms for Short-Range Molecular Dynamics. *Journal of Computational Physics* **1995**, *117*, 1-19.
- 66. Wang, J.; Wolf, R. M.; Caldwell, J. W.; Kollman, P. A.; Case, D. A. Development and Testing of a General Amber Force Field. *Journal of Computational Chemistry* **2004**, *25*, 1157-1174.
- 67. Gouveia, A. S.; Bernardes, C. E.; Tomé, L. C.; Lozinskaya, E. I.; Vygodskii, Y. S.; Shaplov, A. S.; Lopes, J. N. C.; Marrucho, I. M. Ionic Liquids with Anions Based on Fluorosulfonyl Derivatives: From Asymmetrical Substitutions to a Consistent Force Field Model. *Physical Chemistry Chemical Physics* **2017**, *19*, 29617-29624.
- 68. Martinez, L.; Andrade, R.; Birgin, E. G.; Martinez, J. M. Packmol: A Package for Building Initial Configurations for Molecular Dynamics Simulations. *Journal of Computational Chemistry* **2009**, *30*, 2157-2164.
- 69. Jewett, A. I.; Stelter, D.; Lambert, J.; Saladi, S. M.; Roscioni, O. M.; Ricci, M.;

- Autin, L.; Maritan, M.; Bashusqeh, S. M.; Keyes, T.; et al. Moltemplate: A Tool for Coarse-Grained Modeling of Complex Biological Matter and Soft Condensed Matter Physics. *Journal of Molecular Biology* **2021**, *433*, 166841.
- 70. Nosé, S. A Unified Formulation of the Constant Temperature Molecular Dynamics Methods. *The Journal of Chemical Physics* **1984**, *81*, 511-519.
- 71. Hoover, W. G. Canonical Dynamics: Equilibrium Phase-Space Distributions. *Physical Review A, General Physics* **1985**, *31*, 1695-1697.
- 72. Berendsen, H. J.; Postma, J. v.; Van Gunsteren, W. F.; DiNola, A.; Haak, J. R. Molecular Dynamics with Coupling to an External Bath. *The Journal of Chemical Physics* **1984**, *81*, 3684-3690.
- 73. Momma, K.; Izumi, F. Vesta 3 for Three-Dimensional Visualization of Crystal, Volumetric and Morphology Data. *Journal of Applied Crystallography* **2011**, *44*, 1272-1276.
- 74. Humphrey, W.; Dalke, A.; Schulten, K. VMD: Visual Molecular Dynamics. *Journal of Molecular Graphics* **1996**, *14*, 33-38.
- 75. Neese, F. The ORCA Program System. Wiley Interdisciplinary Reviews: Computational Molecular Science 2012, 2, 73-78.
- 76. Grimme, S.; Antony, J.; Ehrlich, S.; Krieg, H. A Consistent and Accurate Ab Initio
 Parametrization of Density Functional Dispersion Correction (DFT-D) for the 94

Elements H-Pu. The Journal of Chemical Physics 2010, 132, 154104.

77. Grimme, S.; Ehrlich, S.; Goerigk, L. Effect of the Damping Function in Dispersion Corrected Density Functional Theory. *Journal of Computational Chemistry* **2011**, *32*, 1456-1465.

78. Krishnan, R.; Binkley, J. S.; Seeger, R.; Pople, J. A. Self-Consistent Molecular Orbital Methods. XX. A Basis Set for Correlated Wave Functions. *The Journal of Chemical Physics* **1980**, *72*, 650-654.

79. Weigend, F.; Ahlrichs, R. Balanced Basis Sets of Split Valence, Triple Zeta Valence and Quadruple Zeta Valence Quality for H to Rn: Design and Assessment of Accuracy. *Physical Chemistry Chemical Physics* **2005**, *7*, 3297-3305.

80. Barone, V.; Cossi, M. Quantum Calculation of Molecular Energies and Energy Gradients in Solution by a Conductor Solvent Model. *The Journal of Physical Chemistry A* **1998**, *102*, 1995-2001.

81. Chi, C.; Liu, Z.; Lu, X.; Meng, Y.; Huangfu, C.; Yan, Y.; Qiu, Z.; Qi, B.; Wang, G.; Pang, H.; et al. Balance of Sulfur Doping Content and Conductivity of Hard Carbon Anode for High-Performance K-Ion Storage. *Energy Storage Materials* **2023**, *54*, 668-679.

82. Li, H.; Cheng, Z.; Zhang, Q.; Natan, A.; Yang, Y.; Cao, D.; Zhu, H. Bacterial-Derived, Compressible, and Hierarchical Porous Carbon for High-Performance

Potassium-Ion Batteries. Nano Letters 2018, 18, 7407-7413.

- 83. Prabakar, S. J. R.; Han, S. C.; Park, C.; Bhairuba, I. A.; Reece, M. J.; Sohn, K.-S.; Pyo, M. Spontaneous Formation of Interwoven Porous Channels in Hard-Wood-Based Hard-Carbon for High-Performance Anodes in Potassium-Ion Batteries. *Journal of The Electrochemical Society* **2017**, *164*, A2012.
- 84. Li, Q.; Zhang, J.; Zhong, L.; Geng, F.; Tao, Y.; Geng, C.; Li, S.; Hu, B.; Yang, Q.-H. Unraveling the Key Atomic Interactions in Determining the Varying Li/Na/K Storage Mechanism of Hard Carbon Anodes. *Advanced Energy Materials* **2022**, *12*, 2201734.
- 85. Zhao, L.-F.; Hu, Z.; Lai, W.-H.; Tao, Y.; Peng, J.; Miao, Z.-C.; Wang, Y.-X.; Chou, S.-L.; Liu, H.-K.; Dou, S.-X. Hard Carbon Anodes: Fundamental Understanding and Commercial Perspectives for Na-Ion Batteries Beyond Li-Ion and K-Ion Counterparts.

 Advanced Energy Materials 2021, 11, 2002704.
- 86. Nagmani; Tyagi, A.; Puravankara, S. Insights into the Diverse Precursor-Based Micro-Spherical Hard Carbons as Anode Materials for Sodium–Ion and Potassium–Ion Batteries. *Materials Advances* **2022**, *3*, 810-836.
- 87. Zhao, J.; Zou, X.; Zhu, Y.; Xu, Y.; Wang, C. Electrochemical Intercalation of Potassium into Graphite. *Advanced Functional Materials* **2016**, *26*, 8103-8110.
- 88. Debye, P.; Jr., H. R. A.; Brumberger, H. Scattering by an Inhomogeneous Solid. II.

The Correlation Function and Its Application. *Journal of Applied Physics* **1957**, *28*, 679-683.

- 89. Yuan, M.; Cao, B.; Liu, H.; Meng, C.; Wu, J.; Zhang, S.; Li, A.; Chen, X.; Song, H. Sodium Storage Mechanism of Nongraphitic Carbons: A General Model and the Function of Accessible Closed Pores. *Chemistry of Materials* **2022**, *34*, 3489-3500.

 90. Fan, L.; Ma, R.; Zhang, Q.; Jia, X.; Lu, B. Graphite Anode for a Potassium-Ion Battery with Unprecedented Performance. *Angewandte Chemie International Edition in English* **2019**, *58*, 10500-10505.
- 91. Sun, Y.; Xiao, H.; Li, H.; He, Y.; Zhang, Y.; Hu, Y.; Ju, Z.; Zhuang, Q.; Cui, Y. Nitrogen/Oxygen Co-Doped Hierarchically Porous Carbon for High-Performance Potassium Storage. *Chemistry A European Journal* **2019**, *25*, 7359-7365.
- 92. Chen, C.; Wang, Z.; Zhang, B.; Miao, L.; Cai, J.; Peng, L.; Huang, Y.; Jiang, J.; Huang, Y.; Zhang, L.; et al. Nitrogen-Rich Hard Carbon as a Highly Durable Anode for High-Power Potassium-Ion Batteries. *Energy Storage Materials* **2017**, *8*, 161-168.
- 93. Tian, S.; Guan, D.; Lu, J.; Zhang, Y.; Liu, T.; Zhao, X.; Yang, C.; Nan, J. Synthesis of the Electrochemically Stable Sulfur-Doped Bamboo Charcoal as the Anode Material of Potassium-Ion Batteries. *Journal of Power Sources* **2020**, *448*, 227572.
- 94. Wu, Z.; Wang, L.; Huang, J.; Zou, J.; Chen, S.; Cheng, H.; Jiang, C.; Gao, P.; Niu, X. Loofah-Derived Carbon as an Anode Material for Potassium Ion and Lithium Ion

Batteries. Electrochimica Acta 2019, 306, 446-453.

95. Liu, M.; Jing, D.; Shi, Y.; Zhuang, Q. Superior Potassium Storage in Natural O/N–Doped Hard Carbon Derived from Maple Leaves. *Journal of Materials Science:*Materials in Electronics **2019**, *30*, 8911-8919.

96. Xu, B.; Qi, S.; Li, F.; Peng, X.; Cai, J.; Liang, J.; Ma, J. Cotton-Derived Oxygen/Sulfur Co-Doped Hard Carbon as Advanced Anode Material for Potassium-Ion Batteries. *Chinese Chemical Letters* **2020**, *31*, 217-222.

97. Shan, J.; Wang, J.-j.; Kiekens, P.; Zhao, Y.; Huang, J.-j. Effect of Co-Activation of Petroleum Coke and Artemisia Hedinii on Potassium Loss During Activation and Its Promising Application in Anode Material of Potassium-Ion Batteries. *Solid State Sciences* **2019**, *92*, 96-105.

98. Zhang, Z.; Jia, B.; Liu, L.; Zhao, Y.; Wu, H.; Qin, M.; Han, K.; Wang, W. A.; Xi, K.; Zhang, L.; et al. Hollow Multihole Carbon Bowls: A Stress–Release Structure Design for High-Stability and High-Volumetric-Capacity Potassium-Ion Batteries. *ACS Nano* **2019**, *13*, 11363-11371.

99. Hu, Y.; Fan, L.; Rao, A. M.; Yu, W.; Zhuoma, C.; Feng, Y.; Qin, Z.; Zhou, J.; Lu, B. Cyclic-Anion Salt for High-Voltage Stable Potassium-Metal Batteries. *National Science Review* **2022**, *9*, nwac134.

100. Gu, M.; Rao, A. M.; Zhou, J.; Lu, B. In Situ Formed Uniform and Elastic SEI for

High-Performance Batteries. *Energy & Environmental Science* **2023**, *16*, 1166-1175.

101. Chen, X.; Tian, J.; Li, P.; Fang, Y.; Fang, Y.; Liang, X.; Feng, J.; Dong, J.; Ai, X.; Yang, H.; et al. An Overall Understanding of Sodium Storage Behaviors in Hard Carbons by an "Adsorption-Intercalation/Filling" Hybrid Mechanism. *Advanced Energy Materials* **2022**, 2200886.

102. Alvin, S.; Cahyadi, H. S.; Hwang, J.; Chang, W.; Kwak, S. K.; Kim, J. Revealing the Intercalation Mechanisms of Lithium, Sodium, and Potassium in Hard Carbon.

Advanced Energy Materials 2020, 10, 2000283.

103. Morikawa, Y.; Nishimura, S. i.; Hashimoto, R. i.; Ohnuma, M.; Yamada, A. Mechanism of Sodium Storage in Hard Carbon: An X-Ray Scattering Analysis.

*Advanced Energy Materials 2019, 10, 1903176.

104. Xia, J. L.; Yan, D.; Guo, L. P.; Dong, X. L.; Li, W. C.; Lu, A. H. Hard Carbon Nanosheets with Uniform Ultramicropores and Accessible Functional Groups Showing High Realistic Capacity and Superior Rate Performance for Sodium-Ion Storage.

Advanced Materials 2020, 32, e2000447.

105. Matei Ghimbeu, C.; Górka, J.; Simone, V.; Simonin, L.; Martinet, S.; Vix-Guterl, C. Insights on the Na⁺ Ion Storage Mechanism in Hard Carbon: Discrimination between the Porosity, Surface Functional Groups and Defects. *Nano Energy* **2018**, *44*, 327-335.

106. Anji Reddy, M.; Helen, M.; Groß, A.; Fichtner, M.; Euchner, H. Insight into

Sodium Insertion and the Storage Mechanism in Hard Carbon. *ACS Energy Letters* **2018**, *3*, 2851-2857.

107. Meng, Q.; Lu, Y.; Ding, F.; Zhang, Q.; Chen, L.; Hu, Y.-S. Tuning the Closed Pore Structure of Hard Carbons with the Highest Na Storage Capacity. *ACS Energy Letters* **2019**, *4*, 2608-2612.

108. Huang, S.; Li, Z.; Wang, B.; Zhang, J.; Peng, Z.; Qi, R.; Wang, J.; Zhao, Y. N-Doping and Defective Nanographitic Domain Coupled Hard Carbon Nanoshells for High Performance Lithium/Sodium Storage. *Advanced Functional Materials* **2018**, *28*, 1706294.

109. Yu, Z.; Liu, Q.; Chen, C.; Zhu, Y.; Zhang, B. Regulating the Interfacial Chemistry Enables Fast-Kinetics Hard Carbon Anodes for Potassium Ion Batteries. *Journal of Power Sources* **2023**, *557*, 232592.

110. Li, Q.; Zhang, Y.; Chen, Z.; Zhang, J.; Tao, Y.; Yang, Q.-H. Discrete Graphitic Crystallites Promise High-Rate Ion Intercalation for Kc8 Formation in Potassium Ion Batteries. *Advanced Energy Materials* **2022**, *12*, 2201574.

111. Chacón-Torres, J. C.; Wirtz, L.; Pichler, T. Manifestation of Charged and Strained Graphene Layers in the Raman Response of Graphite Intercalation Compounds. *ACS Nano* **2013**, *7*, 9249-9259.

112. Tan, H.; Zhou, R.; Zhang, B. Understanding Potassium Ion Storage Mechanism in

Pitch-Derived Soft Carbon and the Consequence on Cyclic Stability. *Journal of Power Sources* **2021**, *506*, 230179.

113. Share, K.; Cohn, A. P.; Carter, R. E.; Pint, C. L. Mechanism of Potassium Ion Intercalation Staging in Few Layered Graphene from in Situ Raman Spectroscopy.

Nanoscale 2016, 8, 16435-16439.

114. Komaba, S.; Murata, W.; Ishikawa, T.; Yabuuchi, N.; Ozeki, T.; Nakayama, T.; Ogata, A.; Gotoh, K.; Fujiwara, K. Electrochemical Na Insertion and Solid Electrolyte Interphase for Hard-Carbon Electrodes and Application to Na-Ion Batteries. *Advanced Functional Materials* **2011**, *21*, 3859-3867.

115. Hardwick, L. J.; Ruch, P. W.; Hahn, M.; Scheifele, W.; Kotz, R.; Novak, P. In Situ Raman Spectroscopy of Insertion Electrodes for Lithium-Ion Batteries and Supercapacitors: First Cycle Effects. *Journal of Physics and Chemistry of Solids* **2008**, *69*, 1232-1237.

116. Onuma, H.; Kubota, K.; Muratsubaki, S.; Ota, W.; Shishkin, M.; Sato, H.; Yamashita, K.; Yasuno, S.; Komaba, S. Phase Evolution of Electrochemically Potassium Intercalated Graphite. *Journal of Materials Chemistry A* **2021**, *9*, 11187-11200.

117. Xu, Z.; Wang, J.; Guo, Z.; Xie, F.; Liu, H.; Yadegari, H.; Tebyetekerwa, M.; Ryan, M. P.; Hu, Y. S.; Titirici, M. M. The Role of Hydrothermal Carbonization in Sustainable

Sodium-Ion Battery Anodes. Advanced Energy Materials 2022, 12, 2200208.

118. Wang, Z.; Feng, X.; Bai, Y.; Yang, H.; Dong, R.; Wang, X.; Xu, H.; Wang, Q.; Li, H.; Gao, H.; et al. Probing the Energy Storage Mechanism of Quasi-Metallic Na in Hard Carbon for Sodium-Ion Batteries. *Advanced Energy Materials* **2021**, *11*, 2003854.

119. Li, Q.; Liu, X.; Tao, Y.; Huang, J.; Zhang, J.; Yang, C.; Zhang, Y.; Zhang, S.; Jia, Y.; Lin, Q.; et al. Sieving Carbons Promise Practical Anodes with Extensible Low-Potential Plateaus for Sodium Batteries. *National Science Review* **2022**, *9*, nwac084.

120. Liu, J.; Yin, T.; Tian, B.; Zhang, B.; Qian, C.; Wang, Z.; Zhang, L.; Liang, P.; Chen, Z.; Yan, J.; et al. Unraveling the Potassium Storage Mechanism in Graphite Foam.

121. Feng, Z.; Lin, Y.; Tian, C.; Hu, H.; Su, D. Combined Study of the Ground and Excited States in the Transformation of Nanodiamonds into Carbon Onions by Electron Energy-Loss Spectroscopy. *Scientific Reports* **2019**, *9*, 3784.

Advanced Energy Materials 2019, 9, 1900579.

- 122. Nonaka, T.; Kawaura, H.; Makimura, Y.; Nishimura, Y. F.; Dohmae, K. In Situ X-Ray Raman Scattering Spectroscopy of a Graphite Electrode for Lithium-Ion Batteries. *Journal of Power Sources* **2019**, *419*, 203-207.
- 123. Hightower, A.; Ahn, C. C.; Fultz, B.; Rez, P. Electron Energy-Loss Spectrometry on Lithiated Graphite. *Applied Physics Letters* **2000**, *77*, 238-240.
- 124. Yun, Y. S.; Park, K.-Y.; Lee, B.; Cho, S. Y.; Park, Y.-U.; Hong, S. J.; Kim, B. H.;

- Gwon, H.; Kim, H.; Lee, S.; et al. Sodium-Ion Storage in Pyroprotein-Based Carbon Nanoplates. *Advanced Materials* **2015**, *27*, 6914-6921.
- 125. Feher, G.; Kip, A. F. Electron Spin Resonance Absorption in Metals. I. Experimental. *Physical Review* **1955**, *98*, 337-348.
- 126. Kawamura, K. Electron Spin Resonance Behavior of Pitch-Based Carbons in the Heat Treatment Temperature Range of 1100–2000 °C. *Carbon* **1998**, *36*, 1227-1230.
- 127. Wu, Y.-P.; Wan, C.-R.; Jiang, C.-Y.; Fang, S.-B.; Jiang, Y.-Y. Mechanism of Lithium Storage in Low Temperature Carbon. *Carbon* **1999**, *37*, 1901-1908.
- 128. Zhecheva, E.; Stoyanova, R.; Jiménez-Mateos, J. M.; Alcántara, R.; Lavela, P.; Tirado, J. L. EPR Study on Petroleum Cokes Annealed at Different Temperatures and Used in Lithium and Sodium Batteries. *Carbon* **2002**, *40*, 2301-2306.
- 129. Yu, Z.-E.; Lyu, Y.; Wang, Y.; Xu, S.; Cheng, H.; Mu, X.; Chu, J.; Chen, R.; Liu, Y.; Guo, B. Hard Carbon Micro-Nano Tubes Derived from Kapok Fiber as Anode Materials for Sodium-Ion Batteries and the Sodium-Ion Storage Mechanism. *Chemical Communications* **2020**, *56*, 778-781.
- 130. Niemöller, A.; Jakes, P.; Eichel, R.-A.; Granwehr, J. EPR Imaging of Metallic Lithium and Its Application to Dendrite Localisation in Battery Separators. *Scientific Reports* **2018**, *8*, 14331.
- 131. Lin, X.; Liu, Y.; Tan, H.; Zhang, B. Advanced Lignin-Derived Hard Carbon for

Na-Ion Batteries and a Comparison with Li and K Ion Storage. *Carbon* **2020**, *157*, 316-323.

132. Hatanaka, A.; Elakneswaran, Y.; Kurumisawa, K.; Nawa, T. The Impact of Tortuosity on Chloride Ion Diffusion in Slag-Blended Cementitious Materials. *Journal of Advanced Concrete Technology* **2017**, *15*, 426-439.

133. Tang, Z.; Wang, H.; Wu, P. F.; Zhou, S. Y.; Huang, Y. C.; Zhang, R.; Sun, D.; Tang, Y. G.; Wang, H. Y. Electrode-Electrolyte Interfacial Chemistry Modulation for Ultra-High Rate Sodium-Ion Batteries. *Angewandte Chemie International Edition* **2022**, *61*, e202200475.

134. Liang, H. J.; Gu, Z. Y.; Zhao, X. X.; Guo, J. Z.; Yang, J. L.; Li, W. H.; Li, B.; Liu, Z. M.; Li, W. L.; Wu, X. L. Ether-Based Electrolyte Chemistry Towards High-Voltage and Long-Life Na-Ion Full Batteries. *Angewandte Chemie International Edition* **2021**, *60*, 26837-26846.

135. Tian, Y. F.; Tan, S. J.; Lu, Z. Y.; Xu, D. X.; Chen, H. X.; Zhang, C. H.; Zhang, X. S.; Li, G.; Zhao, Y. M.; Chen, W. P.; et al. Insights into Anion-Solvent Interactions to Boost Stable Operation of Ether-Based Electrolytes in Pure-SiO_x||LiNi_{0.8}Mn_{0.1}Co_{0.1}O₂ Full Cells. *Angew Chem Int Ed Engl* **2023**, *62*, e202305988.

136. Li, Q.; Cao, Z.; Wahyudi, W.; Liu, G.; Park, G.-T.; Cavallo, L.; Anthopoulos, T.D.; Wang, L.; Sun, Y.-K.; Alshareef, H. N.; et al. Unraveling the New Role of an

Ethylene Carbonate Solvation Shell in Rechargeable Metal Ion Batteries. *ACS Energy Letters* **2021**, *6*, 69-78.

137. Holoubek, J.; Liu, H.; Wu, Z.; Yin, Y.; Xing, X.; Cai, G.; Yu, S.; Zhou, H.; Pascal, T. A.; Chen, Z.; et al. Tailoring Electrolyte Solvation for Li Metal Batteries Cycled at Ultra-Low Temperature. *Nature Energy* **2021**, *6*, 303-313.

138. Wang, C.; Appleby, A. J.; Little, F. E. Irreversible Capacities of Graphite Anode for Lithium-Ion Batteries. *Journal of Electroanalytical Chemistry* **2002**, *519*, 9-17.

139. Jian, Z. L.; Xing, Z. Y.; Bommier, C.; Li, Z. F.; Ji, X. L. Hard Carbon Microspheres: Potassium-Ion Anode Versus Sodium-Ion Anode. *Advanced Energy Materials* **2016**, *6*, 1501874.

140. Xiao, N.; Zhang, X.; Liu, C.; Wang, Y.; Li, H.; Qiu, J. Coal-Based Carbon Anodes for High-Performance Potassium-Ion Batteries. *Carbon* **2019**, *147*, 574-581.

141. Huang, W.; Attia, P. M.; Wang, H.; Renfrew, S. E.; Jin, N.; Das, S.; Zhang, Z.; Boyle, D. T.; Li, Y.; Bazant, M. Z.; et al. Evolution of the Solid–Electrolyte Interphase on Carbonaceous Anodes Visualized by Atomic-Resolution Cryogenic Electron Microscopy. *Nano Letters* **2019**, *19*, 5140-5148.

142. Gao, Y.; Hou, Z.; Zhou, R.; Wang, D.; Guo, X.; Zhu, Y.; Zhang, B. Critical Roles of Mechanical Properties of Solid Electrolyte Interphase for Potassium Metal Anodes. *Advanced Functional Materials* **2022**, *32*, 2112399.

- 143. Cao, C.; Abate, I. I.; Sivonxay, E.; Shyam, B.; Jia, C.; Moritz, B.; Devereaux, T. P.; Persson, K. A.; Steinrück, H.-G.; Toney, M. F. Solid Electrolyte Interphase on Native Oxide-Terminated Silicon Anodes for Li-Ion Batteries. *Joule* **2019**, *3*, 762-781.
- 144. Pham, T. D.; Lee, K.-K. Simultaneous Stabilization of the Solid/Cathode Electrolyte Interface in Lithium Metal Batteries by a New Weakly Solvating Electrolyte. *Small* **2021**, *17*, 2100133.
- 145. Peled, E.; Menkin, S. Review—SEI: Past, Present and Future. *Journal of The Electrochemical Society* **2017**, *164*, A1703-A1719.
- 146. He, M.; Guo, R.; Hobold, G. M.; Gao, H.; Gallant, B. M. The Intrinsic Behavior of Lithium Fluoride in Solid Electrolyte Interphases on Lithium. *Proceedings of the National Academy of Sciences* **2020**, *117*, 73-79.
- 147. Huang, J.; Guo, X.; Du, X.; Lin, X.; Huang, J.-Q.; Tan, H.; Zhu, Y.; Zhang, B. Nanostructures of Solid Electrolyte Interphases and Their Consequences for Microsized Sn Anodes in Sodium Ion Batteries. *Energy & Environmental Science* **2019**, *12*, 1550-1557.
- 148. Tian, F.; Radin, M. D.; Siegel, D. J. Enhanced Charge Transport in Amorphous Li₂O₂. *Chemistry of Materials* **2014**, *26*, 2952-2959.
- 149. Hundekar, P.; Basu, S.; Fan, X.; Li, L.; Yoshimura, A.; Gupta, T.; Sarbada, V.; Lakhnot, A.; Jain, R.; Narayanan, S.; et al. In Situ Healing of Dendrites in a Potassium

Metal Battery. *Proceedings of the National Academy of Sciences* **2020**, *117*, 5588-5594.

150. Verma, P.; Maire, P.; Novák, P. A Review of the Features and Analyses of the Solid Electrolyte Interphase in Li-Ion Batteries. *Electrochimica Acta* **2010**, *55*, 6332-6341.

151. Campbell, Q. T. Voltage-Dependent First-Principles Barriers to Li Transport within Li-Ion Battery Solid Electrolyte Interphases. *The Journal of Physical Chemistry C* **2024**, *128*, 10259-10269.

- 152. Allen J. Bard, L. R. F. *Electrochemical Methods Fundamentals and Applications*; 2001.
- 153. Trasatti, S. The Absolute Electrode Potential: An Explanatory Note (Recommendations 1986). *Pure and Applied Chemistry* **1986**, *58*, 955-966.
- 154. Lian, X.; Ju, Z.; Li, L.; Yi, Y.; Zhou, J.; Chen, Z.; Zhao, Y.; Tian, Z.; Su, Y.; Xue, Z.; et al. Dendrite-Free and High-Rate Potassium Metal Batteries Sustained by an Inorganic-Rich SEI. *Advanced Materials* **2024**, *36*, 2306992.
- 155. Zhong, Y.; Zhou, S.; He, Q.; Pan, A. Architecture Design Principles for Stable Electrodeposition Behavior-Towards Better Alkali Metal (Li/Na/K) Anodes. *Energy Storage Materials* **2022**, *45*, 48-73.
- 156. Li, Y.; Zhang, L.; Liu, S.; Wang, X.; Xie, D.; Xia, X.; Gu, C.; Tu, J. Original Growth Mechanism for Ultra-Stable Dendrite-Free Potassium Metal Electrode. *Nano Energy* **2019**, *62*, 367-375.

- 157. Zhang, L.; Liu, C.; Song, R.; Wang, Q.; Chen, Y.; Huang, P. Low-Temperature Graphitization of Carbon Foam Using Nickel-Based Catalysts for Enhanced Thermal Conductivity: Application in the Pyrolysis of Oil-Rich Coal. *Journal of Porous Materials* **2024**, *31*, 1087-1099.
- 158. Liu, P.; Wang, Y.; Hao, H.; Basu, S.; Feng, X.; Xu, Y.; Boscoboinik, J. A.; Nanda, J.; Watt, J.; Mitlin, D. Stable Potassium Metal Anodes with an All-Aluminum Current Collector through Improved Electrolyte Wetting. *Advanced Materials* **2020**, *32*, 2002908.
- 159. Lin, Y.-X.; Liu, Z.; Leung, K.; Chen, L.-Q.; Lu, P.; Qi, Y. Connecting the Irreversible Capacity Loss in Li-Ion Batteries with the Electronic Insulating Properties of Solid Electrolyte Interphase (SEI) Components. *Journal of Power Sources* **2016**, *309*, 221-230.
- 160. Ramprasad, R.; Allmen, P. V.; Fonseca, L. R. C. Contributions to the Work Function: A Density-Functional Study of Adsorbates at Graphene Ribbon Edges. *Physical Review B* **1999**, *60*, 6023-6028.
- 161. Leung, T. C.; Kao, C. L.; Su, W. S.; Feng, Y. J.; Chan, C. T. Relationship between Surface Dipole, Work Function and Charge Transfer: Some Exceptions to an Established Rule. *Physical Review B* **2003**, *68*, 195408.
- 162. Kahn, A. Fermi Level, Work Function and Vacuum Level. Materials Horizons

2016, *3*, 7-10.

163. Ren, X.; Gao, P.; Zou, L.; Jiao, S.; Cao, X.; Zhang, X.; Jia, H.; Engelhard, M. H.; Matthews, B. E.; Wu, H.; et al. Role of Inner Solvation Sheath within Salt–Solvent Complexes in Tailoring Electrode/Electrolyte Interphases for Lithium Metal Batteries.

Proceedings of the National Academy of Sciences 2020, 117, 28603-28613.

164. J. shama, T. G., J.D. Rimstidt and Ralph Staley. X-Ray Photoelectron Spectra of Alkali Azides. *Chemical Physics Letters* **1972**, *15*, 232-235.

165. Li, X.; Li, Q.; Yan, W.; Fan, B.; Wang, Z. In-Situ Controllable Electrodeposition of NiS_x Nanostructures Coupled with Polypyrrole for Enhanced Hydrogen Evolution Reaction. *International Journal of Hydrogen Energy* **2024**, *51*, 443-451.

166. Zhao, Q.; Stalin, S.; Archer, L. A. Stabilizing Metal Battery Anodes through the Design of Solid Electrolyte Interphases. *Joule* **2021**, *5*, 1119-1142.

167. Scharifker, B.; Hills, G. Theoretical and Experimental Studies of Multiple Nucleation. *Electrochimica Acta* **1983**, *28*, 879-889.

168. Thirumalraj, B.; Hagos, T. T.; Huang, C.-J.; Teshager, M. A.; Cheng, J.-H.; Su, W.-N.; Hwang, B.-J. Nucleation and Growth Mechanism of Lithium Metal Electroplating. *Journal of the American Chemical Society* **2019**, *141*, 18612-18623.

169. Grujicic, D.; Pesic, B. Electrodeposition of Copper: The Nucleation Mechanisms. *Electrochimica Acta* **2002**, *47*, 2901-2912. 170. Pande, V.; Viswanathan, V. Computational Screening of Current Collectors for Enabling Anode-Free Lithium Metal Batteries. *ACS Energy Letters* **2019**, *4*, 2952-2959.

171. Aurbach, D.; Pollak, E.; Elazari, R.; Salitra, G.; Kelley, C. S.; Affinito, J. On the Surface Chemical Aspects of Very High Energy Density, Rechargeable Li–Sulfur Batteries. *Journal of The Electrochemical Society* **2009**, *156*, A694.

172. Yang, Y.; Davies, D. M.; Yin, Y.; Borodin, O.; Lee, J. Z.; Fang, C.; Olguin, M.; Zhang, Y.; Sablina, E. S.; Wang, X.; et al. High-Efficiency Lithium-Metal Anode Enabled by Liquefied Gas Electrolytes. *Joule* **2019**, *3*, 1986-2000.

173. Collet, J.; Tharaud, O.; Chapoton, A.; Vuillaume, D. Low-Voltage, 30 nm Channel Length, Organic Transistors with a Self-Assembled Monolayer as Gate Insulating Films.

Applied Physics Letters 2000, 76, 1941-1943.

174. Hona, R. K.; Azure, A. D.; Guinn, M.; Phuyal, U. S.; Stroh, K.; Thapa, A. K. Ionic Conductivity of K-Ion Glassy Solid Electrolytes of K2S-P2S5-Kotf System.

International Journal of Molecular Sciences 2023, 24, 16855.

175. Li, Z.; Huai, L.; Li, S.; Ma, M.; Luo, K.; Zhao, Y.; Wang, D.; Sun, X.; Peng, Z. Insight into Bulk Charge Transfer of Lithium Metal Anodes by Synergism of Nickel Seeding and Lif-Li3n-Li2s Co-Doped Interphase. *Energy Storage Materials* **2021**, *37*, 491-500.

176. Adams, B. D.; Zheng, J.; Ren, X.; Xu, W.; Zhang, J.-G. Accurate Determination

of Coulombic Efficiency for Lithium Metal Anodes and Lithium Metal Batteries.

Advanced Energy Materials 2018, 8, 1702097.

177. Han, M.; Jiang, J.; Lu, S.; Jiang, Y.; Ma, W.; Liu, X.; Zhao, B.; Zhang, J. Moderate Specific Surface Areas Help Three-Dimensional Frameworks Achieve Dendrite-Free Potassium-Metal Anodes. *ACS Applied Materials & Interfaces* **2022**, *14*, 900-909.

178. Zhao, Y.; Liu, B.; Yi, Y.; Lian, X.; Wang, M.; Li, S.; Yang, X.; Sun, J. An Anode-Free Potassium-Metal Battery Enabled by a Directly Grown Graphene-Modulated Aluminum Current Collector. *Advanced Materials* **2022**, *34*, 2202902.

179. Yi, Y.; Li, J.; Gao, Z.; Liu, W.; Zhao, Y.; Wang, M.; Zhao, W.; Han, Y.; Sun, J.; Zhang, J. Highly Potassiophilic Graphdiyne Skeletons Decorated with Cu Quantum Dots Enable Dendrite-Free Potassium-Metal Anodes. *Advanced Materials* **2022**, *34*, 2202685.

180. Liu, P.; Wang, Y.; Gu, Q.; Nanda, J.; Watt, J.; Mitlin, D. Dendrite-Free Potassium Metal Anodes in a Carbonate Electrolyte. *Advanced Materials* **2020**, *32*, 1906735.

181. Tang, X.; Zhou, D.; Li, P.; Guo, X.; Sun, B.; Liu, H.; Yan, K.; Gogotsi, Y.; Wang,G. Mxene-Based Dendrite-Free Potassium Metal Batteries. *Advanced Materials* 2020,32, 1906739.

182. Wang, J.; Yuan, J.; Chen, C.; Wang, L.; Zhai, Z.; Fu, Q.; Liu, Y.; Dong, L.; Yan, W.; Li, A.; et al. Cu₃Pt Alloy-Functionalized Cu Mesh as Current Collector for

Dendritic-Free Anodes of Potassium Metal Batteries. *Nano Energy* **2020**, *75*, 104914.

183. Zhou, M.; Qi, W.; Hu, Z.; Cheng, M.; Zhao, X.; Xiong, P.; Su, H.; Li, M.; Hu, J.; Xu, Y. Highly Potassiophilic Carbon Nanofiber Paper Derived from Bacterial Cellulose Enables Ultra-Stable Dendrite-Free Potassium Metal Anodes. *ACS Applied Materials* & *Interfaces* **2021**, *13*, 17629-17638.

184. Zhao, X.; Chen, F.; Liu, J.; Cheng, M.; Su, H.; Liu, J.; Xu, Y. Enhanced Surface Binding Energy Regulates Uniform Potassium Deposition for Stable Potassium Metal Anodes. *Journal of Materials Chemistry A* **2020**, *8*, 5671-5678.

185. Hatzell, K. B. Anode-Less or Anode-Free? ACS Energy Letters 2023, 8, 4775-4776.

186. Wang, C.; Xing, L.; Vatamanu, J.; Chen, Z.; Lan, G.; Li, W.; Xu, K. Overlooked Electrolyte Destabilization by Manganese (II) in Lithium-Ion Batteries. *Nature Communications* **2019**, *10*, 3423.

187. Bie, X.; Kubota, K.; Hosaka, T.; Chihara, K.; Komaba, S. A Novel K-Ion Battery: Hexacyanoferrate(ii)/Graphite Cell. *Journal of Materials Chemistry A* **2017**, *5*, 4325-4330.

188. Gao, C.; Lei, Y.; Wei, Y.; Wang, H.; Yuan, F.; Kang, F.; Zhai, D. Coexistence of Two Coordinated States Contributing to High-Voltage and Long-Life Prussian Blue Cathode for Potassium Ion Battery. *Chemical Engineering Journal* **2022**, *431*, 133926.

189. Jiang, X.; Zhang, T.; Yang, L.; Li, G.; Lee, J. Y. A Fe/Mn-Based Prussian Blue Analogue as a K-Rich Cathode Material for Potassium-Ion Batteries.

ChemElectroChem 2017, 4, 2237-2242.

190. Xu, C.; Yang, Z.; Zhang, X.; Xia, M.; Yan, H.; Li, J.; Yu, H.; Zhang, L.; Shu, J. Prussian Blue Analogues in Aqueous Batteries and Desalination Batteries. *Nano-Micro Letters* **2021**, *13*, 166.

191. Yamada, Y.; Chiang, C. H.; Sodeyama, K.; Wang, J.; Tateyama, Y.; Yamada, A. Corrosion Prevention Mechanism of Aluminum Metal in Superconcentrated Electrolytes. *ChemElectroChem* **2015**, *2*, 1687-1694.

192. Xue, W.; Huang, M.; Li, Y.; Zhu, Y. G.; Gao, R.; Xiao, X.; Zhang, W.; Li, S.; Xu, G.; Yu, Y.; et al. Ultra-High-Voltage Ni-Rich Layered Cathodes in Practical Li Metal Batteries Enabled by a Sulfonamide-Based Electrolyte. *Nature Energy* **2021**, *6*, 495-505.

193. Ge, J.; Fan, L.; Rao, A. M.; Zhou, J.; Lu, B. Surface-Substituted Prussian Blue Analogue Cathode for Sustainable Potassium-Ion Batteries. *Nature Sustainability* **2022**, *5*, 225-234.

194. Lei, K.; Zhu, Z.; Yin, Z.; Yan, P.; Li, F.; Chen, J. Dual Interphase Layers in Situ Formed on a Manganese-Based Oxide Cathode Enable Stable Potassium Storage. *Chem* **2019**, *5*, 3220-3231.

195. Kim, S. C.; Oyakhire, S. T.; Athanitis, C.; Wang, J.; Zhang, Z.; Zhang, W.; Boyle, D. T.; Kim, M. S.; Yu, Z.; Gao, X.; et al. Data-Driven Electrolyte Design for Lithium Metal Anodes. *Proceedings of the National Academy of Sciences* **2023**, *120*, e2214357120.

196. Wang, Z.; Chen, C.; Wang, D.; Zhu, Y.; Zhang, B. Stabilizing Interfaces in High-Temperature Ncm811-Li Batteries Via Tuning Terminal Alkyl Chains of Ether Solvents.

*Angewandte Chemie 2023, 135, e202303950.

197. Lin, J.; Peng, H.; Huang, P.; Naren, T.; Liang, C.; Kuang, G.; Chen, L.; Zhang, C.; Wei, W. Electrically Coupled Electrolyte Engineering Enables High Interfacial Stability for High-Voltage Sodium-Ion Batteries. *Advanced Functional Materials* **2023**, *33*, 2307061.

198. Wahyudi, W.; Ladelta, V.; Tsetseris, L.; Alsabban, M. M.; Guo, X.; Yengel, E.; Faber, H.; Adilbekova, B.; Seitkhan, A.; Emwas, A.-H.; et al. Lithium-Ion Desolvation Induced by Nitrate Additives Reveals New Insights into High Performance Lithium Batteries. *Advanced Functional Materials* **2021**, *31*, 2101593.

199. Wang, Q.; Sun, J.; Yao, X.; Chen, C. Thermal Stability of LiPF₆/EC+DEC Electrolyte with Charged Electrodes for Lithium Ion Batteries. *Thermochimica Acta* **2005**, *437*, 12-16.

200. Hosaka, T.; Matsuyama, T.; Tatara, R.; Gossage, Z. T.; Komaba, S. Impact of

Electrolyte Decomposition Products on the Electrochemical Performance of 4 V Class K-Ion Batteries. *Chemical Science* **2023**, *14*, 8860-8868.

201. Bar-Tow, D.; Peled, E.; Burstein, L. A Study of Highly Oriented Pyrolytic Graphite as a Model for the Graphite Anode in Li-Ion Batteries. *Journal of The Electrochemical Society* **1999**, *146*, 824.

202. Tong, B.; Song, Z.; Wan, H.; Feng, W.; Armand, M.; Liu, J.; Zhang, H.; Zhou, Z. Sulfur-Containing Compounds as Electrolyte Additives for Lithium-Ion Batteries. *InfoMat* **2021**, *3*, 1364-1392.

203. Mo, Y.; Zhou, W.; Wang, K.; Xiao, K.; Chen, Y.; Wang, Z.; Tang, P.; Xiao, P.; Gong, Y.; Chen, S.; et al. Engineering Electrode/Electrolyte Interphase Chemistry toward High-Rate and Long-Life Potassium Ion Full-Cell. *ACS Energy Letters* **2023**, *8*, 995-1002.

204. Hall, D. S.; Allen, J. P.; Glazier, S. L.; Ellis, L. D.; Ma, L.; Peters, J. M.; Hill, I. G.; Dahn, J. R. The Solid-Electrolyte Interphase Formation Reactions of Ethylene Sulfate and Its Synergistic Chemistry with Prop-1-Ene-1,3-Sultone in Lithium-Ion Cells. *Journal of The Electrochemical Society* **2017**, *164*, A3445.

205. Xia, J.; Sinha, N. N.; Chen, L. P.; Dahn, J. R. A Comparative Study of a Family of Sulfate Electrolyte Additives. *Journal of The Electrochemical Society* **2014**, *161*, A264. 206. Wu, Z.; Li, S.; Zheng, Y.; Zhang, Z.; Umesh, E.; Zheng, B.; Zheng, X.; Yang, Y.

The Roles of Sulfur-Containing Additives and Their Working Mechanism on the Temperature-Dependent Performances of Li-Ion Batteries. *Journal of The Electrochemical Society* **2018**, *165*, A2792.

207. Tian, M.; Ben, L.; Yu, H.; Song, Z.; Yan, Y.; Zhao, W.; Armand, M.; Zhang, H.; Zhou, Z.-B.; Huang, X. Designer Cathode Additive for Stable Interphases on High-Energy Anodes. *Journal of the American Chemical Society* **2022**, *144*, 15100-15110.